Vibration damping in beams using the acoustic black hole effect

Vivien Denis

To cite this version:

Vivien Denis. Vibration damping in beams using the acoustic black hole effect. Vibrations [physics.class-ph]. Université du Maine, 2014. English. NNT : . tel-01075826

HAL Id: tel-01075826

https://hal.science/tel-01075826

Submitted on 20 Oct 2014

Académie de Nantes

Université Du Maine, Le Mans, France
École Doctorale Sciences Pour l'Ingénieur, Géosciences, Architecture

Thèse de Doctorat
Spécialité : Acoustique

AMORTISSEMENT VIBRATOIRE DE POUTRES PAR EFFET TROU NOIR ACOUSTIQUE

Vivien DENIS

Préparée au Laboratoire d'Acoustique de l'Université du Maine, UMR CNRS 6613

Soutenue sous réserve de l'avis positif des rapporteurs
le 22 octobre 2014 devant le jury composé de :

S.C. CONLON	Professeur, Penn State University (State College)	Invité
S. FÉLIX	Chargé de recherche CNRS, LAUM (Le Mans)	Examinateur
F. GAUTIER	Professeur, LAUM (Le Mans)	Directeur de thèse
M. ICHCHOU	Professeur, Ecole Centrale de Lyon (Lyon)	Rapporteur
V. KRYLOV	Professeur, Loughborough University (Loughborough)	Rapporteur
M. MIRONOV	Professeur, Andreev Acoustic Institute (Moscou)	Examinateur
A. PELAT	Maître de conférences, LAUM (Le Mans)	Co-directeur de thèse
C. TOUZÉ	Professeur, ENSTA Paritech (Paris)	Examinateur

RÉSUMÉ

L'amortissement des vibrations mécaniques de structure joue un rôle important dans de nombreuses applications industrielles. Les méthodes classiques de réduction de vibration par ajout de revêtement viscoélastique donnent généralement lieu à une augmentation de masse importante, ce qui peut être rédhibitoire dans l'industrie des transports pour des raisons écologiques ou économiques. L'effet "Trou Noir Acoustique" (TN) est une méthode passive permettant d'obtenir un amortissement de la structure sans augmenter sa masse: les ondes de flexion se propageant dans une extrémité de plaque profilée avec une loi de puissance sont efficacement dissipées si l'on place un film amortissant dans la zone terminale.

Une étude préliminaire de nature expérimentale confirme le potentiel du TN comme stratégie d'amortissement: une analyse modale montre que le TN augmente significativement le facteur de recouvrement modal (MOF) de la poutre, et réduit donc son caractère résonant. Une analyse basée sur une approche ondulatoire montre clairement que le coefficient de réflexion de l'extrémité TN présente de faibles valeurs. Un modèle numérique bi-dimensionnel d'une poutre, développé pour analyser le comportement de la terminaison, montre que l'augmentation du MOF peut-être expliquée d'une part par une augmentation de la densité modale et d'autre part, par un fort amortissement des modes de la structure, causé par une localisation de l'énergie dans la région profilée. On établit que la poutre TN possède des modes locaux bi-dimensionnels, et un modèle de guide de la terminaison TN incluant des imperfections, qui ne peuvent être évitées en pratique, montre que l'énergie incidente est diffusée sur de nombreux modes locaux. Les imperfections du TN améliorent ainsi ses performances.

L'analyse des mécanismes dissipatifs mis en jeu dans le TN permet d'estimer les performances en terme d'amortissement vibratoire, de tirer le meilleur parti de ces mécanismes, d'en déduire des règles de dimensionnement et donc d'envisager son intégration dans des applications utiles à l'ingénieur.

Académie de Nantes

Université Du Maine, Le Mans, France
Doctoral school of Science Engineering, Geoscience and Architecture

Doctoral thesis in Acoustics

Vibration damping in beams using the Acoustic Black Hole effect

Vivien DENIS

Prepared in the Acoustic Laboratory of le Mans, UMR CNRS 6613

Defended subject to acceptance of the reviewers
the 22th of October 2014 in front of the examining committee:

S.C. Conlon	Professor, Penn State University (State College)	Invited member
S. Félix	CNRS researcher, LAUM (Le Mans)	Examiner
F. Gautier	Professor, LAUM (Le Mans)	Supervisor
M. Ichchou	Professor, Ecole Centrale de Lyon (Lyon)	Reviewer
V. Krylov	Professor, Loughborouh University (Loughborough)	Reviewer
M. Mironov	Professor, Andreev Acoustic Institute (Moscow)	Examiner
A. Pelat	Lecturer, LAUM (Le Mans)	Co-supervisor
C. Touzé	Professor, ENSTA Paritech (Paris)	Examiner

ABSTRACT

Vibration damping of mechanical structures is playing an important role in the design of many industrial systems. Classical methods for reducing vibrations using viscoelastic layers glued to the structure usually result in added mass on the treated structure, which may be prohibitive in transportation industry for ecological and economical reasons. The "Acoustic Black Hole" (ABH) effect is a lightweight passive vibration technique: the flexural waves propagating in a beam extremity tapered with a power law profile are efficiently dissipated if an absorbing layer is placed where the thickness is minimum.

A preliminary study experimentally confirms the potential of ABH as an efficient strategy for vibration damping: a modal analysis shows that the ABH significantly increases the Modal Overlap Factor (MOF) of the beam, thus reducing the resonant behaviour of the structure. An analysis based on a wave approach clearly shows that the reflection coefficient of an ABH termination has small values. Further investigations, including a two dimensional numerical model of the structure developed in order to understand its behaviour, show that the increase of MOF can be explained partly by an increase of the modal density and mostly by a high damping of a number of modes of the structure due to energy localisation in the tapered region. It is shown that the ABH beam possesses two-dimensional local modes. A waveguide model of an ABH termination with tip imperfection, which cannot be avoided in practice, shows that incident energy is scattered on local modes and that imperfections enhance the damping effect.

The analysis of the dissipative mechanisms involved pin the ABH effect permits to estimate its performances in vibration damping, helps make the most of these mechanisms, allows to deduce dimensioning rules and thus to consider its integration into useful engineering applications.

ACKNOWLEDGEMENTS

Je suis tout d'abord reconnaissant à François et Adrien pour m'avoir accordé leur confiance et guidé pendant ces trois ans.

Je suis également reconnaissant à Stanislas Renard pour l'usinage des poutres aluminium utilisées et à Cécile Leroux du Centre de Transfert de Technologie du Mans (CTTM) pour la réalisation des poutres polymères.

Je remercie le ministère de la recherche pour m'avoir accordé le financement qui m'a permis de réaliser cette thèse de doctorat.

J'ai apprécié l'accueil du Laboratoire d'Acoustique de l'Université du Maine (LAUM), et de ses directeurs Joël et Laurent. Merci aux chercheurs de ce laboratoire pour l'accueil sympathique, l'ambiance générale ou les discussions scientifiques. Je pense particulièrement à Charles, Jean-Michel, Aroune, Jean-Philippe. Le travail d'Anne-Marie a par ailleurs été précieux lors des déplacements.

Merci à l'Ecole Nationale Supérieure d'Ingénieurs du Mans (ENSIM) qui a été ma seconde maison durant trois ans, et à son directeur Pascal. Merci à la cafetière quotidienne et ceux qui chaque jour, font le café, plus ou moins acide, plus ou moins serré. Je tiens à remercier l'équipe technique pour l'aide et les sourires au quotidien: Mathieu, Julien, Nicolas, Cathy, Marilyne et Amina (que je croise tous les matins en vélo).

J'ai effectué mon service d'enseignement à l'ENSIM et travaillé dans ce contexte avec des gens agréables et compétents: je remercie Adrien, Samuel, Yannick et Marine.

Durant les première et deuxième années de thèse ont eu lieu des stages de master 2 en lien avec ma thèse; cela a été l'occasion de travailler avec Julien, Amar, Charlie et Charly. J'ai également reçu l'aide de Benjamin durant la première année.

Merci aux musiciens de l'Ensim'Phonic Orchestra de me supporter en tant que chef, à la fanfare Takasouffler et à l'Orchestre Départemental d'Harmonie d'occuper mes samedis après-midi et mes dimanches matin, respectivement.

Je n'ai jamais été seul en tant que thésard : de nombreuses personnes ont été embarquées dans cette aventure. Je leur suis reconnaissant d'être là pour l'ambiance ou la science. Je pense aux anciens qui donnent l'exemple : Clément, Damien, Mathieu, Miguel et Adil. Je pense aussi aux fanfarons Alberto et Jean-Baptiste, saxophoniste et saxophoniste, respectivement. Merci également à la bande des thésards de l'ENSIM :

Julien, Amar, Charly, Thibault, Charlie, Martial, Matthieu, Alexei et Alexandre. Merci aux occupants éphémères du bureau P12: Thibault et Thomas. Merci à Balbine pour son enthousiasme, à Margaux pour son humour, et à Hélène pour ses gâteaux.

Je remercie particulièrement Frédéric pour ses dessins, ses bons mots et ses conseils avisés.

Une pensée spéciale pour Laurianne qui travaille en face de moi depuis le début de l'aventure et m'a aidé à choisir la chemise que je porterai lors de ma soutenance.

Merci à ma famille, ma mère Corinne, mes frères Joaquim et Nicolas, ma soeur Clémentine, mes grands parents François, Liliane, Serge et Ginette d'être là tout simplement.

A mon père.

CONTENTS

LIST OF SYMBOLS

The following list summarises the main mathematical symbols used throughout this document, with their respective unit and a short description. Where no unit is given, the symbol is either unitless or corresponds to a matrix whose rows or columns have different units.

Time, frequency, space and wavenumber variables

t	s	Time
f	s^{-1}	Frequency
ω	$\text{rad}\cdot\text{s}^{-1}$	Circular frequency
x, y	m	Spatial coordinates in a global coordinate system
z	m	Space variable normal to the plate surface

Physical parameters of plates and beams

h	m	Plate thickness
ρ	kg.m^3	Mass density
η		Structural damping ratio
E_0	Pa	Young's modulus
E	Pa	Complex Young's modulus
G	Pa	Shear modulus
ν		Poisson's ratio
D	Pa.m^3	Bending stiffness / Flexural rigidity
k_f	m^{-1}	Flexural wavenumber
c_ϕ	m.s^{-1}	Phase velocity of flexural waves
c_γ	m.s^{-1}	Group velocity of flexural waves

Parameters of Acoustic Black Hole profile

m		Exponent of the profile
h_t	m	Truncation thickness
h_0	m	Thickness of the uniform region
l_{ABH}	m	Physical length of the tapered profile
l_t	m	Length of the tapered profile reaching zero thickness
ϵ		Parameter of the power-law profile
l_l	m	Length of the damping layer
a	m	Length of the infinitesimal rigid bar figuring an imperfection
m_0	kg	Mass of the imperfection in the simplified representation

Vibrational field variables

w	m	Plate transverse displacement
θ_x		Plate slope along x axis.
M_x	N	Bending moment acting on a cross-section of normal x
V_x	$\mathrm{N.m^{-1}}$	Total shear force on a cross-section of normal x
Y	$\mathrm{m.s^{-1}.N^{-1}}$	Mechanical admittance

Modal properties of flexural vibrations

d	s	Modal density
ξ_k		Modal damping ratio
η_k		Modal loss factor
$\Delta\omega_k$	$\mathrm{s^{-1}}$	-3dB-bandwith of resonance k
$\delta\omega_k$	$\mathrm{s^{-1}}$	Circular frequency interval between resonances k and $k+1$
Q		Quality factor of a resonance
MOF		Modal Overlap Factor
α_k	$\mathrm{rad.s^{-1}}$	Complex eigenvalue

Finite difference method

$\tilde{x}$		Transformed x coordinate
n, q		Spatial indices
$\delta_{\tilde{x}+}, \delta_{\tilde{x}-}$		Forward and backward finite difference operators along the $\tilde{x}$-coordinate
δ_{yy}		Finite difference operator approximating the second-order derivative along the y-coordinate
$\mu_{\tilde{x}+}, \mu_{\tilde{x}-}$		Forward and backward averaging operators along the $\tilde{x}$-coordinate
$\Delta_{\tilde{x}}$	m	Spatial step along the $\tilde{x}$-coordinate
Δ_y	m	Spatial step along the y-coordinate

State vector representation

$\mathbf{W}$		State vector
$\mathbf{H}$		Matricant
$\mathbf{\Lambda}$	m^{-1}	Eigenvalue matrix
$\mathbf{E}$		Eigenvector matrix
$\mathbf{V}$		Wave vector
$\mathbf{V}_+$		Forward-travelling wave vector
$\mathbf{V}_-$		Backward-travelling wave vector
$\mathbf{R}$		Reflection matrix
$\mathbf{R}^-$		Reflection matrix from side - to side -
$\mathbf{R}^+$		Reflection matrix from side + to side +
$\mathbf{T}^{-+}$		Reflection matrix from side - to side +
$\mathbf{T}^{+-}$		Reflection matrix from side + to side -
$\mathbf{R}_{ir}$		Sub reflection matrix representing the couplings between incident i and reflected r propagating p and attenuating a waves, e.g. R_{pp}, R_{pa}, R_{ap},R_{aa}
$\mathbf{T}_{it}$		Sub transmission matrix representing the couplings between incident i and transmitted t waves
$\mathbf{S}$		Scattering matrix of a section
$\mathbf{Z}$		Impedance matrix
$\mathbb{I}$		Identity matrix
$\mathbb{O}$		Zero matrix

Magnus method

$\bar{x}_n$	m	Discrete longitudinal coordinate
Ω_n		Magnus matrix
Δ	m	Spatial step

Operators and miscellaneous symbols

∇	m^{-1}	Del vector differential operator
ε		Error estimation
Re()		Real part
Im()		Imaginary part
Δl	m	Correction length
Arg()		Argument

Chapter 1

INTRODUCTION

1.1 Generalities on passive vibration damping methods

1.1.1 Classical damping techniques for vibration control

The control of unwanted vibrations is important for reliability, stability and comfort in many industrial applications [115]. Indeed, vibrations can generate radiated noise [28] but are also a source of structural damage [70]: stresses coming from vibration amplitude and high number of load cycles induce fatigue effect and reduce the lifetime of the system.

Furthermore, structure lightening is an important concern in many engineering domains. In the transport industry, increasing the mass of the vehicle impacts the fuel consumption because it generates a supplementary energy need: at a constant speed to counteract rolling resistance, and in acceleration phases. Therefore, the increase in mass impacts the CO_2 emissions in a negative way: for a standard public transportation vehicle (maximum 18 t in most European countries) a weight gain of 500 kg can generate 1 or 2 % gain in CO_2 emissions [1]. It is also a concern for aeronautic and aerospace vehicles where the power-to-weight ratio (or thrust-to-weight ratio) is important for fuel consumption and manoeuvrability concerns [50]. Structure lightening usually increases problems due to vibrations: structures can then have a larger vibration amplitude, radiate more efficiently and be more fragile. The development of vibration control methods adapted to light structures becomes of a great interest.

There are two classes of vibration control: active and passive. This study focuses only on passive techniques. The passive control of vibratory levels usually consists in either moving the natural frequencies of vibration of the structure out of the range of operating frequencies or if it is not achievable, to reduce the amplitude of the resonances without modifying their frequencies, by damping the motion.

A first cause of damping in a structure originates in the constitutive material, as part of the energy absorbed by a material under a cyclic load is dissipated as heat to the surroundings [40]. When a purely elastic material is submitted to oscillatory stress σ (during a Dynamic Mechanical Analysis [91] for example), the measured strain ϵ occurs in phase. In a viscoelastic material however, strain lags behind stress so that

$$\sigma = \sigma_0 e^{\mathrm{j}\omega t} \quad \text{and} \quad \epsilon = \epsilon_0 e^{\mathrm{j}(\omega t - \delta)}. \tag{1.1}$$

This phase lag is due to motion in the material at microscopic scale [40]. An usual way to characterize the material is then to define a complex Young's modulus E as

$$E = \frac{\sigma}{\epsilon} = \frac{\sigma_0}{\epsilon_0} \cos\delta (1 + \mathrm{j} \tan\delta) = E_0(1 + \mathrm{j}\eta), \tag{1.2}$$

where

$$E_0 = \frac{\sigma_0}{\epsilon_0} \cos\delta, \tag{1.3}$$

is the storage modulus and

$$\eta = \tan\delta, \tag{1.4}$$

is called the loss factor of the material, that models the dissipation of energy. Independently from the damping properties of material, energy in a vibrating structure can also be dissipated at boundary conditions, in structural joints through friction, that constitute localised sources of damping, or through acoustic radiation [11]. From a structural point of view, damping a structure corresponds to increasing the modal loss factors of the resonance peaks. With the exception of very academic structures, the relation between modal loss factors, intrinsic loss factor of the constitutive material and localised sources of damping in the structure is usually complex [59].

Classical vibration damping methods are thoroughly described in the literature [100, 68]. Several strategies are mentioned here:

- A damped structure can be realised by choosing materials having a high loss factor. Most of metal alloys are not suitable from this perspective. Viscoelastic materials such as polymers are however more interesting. Their properties vary a lot with temperature and frequency, according to the Williams-Landel-Ferry (WLF) model [48, 47]: at high temperature or low frequency, viscoelastic materials are soft and elastic. As the temperature decreases or the frequency increases, they become harder and dissipate more energy. At low temperature or high frequency, they become hard and non dissipative. The region of maximum damping, known as the glass-rubber transition, is fairly dependent on the material. Note that metal alloys with interesting damping characteristics have been developed, for example the Sonoston Cu-Mn alloy [70].

- Damping can also be obtained using tuned damping device (or tuned mass damper), which often consists in an added mass-spring system with viscous damping, or a mass on viscoelastic spring, or a viscoelastically damped resonant beam [69, 67, 122, 123] (see Fig. 1.1). Note that it differs from a dynamic absorber in that the true dynamic absorber does not require damping but requires precise tuning knowledge of the excitation frequency [33]. Since the tuned damping device actually dissipates energy, it is effective on several structural modes [114]. Ref. [100] shows the case of a beam covered with a distribution of tuned dampers (with η=0.5), where the effective modal loss factor obtained reaches 30 % at the price of a doubling in mass, but other works show that it is not economic to use a mass ratio higher than 15% for the dampers [23]. Albeit based on a simple and old principle, tuned mass dampers are the object of many recent works and are frequently applied in various engineering domains: automotive, rails, building, aircraft [110, 132].

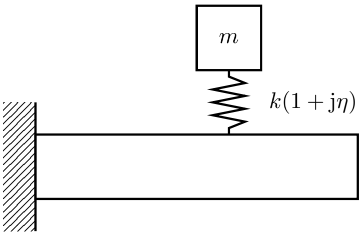

Figure 1.1: Simple configuration of tuned mass damper placed on a cantilever beam, as described in [122]. The device is defined by its mass m, stiffness k and loss factor η.

- Another classical way of damping vibrations consists in covering the structure to be treated with a surface damping layer (see Fig. 1.2(a)). The resulting damping properties of the treated structure come mainly from the extensional strains of the added layer. This mechanism is first described by Oberst [102] and is often used as a technique to estimate characteristics of soft materials. The Oberst model gives an expression of the modal parameters of the first flexural mode of a simply supported beam covered by a damping layer, thus allows to find equivalent material and geometrical characteristics of the beam. As long as extensional strains of the damping layer are concerned, the complex Young's modulus E of the damping layer is the parameter of interest. The complex stiffness of the covered beam writes [102]:

  $$EI = EI_1 \times \left(1 + e_2 h_2^3(1+\mathrm{j}\eta_2) + 3(1+h_2)^2 e_2 h_2 \frac{(1+\mathrm{j}\eta_2)}{(1+e_2 h_2(1+\mathrm{j}\eta_2))}\right), \qquad (1.5)$$

  where $e_2 = \frac{E_1}{E_2}$ and $h_2 = \frac{H_1}{H_2}$ with E_i, I_i, H_i, η_i the Young's modulus, inertia of the cross-section, thickness and loss factor of the i-th layer, respectively, with i=1, 2 (see Fig. 1.2(a)).

- An improvement of the efficiency of a damping layer is obtained if the damping layer is no more free but is constrained by a third layer generally made of a stiff material (see Fig. 1.2(b)); in this case, the dissipation is mainly due to shear strains [126]

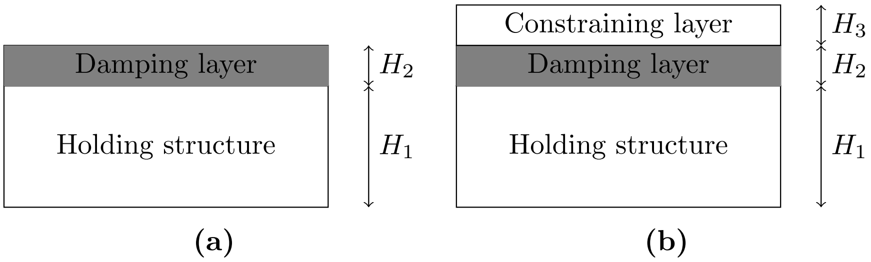

Figure 1.2: Scheme of surface damping techniques: (a) free layer (extensional damping), (b) constrained layer (shear damping).

and the parameter of interest is the complex shear modulus G of the damping layer. The Ross-Ungar-Kerwin (RKU) model [116] estimates equivalent modal parameters for a three layers beam and generalise the result of [102] for two layers beams; more generally, several methods allows to estimate the behaviour of layered structures [62, 82, 26, 25]. Surface damping methods make use of viscoelastic materials and their efficiency are strongly related to the material characteristics. The choice of material and geometry allows an optimal configuration to be found for each specific case [116].

- Other passive damping methods include friction damping, where vibrational energy is converted to heat through friction of a moving part [32], or particle damping, where small sized granular particles move freely inside a cavity and dissipate energy through a combination of friction and loss mechanisms. Notably, there is a increasing interest for particle dampers inside the cells of honeycomb panels for spatial applications [92] (see Fig. 1.3).

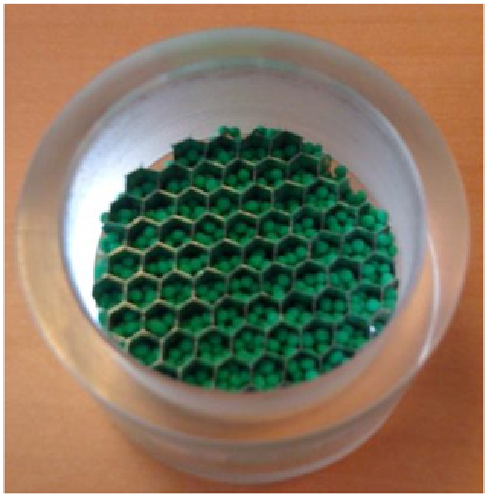

Figure 1.3: Box filled with particles in honeycomb cells (from [92]).

- For a given structure and for a given material, attenuating bending wave reflections at the edges is a way to reduce the resonant behaviour. An example of such boundary damping is given in the pioneer work of Vemula *et al.* [130] who propose to use a graded impedance interface at the edges of a beam, consisting in the association of several pieces of beams made with different materials (see Fig. 1.4). The results show that lower reflectivity is caused by energy dissipation within the composite material at the free end coupled with relatively large amplitude vibrations caused by the impedance gradation. This approach is similar to the Acoustic Black Hole approach developed in this document.

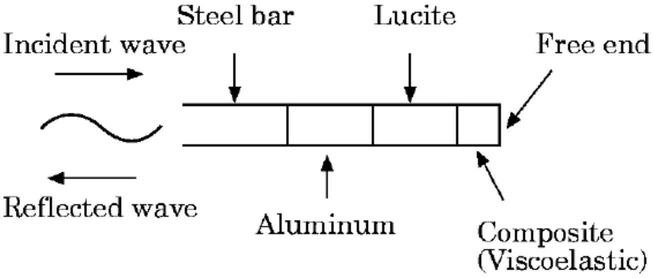

Figure 1.4: Graded impedance interface at the edge of a steel bar (from [130]).

1.1.2 Choice of the damping strategy: Ashby diagrams

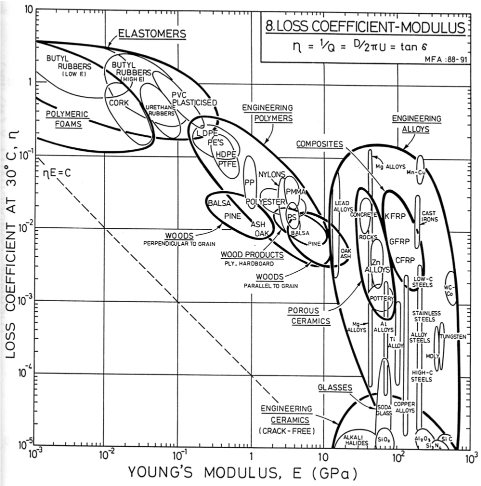

Figure 1.5: Ashby diagram for loss coefficient / Young's modulus (from [8]).

The choice of the damping strategy is made regarding the modal loss factors obtained on the treated structure, and it has been pointed out that the increase of mass is also an important criteria. Furthermore, an industrial part has to have a certain mechanical resistance, hence its static rigidity should not be too low. A way to compare the efficiency of damping strategies applied on a beam is to represent the specific Young's modulus E/ρ as a function of the loss factor of the structure. E/ρ is the ratio of the Young's modulus over the mass density of the treated beam. Such a representation, so-called Ashby diagram [8] (see Fig. 1.5 for example), is presented in Fig. 1.6. In this diagram, a treatment resulting in a stiff and light structure locates on the top while a treatment resulting in a damped structure is on the right side. Several materials and surface damping treatments are applied to a resonant free beam and can be compared on this diagram. For surface damping treatments (represented as lines), note that the performance depends on the beam thickness; several damping layer thicknesses are considered. Each points of each lines correspond to a different thickness H_2. For the sake of brevity, Appendix A.1 contains the material and thickness parameters (according to tabulated parameters in [100] or [21], summarised in Tab. A.1). Formulas used for the calculation in the case of constrained layer displayed in Appendix A.2.

Fig. 1.6 reminds that steel (▽) and aluminium (○) are weakly damped. It is also the case of the carbon composite that is shown (△) which has a remarkably high specific modulus. Polymer (□) and Sonoston (◁) illustrates that unfortunately, most of the materials having a high intrinsic loss factor have weak specific Young's modulus because of either high mass density or low Young's modulus. Fig. 1.6 also shows that covering the structure with a non-constrained layer (extensional damping, dashed lines) is not very attractive: a thin layer has little effect on the overall damping, while a thick layer increases the damping but with a decrease of the specific modulus. Finally, covering the structure with a constrained layer (full lines) has a very interesting effect on the damping but decreases the specific modulus due to an added mass.

The framework of this study can be summarised as filling the empty space of the top right hand corner of Fig. 1.6 where should be found the materials or damping techniques providing a high loss factor while keeping a high specific Young's modulus. The Acoustic Black Hole (ABH) effect as described in [93](works developed at Andreev Institute, Moscow, Russia), in [75](works developed at Loughborough University, United Kingdom) and in [57](works developed at Le Mans University, France) is particularly interesting in fulfilling this role.

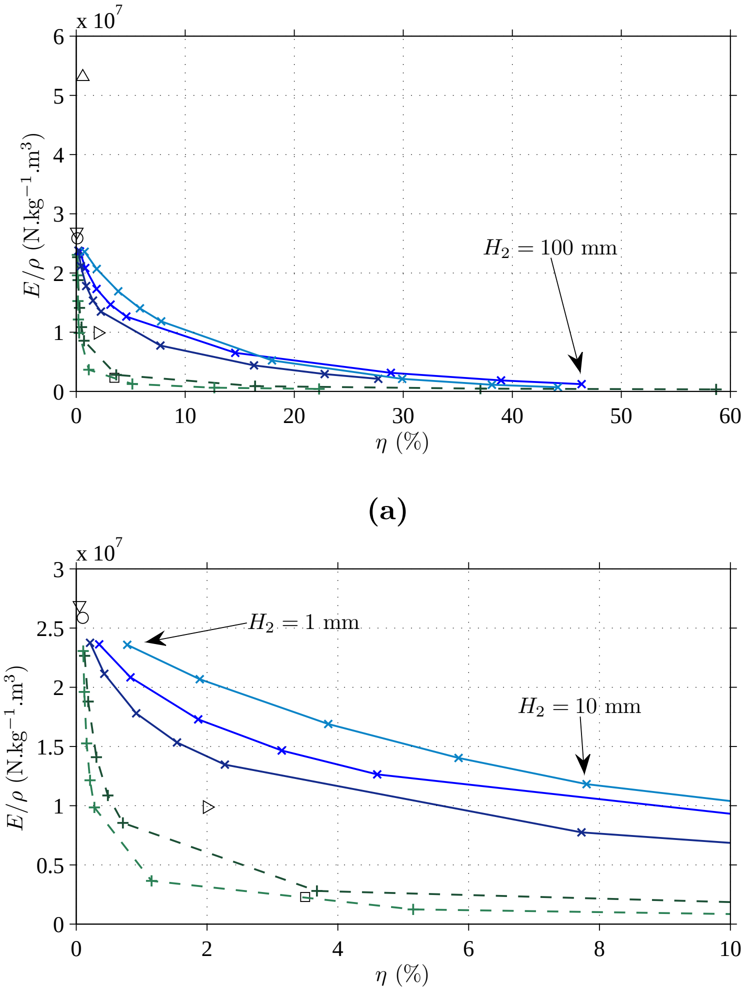

(a)

(b)

Figure 1.6: (a) Comparison of intrinsic loss factor η versus specific Young's modulus E/ρ for materials: aluminium (○), steel (▽), carbon composite (△), polymer FullCure (□), Sonoston (◁) and surface damping treatments: free layer on aluminium beam with damping layer made of Viton B (dashed line, +, dark green), Paracril BJ 50 (dashed line, +, light green), constrained layer on aluminium beam with damping layer made of Soundcoat DYAD (full line, x, medium blue), 3M ISD 110 (full line, x, dark blue), 3M ISD 112 (full line, x, light blue). Detailed material properties are given in Appendix A.1. (b) Zoom on the bottom left hand corner.

1.2 Literature review on the Acoustic Black Hole effect

The Acoustic Black Hole effect takes benefit of the wave properties in a plate or beam of decreasing stiffness in order to create an anechoic extremity. This section presents three description and main models of the phenomenon: the first one is proposed by Mironov [93] and yields a reflection coefficient for propagating bending waves in a tapered plate or beam extremity whose material properties are homogeneous. The second one is by Krylov *et al.* [77] and considers inhomogeneous material properties induced by a thin covering damping layer. Whereas these two models consider only propagating waves, a third approach by Georgiev *et al.* [57] considers propagating and attenuating waves in the inhomogeneous beam extremity.

1.2.1 ABH wave model based on geometrical acoustics assumptions - homogeneous material properties

Mironov shows, in the framework of geometrical acoustics, that flexural waves can propagate without being reflected in the extremity of a thin structure i.e. beam or plate whose thickness decreases with a power-law profile [93, 94]. Indeed, as the wave speed is proportional to the square root of the local thickness, if the thickness is slowly decreasing, the wave slows down without being reflected. The condition for slow variation of thickness, which is about small variations of the wave number over a distance of wavelength order,

$$\frac{\mathrm{d}k}{\mathrm{d}x}\frac{1}{k} \ll k, \tag{1.6}$$

is satisfied in particular by a power-law thickness (see Fig. 1.7(a))

$$h(x) = \epsilon x^m \quad m \geq 2. \tag{1.7}$$

Eq. (1.6) allows to apply the Wentzel-Kramers-Brillouin (WKB) approximation and write a solution for the displacement in the structure. The phase and group velocities c_ϕ and c_γ for bending waves are in this case obtained substituting Eq. (1.7) in their general expression for bending waves:

$$c_\phi(x) = \left(\frac{E\omega^2}{12\rho}\right)^{1/4}\sqrt{h(x)} = \left(\frac{E\omega^2}{12\rho}\right)^{1/4}\sqrt{\epsilon}x^{m/2}, \tag{1.8}$$

$$c_\gamma(x) = 2\left(\frac{E\omega^2}{12\rho}\right)^{1/4}\sqrt{h(x)} = 2\left(\frac{E\omega^2}{12\rho}\right)^{1/4}\sqrt{\epsilon}x^{m/2}. \tag{1.9}$$

Eq. (1.9) shows that the velocities tend to zero when x tends to zero. Moreover, the transit time τ of a wave packet between the abscissas x_i and x_t is

$$\tau = \int_{x_i}^{x_t} \frac{1}{c_\gamma(x)}\,\mathrm{d}x = \frac{1}{2\sqrt{\epsilon}}\left(\frac{12\rho}{E\omega^2}\right)^{1/4}\int_{x_i}^{x_t}\frac{1}{x^{m/2}}\,\mathrm{d}x, \tag{1.10}$$

yielding for $m = 2$

$$\tau_{m=2} = \frac{1}{2\sqrt{\epsilon}} \left(\frac{12\rho}{E\omega^2}\right)^{1/4} \ln\left|\frac{x_t}{x_i}\right|. \tag{1.11}$$

Note that in Eq. (1.10), the integral diverges when x_t=0 for any $m \geq 2$ which translates into an infinite transit time between the x_i and x_t; it means in this case that the bending waves slow down, eventually stop and do not reach the extremity of the profile. Retrospectively, Mironov *et al.* [94] mention the term "Vibrational Black Hole" for such an extremity.

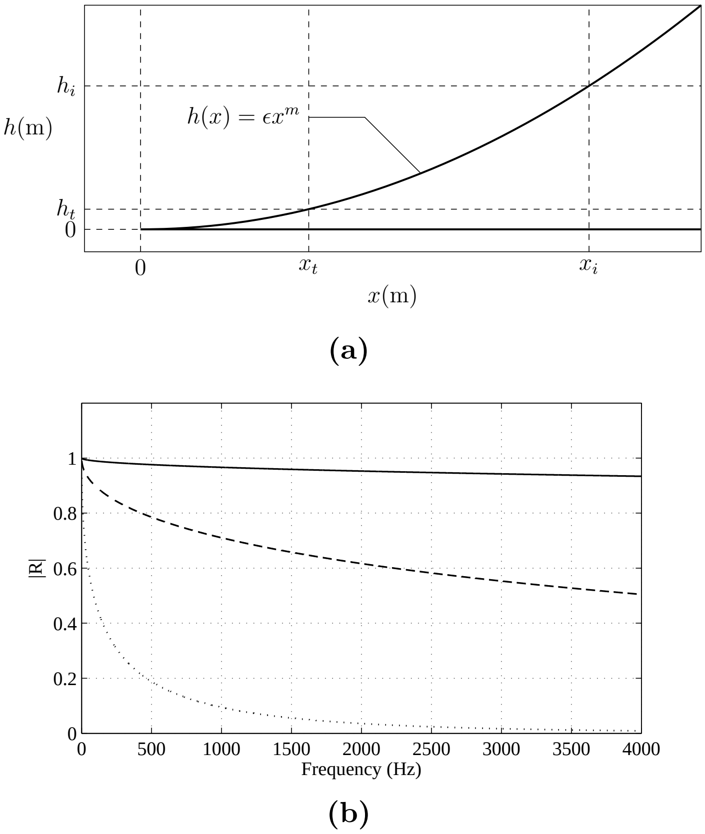

Figure 1.7: (a) Power-law thickness profile of an ABH (after Mironov [93]). (b) Reflection coefficient computed with Eq. (1.13) with ϵ=0.35, x_i=0.00653 m, x_t=0.0053 m, and (η=0.2 %, m=2) (full line), (η=2 %, m=2) (dashed line) or (η=0.2 %, m=4) (dashdotted line).

In a structure made of dissipative material, the Young's modulus is complex and so is the wavenumber $k_f = \sqrt[4]{\omega^2 12\rho(1-\nu^2)/Eh^2}$, therefore the travelling waves are attenuated. The integrated space rate of attenuation between x_i and x_t is $\int_{x_i}^{x_t} \mathrm{Im}(k(x))\,\mathrm{d}x$. For a extremity truncated at x_t (see Fig. 1.7), Mironov [93] proposes an expression for the the reflection coefficient:

$$R = \exp\left(-2\int_{x_i}^{x_t} \mathrm{Im}(k_f(x))\,\mathrm{d}x\right). \tag{1.12}$$

In the case where $m = 2$, the reflection coefficient writes

$$R = \exp\left(-2\left(\omega^2 \frac{12\rho}{E_0}\right)^{1/4} \frac{\eta}{1+\eta^2} \frac{1}{\sqrt{\epsilon}} \ln\left|\frac{x_t}{x_i}\right|\right), \tag{1.13}$$

which tends to zero with x_t, showing that any non-zero damping is sufficient to totally absorb the wave. However, Mironov shows that even if the plate thickness varies by three orders of magnitude, the loss factor of common materials does not allow to obtain an attractive reflection coefficient. This is illustrated on Fig. 1.7(b) for an extremity made of aluminium with m=2, η=0.1%, ϵ=0.35, x_i=0.0653 m and x_t=0.0053 m (h_t=10 μm and h_i=1.5 mm)(full line). The reflection coefficient tends to zero with the frequency but the reflection coefficient is still high. Two variations from this configuration are also plotted: the configuration (η=0.1%, m=4) (dashdotted line) seems very interesting at first sight but necessitates a terminal thickness of h_t=0.2 nm. The configuration (η=2%, m=2) (dashed line) yields a reflection coefficient that can be as low as 0.5.

In such a configuration of ABH, a low reflection coefficient can be obtained by either an atomical terminal thickness or a high material loss factor.

Note that in order to make the effect described in [93] more interesting practically, Pislyakov *et al.* [111] study the case of beams and disc plates with tapered edges whose very tip is coated, so that the reflection coefficient at the boundary condition is not unity.

1.2.2 ABH wave model based on geometrical acoustics assumptions - non-homogeneous material properties

Using the expression (1.12) for the reflection coefficient, Krylov *et al.* [77, 75, 78] propose to decrease the reflection coefficient by increasing the imaginary part of the wavenumber. This is realised by covering the truncated tapered extremity with a thin viscoelastic layer (see Fig. 1.8(a)) and allows to compensate the finite thickness of power-law profile. The added layer is taken into account using the model from Ross-Ungar-Kerwin [116] which gives equivalent and inhomogeneous characteristics for the bi-laminated structure. In this model, the only attenuation mechanism is the one associated with extensional deformations.

Assuming that the added layer thickness is weak regarding the plate thickness, the Ross-Ungar-Kerwin model [116] can be simplified writing an equivalent material loss factor due to the viscoelastic layer

$$\eta(x) = \eta_p + \frac{3h_l E_l}{h(x)E_0}\eta_l, \tag{1.14}$$

where h_l, E_l and η_l are the thickness, Young's modulus and loss factor of the layer, respectively. Under these conditions, the reflection coefficient writes, with $m = 2$

$$R = \exp\left(-2(\kappa_b + \kappa_l)\right), \tag{1.15}$$

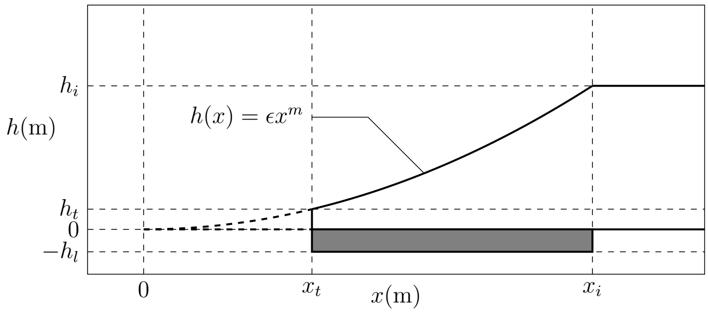

(a)

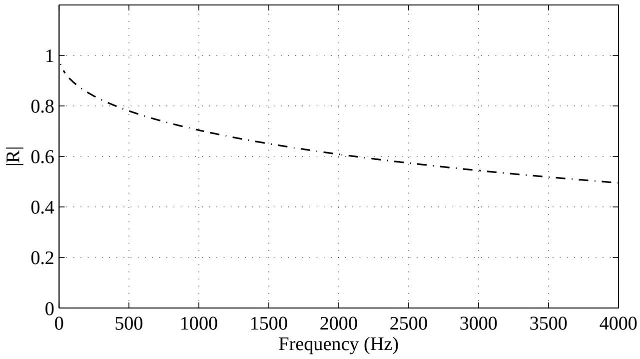

(b)

Figure 1.8: (a) Side view of a beam with acoustic black hole extremity covered with a damping layer. (b) Reflection coefficient computed using Eq. (1.18) for aluminium ABH with ϵ=0.35, x_i=0.0653 m, x_t=0.0053 m, m=2, E_l=7 GPa, ρ_l=1000 kg.m^{-3}, η_l=0.4, h_l=0.1 mm.

where the non dimensional parameters κ_b and κ_l are [77]:

$$\kappa_b = \left(\frac{12\rho}{E_0}\right)^{1/4} \frac{\omega^{1/2}\eta_p}{4\epsilon^{1/2}} \ln\left(\frac{x_t}{x_i}\right), \tag{1.16}$$

and

$$\kappa_l = \left(\frac{12\rho}{E_0}\right)^{1/4} \frac{3\omega^{1/2}\eta_l h_l}{8\epsilon^{2/3}} \frac{E_l}{E_0} \left(\frac{1}{x_t^2} - \frac{1}{x_i^2}\right). \tag{1.17}$$

The main interest of this approach consisting in adding a viscoelastic layer is that the reflection coefficient can now be very weak even if the profile is truncated.

Eqs. (1.14) and (1.15) are valid only if the layer is much thinner than the plate, which cannot always be verified in practice, particularly near the edge of the profile where the plate thickness is very weak. Krylov *et al.* [75] propose to take into account an arbitrary layer thickness in the model. Assuming $E_l/E_0 \ll 1$, the imaginary part of the flexural wavenumber is

$$\mathrm{Im}\left(k_f(x)\right) = \frac{(\frac{12\rho}{E_0})^{1/4}\omega^{1/2}(1+\frac{\rho_l h_l}{\rho h(x)})^{1/4}(\eta_p + \eta_l\frac{E_l}{E_0}(3\frac{h_l}{h(x)} + 6(\frac{h_l}{h(x)})^2 + 4(\frac{h_l}{h(x)})^3))}{4h(x)^{1/2}(1+\frac{E_l}{E_0}(3\frac{h_l}{h(x)} + 6(\frac{h_l}{h(x)})^2 + 4(\frac{h_l}{h(x)})^3))^{5/4}}. \tag{1.18}$$

The corresponding reflection coefficient is obtained by numerical integration of Eq. (1.15). Fig. 1.8(b) shows the result of a computation of R using Eq. (1.18) on an aluminium beam with m=2, a minimum thickness h_t=10 μm (ϵ=0.35, x_i=0.0653 m, x_t=0.0053 m) and a damping layer with characteristics: E_l=7 GPa, ρ_l=1000 kg.m^{-3}, η_l=0.4, h_l=0.1 mm. The reflection coefficient in this case reaches 0.5 at 4 kHz.

1.2.3 ABH wave model based on plane wave assumption - inhomogeneous material properties

The ABH extremity can be seen as an heterogeneity in a structural waveguide constituted by the beam. Several techniques exist in the literature to describe the vibratory field and compute a reflection coefficient: transfer matrix, scattering matrix, impedance matrix, *etc.* [85, 101, 46]. If one considers the attenuating waves, impedance matrix method is the more efficient. Georgiev *et al.* [57] propose a model that takes into account the attenuating part of the wave field to compute the reflection coefficient of an ABH beam extremity using an impedance matrix technique. Following the Euler-Bernoulli assumptions, the cross-section remains undeformed during the vibration. All points of the cross-section are thus in phase, which is the main characteristic of a plane wave. This model is numerically solved and allows to observe the effect of arbitrary spatially varying parameters. By considering the attenuating waves, a reflection matrix is obtained instead of a reflection coefficient.

The equation of flexural motion for a beam in harmonic regime (with a $e^{\mathrm{j}\omega t}$ time dependence), under the Euler-Bernoulli assumptions, can be written under the matrix formulation [133, 97, 54]

$$\frac{\mathrm{d}}{\mathrm{d}x}\mathbf{W} = \mathbf{H}\mathbf{W}, \tag{1.19}$$

where

$$\mathbf{W}(x)=\left[\begin{array}{c} w(x)\\ \theta(x)\\ V(x)\\ M(x)\end{array}\right], \tag{1.20}$$

is the state vector, with the flexural displacement w, the slope θ, the total shear force V and the bending moment M. Matrix $\mathbf{H}$ is in this case given by

$$\mathbf{H}=\left[\begin{array}{cc} \mathbf{H_1} & \mathbf{H_2}\\ \mathbf{H_3} & \mathbf{H_4}\end{array}\right], \tag{1.21}$$

where

$$\begin{gathered}\mathbf{H_1}=\left[\begin{array}{cc} 0 & 1\\ 0 & 0\end{array}\right], \quad \mathbf{H_2}=\left[\begin{array}{cc} 0 & 0\\ 0 & 1/EI(x)\end{array}\right],\\ \mathbf{H_3}=\left[\begin{array}{cc} -\rho b h(x)\omega^2 & 0\\ 0 & 0\end{array}\right], \quad \mathbf{H_4}=\left[\begin{array}{cc} 0 & 0\\ -1 & 0\end{array}\right],\end{gathered} \tag{1.22}$$

and where ω is the angular frequency, b and $h(x)$ are the width and the thickness of the beam, respectively, ρ is the mass density, $EI(x)$ is the local bending stiffness. The relation between kinematic and force variables at any point x is given by

$$\left[\begin{array}{c} V(x)\\ M(x)\end{array}\right]=\mathrm{j}\omega\mathbf{Z}(x)\left[\begin{array}{c} w(x)\\ \theta(x)\end{array}\right], \tag{1.23}$$

where $\mathbf{Z}(x)$ is the local impedance matrix of the beam. Substituting Eq. (1.23) in Eq. (1.19) permits to obtain the Riccati equation in $\mathbf{Z}(x)$:

$$\frac{\mathrm{d}\mathbf{Z}}{\mathrm{d}x}=-\mathbf{Z}\mathbf{H_1}-\mathrm{j}\omega\mathbf{Z}\mathbf{H_2}\mathbf{Z}+\frac{\mathbf{H_3}}{\mathrm{j}\omega}+\mathbf{H_4}\mathbf{Z}. \tag{1.24}$$

The reflection matrix $\mathbf{R}(x)$ of the extremity between 0 and x is then defined by

$$\mathbf{V}_-=\mathbf{R}(x)\mathbf{V}_+. \tag{1.25}$$

where $\mathbf{V}_-$ and $\mathbf{V}_+$ can be interpreted as the backward and forward wave vectors at x. The wave vector $\mathbf{V}$

$$\mathbf{V}=\left[\begin{array}{c} \mathbf{V}^-\\ \mathbf{V}^+\end{array}\right], \tag{1.26}$$

is linked to the state vector $\mathbf{W}$ by the relation

$$\mathbf{W}=\mathbf{E}\mathbf{V}, \tag{1.27}$$

with $\mathbf{E}$ the matrix containing columnwise the eigenvectors of $-\mathrm{j}\mathbf{H}$:

$$\mathbf{E}=\left[\begin{array}{cc} \mathbf{E}_1 & \mathbf{E}_2\\ \mathbf{E}_3 & \mathbf{E}_4\end{array}\right], \tag{1.28}$$

where $\mathbf{E}_1$ to $\mathbf{E}_4$ are 4×4 matrices.

It can be shown that the relation between $\mathbf{R}(x)$ and $\mathbf{Z}(x)$ is

$$\mathbf{R}(x) = (\mathrm{j}\omega\mathbf{Z}(x)\mathbf{E}_2 - \mathbf{E}_4)^{-1}(\mathbf{E}_3 - \mathrm{j}\omega\mathbf{Z}(x)\mathbf{E}_1). \quad (1.29)$$

Specifying characteristics of the beam and the viscoelastic layer, using the same model for the bending stiffness of the bi-laminated structure as in the model of [75], and $\mathbf{Z} = \mathbb{O}$ as the initial condition for the impedance, the model is solved numerically using a fourth-order Runge-Kutta algorithm. The first term R of the reflection matrix concerns forward and backward propagating waves and its evolution with x is plotted in modulus on Fig. 1.9 for several values of η_l, showing the decrease of $|R|$ with η_l.

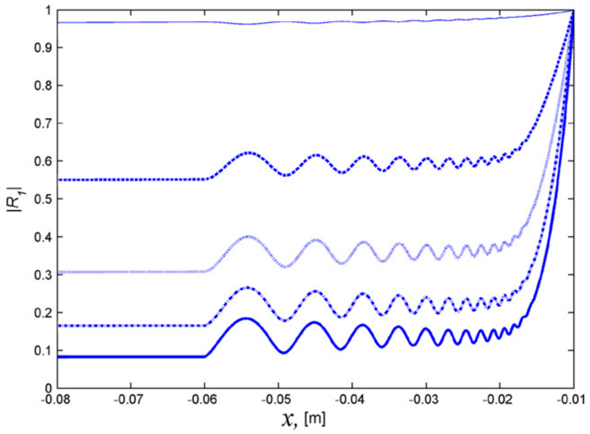

Figure 1.9: Evolution with x of the first term of the reflection matrix function for several values of η_l (from [57]).

1.2.4 Comparison of existing ABH models

Using the parameters given in Tab. 1.1, Fig. 1.10 compiles the results of the three models or [93, 75, 57] for the reflection coefficient. It is emphasized that for the same geometrical parameters, Mironov's ABH is completely inefficient while the two others provide low reflection. Models of Krylov and Georgiev yield a similar order of magnitude but the model including attenuating waves provides a reflection coefficient which oscillates with frequency, while the geometrical model of [77] gives a monotonous behaviour. Moreover, the reflection coefficient is also lower in modulus for the model of Georgiev. Note that this model [57] provides a complex value for R, yielding a modulus and a phase, while in the literature, the two geometrical models only mention the modulus.

1.2.5 Two-dimensional ABH

An implementation of a circular ABH, as a development of the one-dimensional profile is proposed by Refs. [53]. It shows good experimental results when the ABH works in

Geometrical parameters	Material parameters
ϵ=0.35, m=2	E=70 GPa, ρ=2700 kg.m^{-3}
x_i=0.0653 m, x_t=0.0053 m	E_l=7 GPa, ρ_l=1000 kg.m^{-3}
h_l=0.1 mm	η_p=2 %, η_l=40 %

Table 1.1: ABH parameters used in the comparisons of the three ABH models.

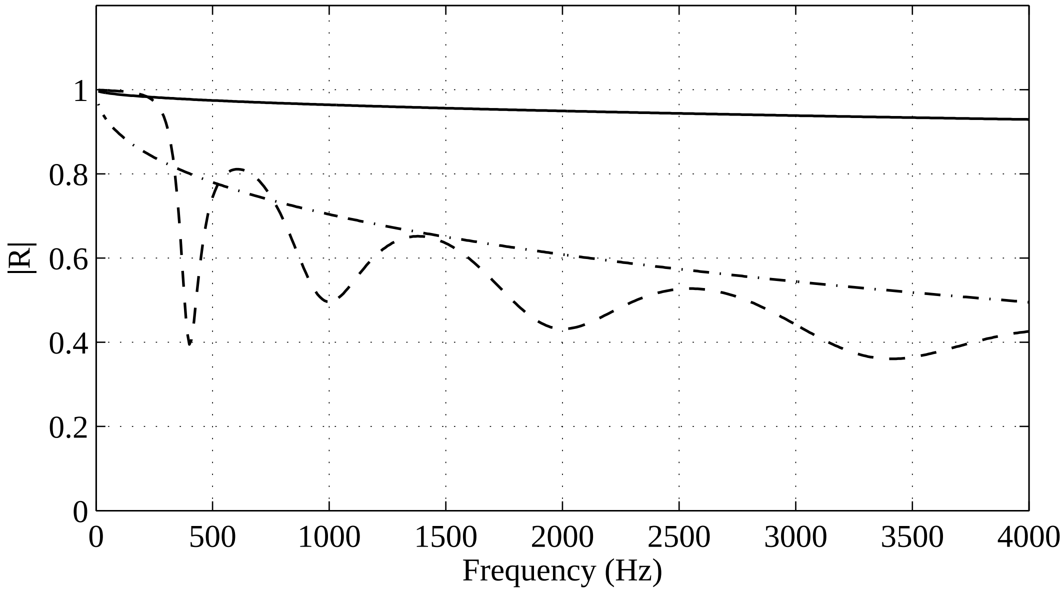

Figure 1.10: Comparison of the modulus of reflection coefficient R of ABH termination, predicted by three models described in [93] (full line), in [77] (dashed dotted line) and in [57] (dashed line), with parameters of Tab. 1.1.

conjunction with a stiffener or a parabolic edge to concentrate the waves towards the ABH. Fig. 1.11 (from [57]) shows the displacement field in an elliptic plate containing an circular ABH profile in one of its foci and the mobility transfer function of this plate.

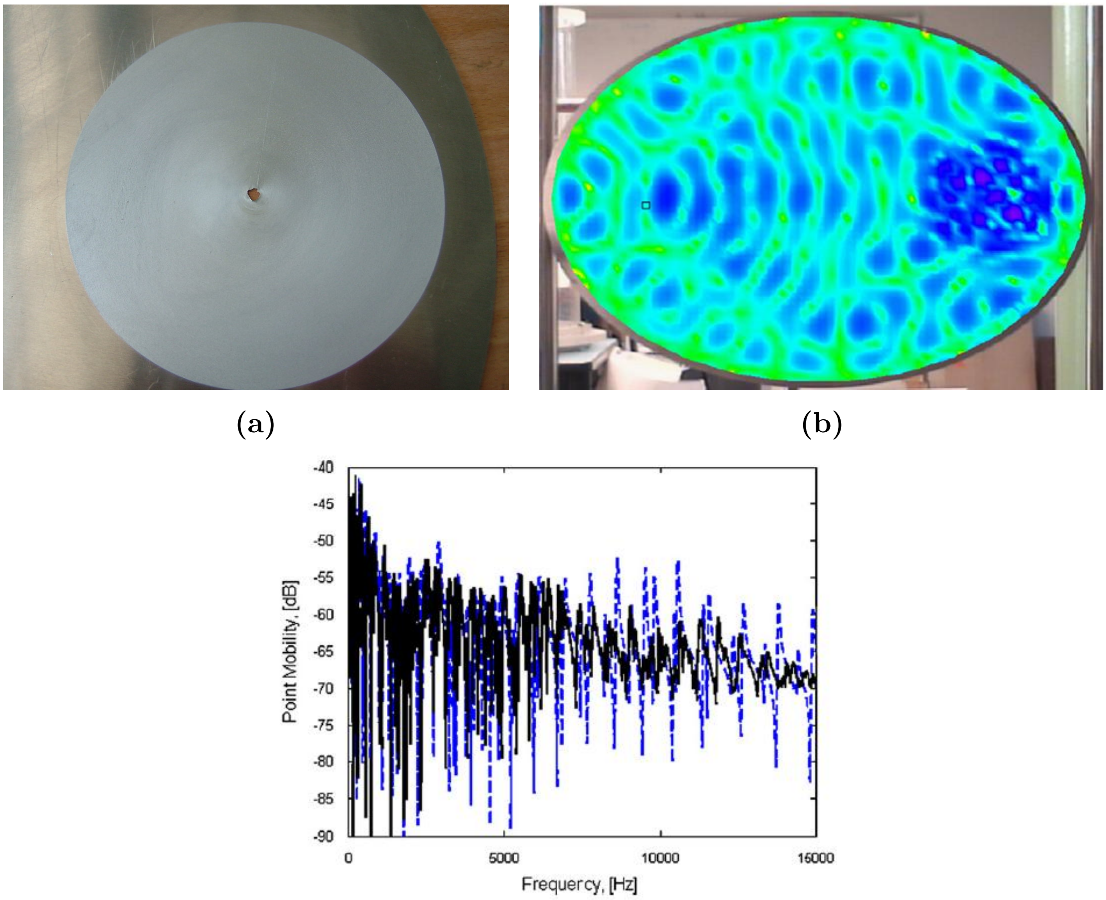

(a) (b)

(c)

Figure 1.11: (a) Black hole pit presenting a small truncation radius at its centre. (b) Displacement field of an elliptic plate containing an circular ABH in one of the foci. (c) Mobility transfer function of the same plate (from [57]).

O'boy *et al.* [104, 103] provide numerical wave-based models for computing the displacement field and frequency response in a rectangular plate simply supported along two-opposite edges with ABH free edge and a circular plate with circular ABH at the centre. The effect of the ABH addition is quantified by looking at the resonance peaks amplitude in the frequency responses. Ref. [103] provides as well a study on the use of a constrained layer and make use of an equivalent loss factor for the whole ABH region in the model.

Note that 2D circular ABH are just now extensively studied at Le Mans University in the the framework of the VIBROLEG project, supported by the IRT Jules Vernes (Institut de Recherche Technologique). In this project, 2D ABH are investigated for plate vibration damping (PhD work of O. Aklouche, 2012-2015). The flexural vibration field resulting from the interaction between an incident plane wave propagating in an infinite plate and a 2D ABH is studied. The capability of the ABH to scatter the incident wave is described by the scattering cross section σ whose a detailed model is currently developed [4, 5]. In the high frequency range, low value of σ (see Fig. 1.12) show the efficiency of the 2D ABH.

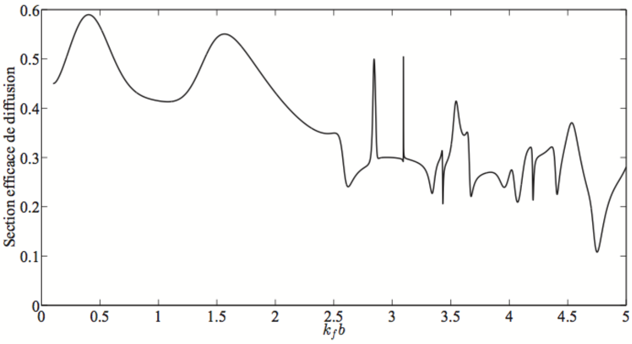

Figure 1.12: Scattering cross section σ of a circular ABH (from [5]).

1.2.6 Experimental works and ABH applications and state of the art in 2014

Efficiency of ABH effect in vibration damping is shown in several papers:

- An interesting application is proposed by Kralovic and Krylov [73], who implement a shaft tapered according to a quadratic law and covered with an adhesive film of absorbing material on a Badminton racket. The reflection of flexural waves coming from the net and racquet head thus leading to reductions of 10-15 dB on the resonance peaks at mid and high frequencies.
- Bowyer *et al.* [19] study experimentally the effect of deviation of a manufactured edge from a ideal profile (i.e. imperfections), but compare a imperfect termination with a shorter thus thicker perfect termination. They conclude that even imperfect, the thinner the better. They also study experimentally the implementation of several circular tapered profiles on plate [18] (see Fig. 1.13).
- Another application is developed in the work of Bowyer *et al.* [17] who implement an ABH termination on the trailing edge of a turbine fan blade (see Fig. 1.14). The application is interesting as fan blade vibrations generate broadband resonant noise. Results are conclusive and the system can be conceived such that it does not modify the air flux on the fan blade, by integrating the quadratic profile and the viscoelastic material in the blade profile.
- Foucaud *et al.* [52, 51] build an artificial cochlea and use an ABH extremity as an anechoic termination in his experimental setup (see Fig. 1.15). The experimental work is in agreement with theoretical models for cochlea, suggesting that the ABH termination fulfil its role in this case.

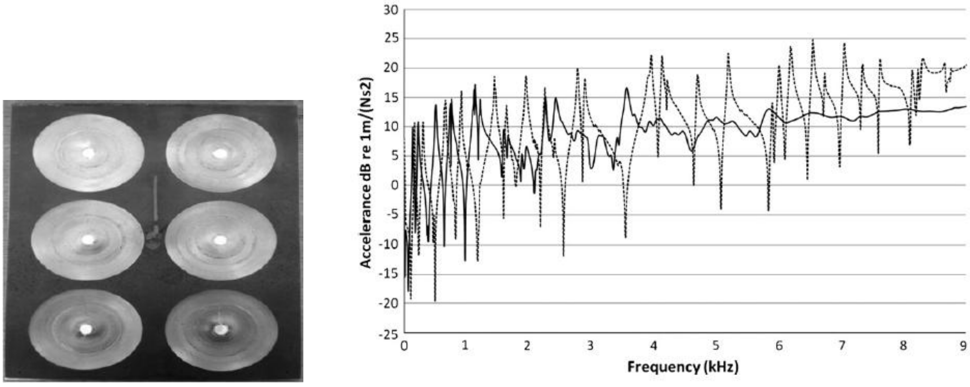

(a) (b)

Figure 1.13: (a) Plate containing six tapered indentations and (b) accelerance for uniform plate and plate with six indentations (from [18]).

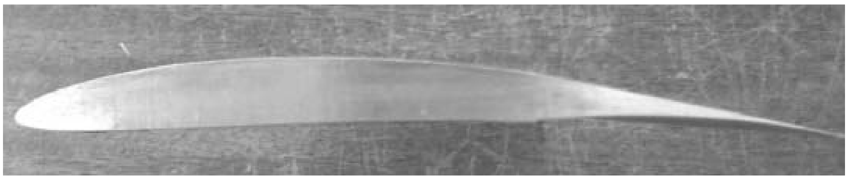

Figure 1.14: Turbine fan blade integrating an ABH extremity on the trailing edge (from [17])

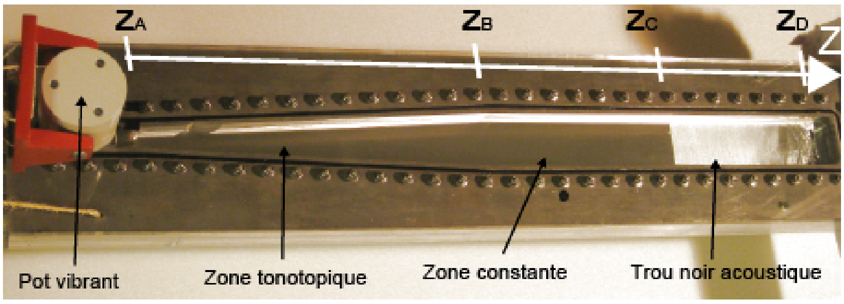

Figure 1.15: Experimental setup showing an artificial cochlea implementing an ABH (indicated as *Trou Noir Acoustique*, from [52]).

- Recently, Zhao *et al.* [138] use a power-law profile coupled with surface-mounted piezo-transducer to build an energy-harvesting system (see Fig. 1.16). They note that the ABH profile is a high energy density zone which can increase the efficiency of absorption mechanisms.

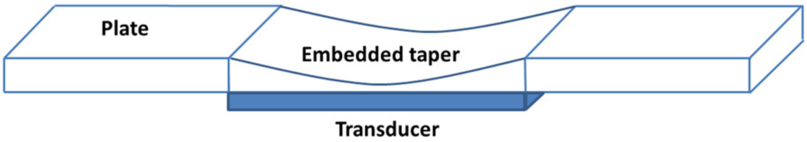

Figure 1.16: Plate embedding an ABH and a surface-mounted transducer (from [138]).

ABH in LAUM

Work on the acoustic black hole effect is ongoing in LAUM. Contributions to the field are found in the PhD thesis of Cuenca [29, 31, 30] and the post-docs of Georgiev [57, 55, 58, 56]. The scattering of a circular ABH profile is one of the main objectives of the ongoing PhD thesis of Aklouche [5, 4]. The subject also participates to education in Université du Maine: M2 research interships of Moleron [96], Barguet [10] focus on the implementation and characterisation of two-dimensional ABH in plates. M2 research internships of Poittevin [112] and Faure [45], and engineer internship of Dufort [41] concern the measurement of the reflection coefficient of a beam having an ABH termination.

1.3 Astrophysical Black Holes and analogues

In astrophysics, the concept of black hole is first described by Schwarzschild [121], based on Einstein relativity. Wheeler [135] is usually credited for naming the object *black hole*. It is a celestial object whose gravity is such that its escape speed is higher than the speed of light, so that even light cannot escape it. Black holes can indirectly be observed as an important source of X rays. It is a very popular research field in physics. Recently, Hawking has emitted the controversial hypothesis that all absorbed information would eventually come out of the black hole in a mangled form [64].

Analogue black holes have been described and eventually practically realised in laboratory experiments. They are used to confirm theories on quantum black holes, which have not been actually observed. Unruh [127] shows that a sound wave in a convergent fluid flow behaves like a quantum field in a classical gravitational field, and proposes a way to experiment black hole evaporation and observe Hawking radiation [63]. This sonic or acoustic analogue to black hole is then called "Dumb hole" to perfect the analogy [128] and have since been studied extensively [131]. Optical black hole have been described [129] as a region where the light is slowed down until its speed is inferior to the rotating speed of a spinning medium; it induces an event horizon but does not allows the observation of Hawking radiation.

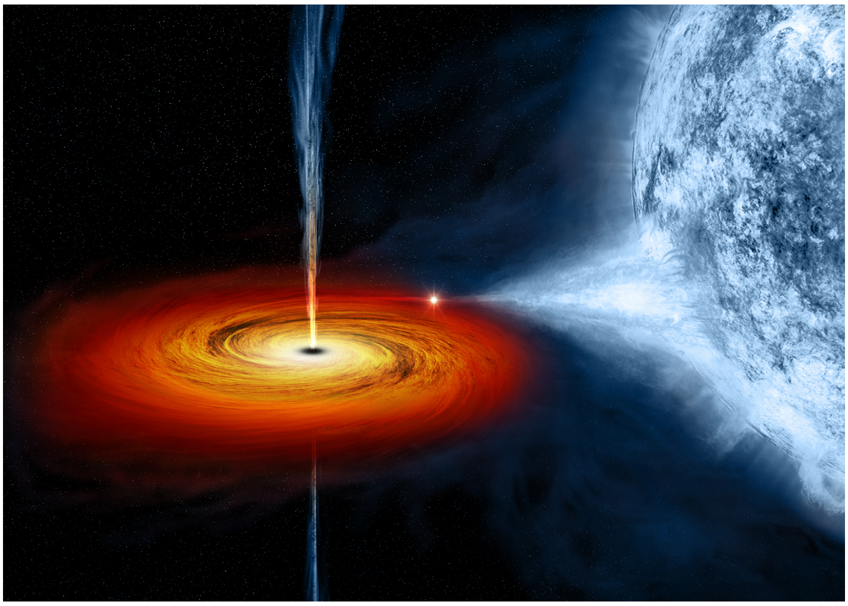

Figure 1.17: Artist's view of an astrophysical black hole, from [99].

The original work of Mironov [93] do no mention the term black hole, but the term can be found in later papers [111, 95]. Ref. [111] mentions that a tapered beam whose thickness reaches zero can be called "vibrational black hole" as the absorption is not due to the transition of energy of vibration to heat but to its accumulation in the vicinity of the border of the plate. Ref. [95] refers to "Acoustic Black Hole" as a retarding structure allowing the sound speed decreases progressively to zero in an tube, based on a decrease of the acoustic admittance of the walls of the tube; a practical case where the zero speed is not reached is also mentioned. Although the "Acoustic Black Hole" term is also used here, it does not involve the same phenomena than the dumb hole described by [128] and may not be an analogue to the quantum black hole.

It appears that [77] forgot the term vibrational black hole and use instead acoustic black hole effect in the case of flexural waves in beam or plate structures, maybe because of the use of the geometrical acoustics and WKB solutions that are similar in principle in both descriptions. Later works [19] prefer the term of tapered edges or wedges. The term acoustic black hole effect, although erroneous, is chosen in this document mainly to stay coherent with the previous literature. It does not reflect an actual analogy since it is clear that the vibration energy is mostly dissipated in heat due to viscoelastic phenomena in a practical realisation. The author recognises that it participates (unfortunately or not) to give an esoteric side to a very practical, nevertheless interesting phenomenon.

1.4 Conclusions and objectives

The interest of the ABH effect for damping lightweight structures has been presented in this chapter through a literature review. It is possible to establish a graduation in the models. In the existing litterature, it is remarkable that there is few direct comparison between theoretical and experimental works. Moreover, a claim of the previous studies is that the ABH effect allows to obtain a quasi-anechoic termination; yet, most of the experimental studies observe frequency responses and not an actual reflection coefficient, which is a more direct indicator. Finally, it appears that the origins of the spectacular effects of adding an ABH should be analysed in depth: to the best of the author's knowledge, only the reductions in peaks amplitudes or their average has been used to quantify the effect of the ABH effect as a damping treatment.

The aim of this thesis is then twofold: to provide and use speaking indicator of the efficient of experimental implementations of ABH, and to give a more advanced explanation to the phenomenon, taking into considerations inhomogeneities of thickness and damping, and deviations from the theoretical profile.

Structure of the document

The document is organized in 5 chapters. Chap. 1 gives a brief state of the art of classical vibration damping methods, comparing their performance and their mass. The ABH effect is proposed as being as much or more efficient and lighter, and its interest is emphasised. Existing models from the literature, state of the art and related works are thoroughly described.

In Chap. 2, the ABH effect is investigated experimentally on beams, by observing it with different methods under the two paradigms of vibrations, the wave and the modal approaches. An experimental modal analysis with a high resolution technique is done showing an increase of the modal loss factors of the treated structure hence an increase of the modal overlap factor. In the wave paradigm, the ABH effect appears as a clear decrease of the reflection coefficient of the beam extremity.

In Chap. 3, the effect of the heterogeneity of the structure, brought by the ABH treatment, is studied analytically and numerically; two properties are playing a fundamental role: the stiffness heterogeneity and the damping heterogeneity. The ABH effect is the combination of the two. This is shown by an observation of a numerical model of ABH plate. Local eigenmodes are pointed out. Analytical development allows a better understanding of these effects: effect of the tapered profile on the modal density and effective length of the tapered profile are also discussed.

In Chap. 4, we propose to take into account imperfections at the tip of the tapered profile and show that they can be used to enhance the damping effect, by scattering an incident wave on heavily damped trapped transverse modes.

A general conclusion of the document in Chap. 5 sums up the different works and proposes several outlooks for future works.

Several journal papers written during the PhD are included as parts of this document. Refs. [38] covers Sec. 2.2 and the majority of Chap. 3 and is already published (it also appears in [35, 36]). Ref. [37] is under review and the core of its content represents

Sec. 2.3.2. Finally, the content of Chap. 4 will be submitted soon as a full length paper [34].

Chapter 2

Experimental evidence of the Acoustic Black Hole effect

This chapter aims to experimentally demonstrate the ABH effect on beams. In structural dynamics, two main approaches can be used to study a structure: wave propagation approach and modal approach. In the wave approach, the motion in the structure is the superposition of waves that can be attenuated in the structure media while they propagate, be multiply reflected on the boundary conditions or propagate to a surrounding media [2]. In the modal approach, a structure is represented by its eigenfrequencies and eigenmodes, which are complex in the general case. These approaches may be complementary, and it is interesting here to use them both to identify the effect of the ABH termination on a beam structure. In the modal approach, it is shown that the ABH effect is seen as an added modal damping while in the wave approach the ABH is seen as an anechoic termination which diminishes the reflection at the extremity. For each approach a rapid observation and a finer analysis are done considering an indicator adapted to the wave and modal approaches: the modal overlap factor or the reflection coefficient. The experimental works and analyses draw the lines of the subsequent chapters.

2.1 Description and manufacturing of ABH beams

Two kinds of processes can be proposed for manufacturing the tapered beams: classical machining process and prototyping process. These two processes orient the choice of the two constitutive materials which are used for the studied beams: aluminium and polymer (Vero White Plus FullCure 835). For each material, two beams are tested: a uniform beam (i.e. constant cross section) used as a reference, and a beam with an ABH termination, whose geometry is described on Fig. 2.1. A layer of damping material is

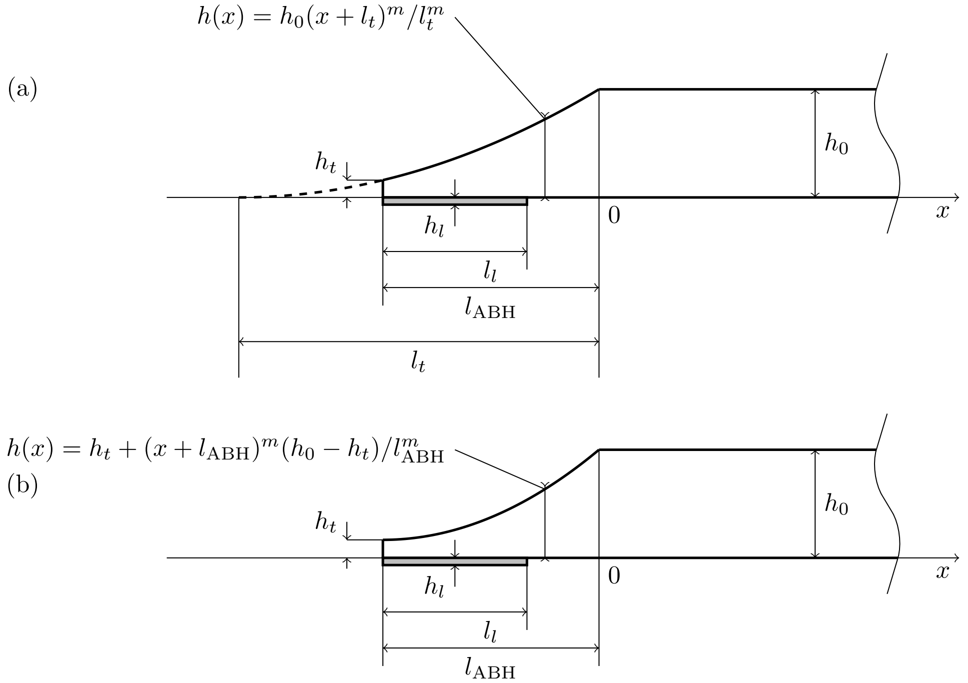

Figure 2.1: Scheme of the ABH profile at beam extremity for (a) aluminium and (b) polymer cases.

stuck on the flat side of the tapered profile. Several types of layer can be used: thick or thin tape made with viscoelastic materials. The dimensions and material (Young's modulus, mass density, loss factor and Poisson's ratio) characteristics of the samples are given in Tab. 2.1. Characteristics of the damping layer are order of magnitude given by the manufacturer.

Geometrical characteristics	Characteristics of material
Aluminium beam	
L=0.8 m, b=0.02 m,	E_1=70 GPa, η_1=0.2 %,
l_{ABH}=0.06 m, l_t=0.07 m,	ρ_1=2700 kg.m^{-3}, ν=0.3.
h_0=1.5 mm, m=2.	
Polymer beam	
L=0.6 m, b=0.02 m,	E_1=3.5 GPa, η_1=2.8 %,
l_{ABH}=0.06 m, h_t=0.16 mm	ρ_1=1175 kg.m^{-3}, ν=0.3.
h_0=1.5 mm, m=2.	
Damping layer	
h_l=0.1 mm,	E_2=7 GPa, η_2=40 %,
l_l=0.05 m.	ρ_2=1000 kg.m^{-3}.

Table 2.1: Geometrical and material characteristics of the sample beams and damping layer.

The ABH termination for the aluminium beam is manufactured using a conventional high speed machining process, allowing to obtain a minimum thickness at the extremity between 10 and 20 20 μm (see Fig. 2.2(a)). The process requires high precision work and often generates irregularities and tearing at the tip of the profile. The polymer beam is manufactured using UV polymerisation, which is a rapid prototyping process. This manufacturing process allows a thinner minimum thickness of about 16 μm and gives a better control on the profile but restricts the choice of the material (see Figs. 2.2(b) and (c)). A standard measurement of the complex Young's modulus versus frequency (based on a Dynamical Mechanical Analysis [91]) provides the mean value given in Tab. 2.1. Such measurement have been provided by the Centre de Transfert de Technologie du Mans (CTTM).

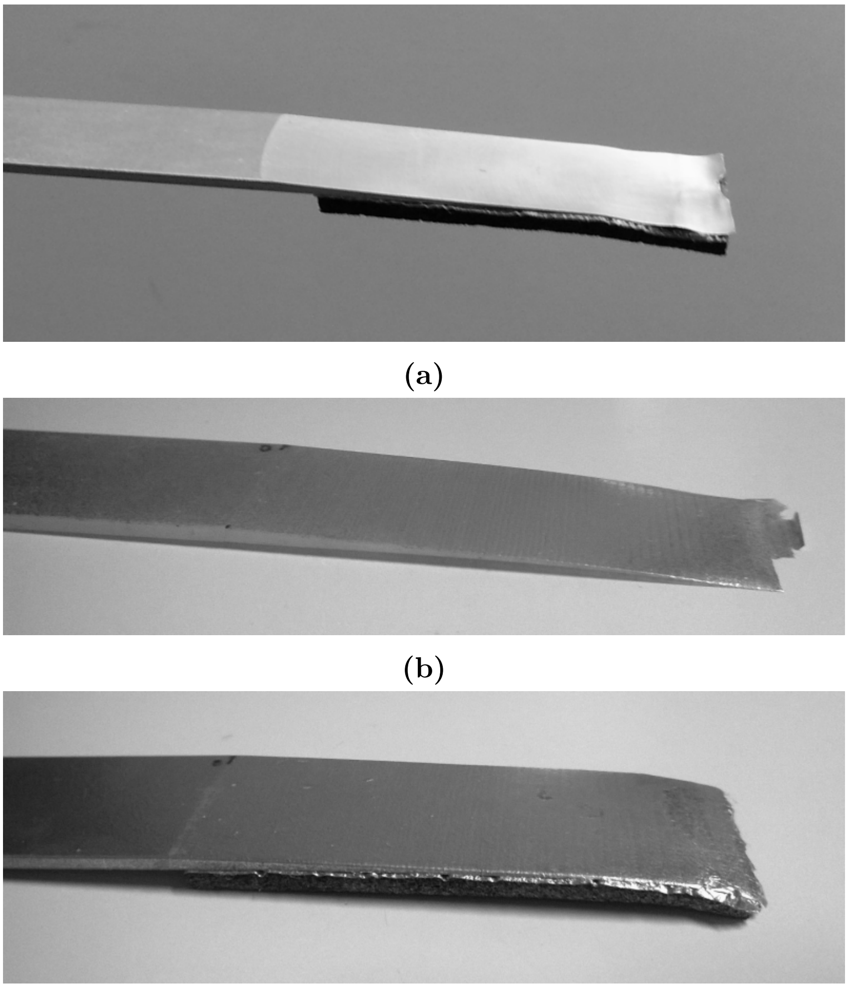

(a)

(b)

(c)

Figure 2.2: Pictures of ABH extremities (a) made of aluminium and covered, (b) made of polymer and non covered and (c) made of polymer and covered.

2.2 Increase of modal damping by ABH effect

Previous works [57] show the potential of ABH treatment for the reduction of the resonant behaviour of a structure. In this section, we propose to show how the addition of a ABH termination to a beam extremity leads to an increase of the modal overlap and the modal damping of this beam. For this purpose, the measurements of the modal characteristics of an uniform and an ABH beam are performed.

2.2.1 Experimental setup

Fig. 2.3(b) represents the experimental setup in which the sample to be tested is vertically suspended. To avoid unwanted additional damping caused by the suspensions, thin wires are glued to the side ridges of the beam. An miniature impact hammer (PCB Piezotronics 086E80) mounted on a flexible support excites the beam at one arbitrary point of its centerline in order to mainly excite flexural modes and to avoid torsional modes. A force sensor is embedded in the hammer and measures the impact force. At the same point, but on the back side of the beam, the measurement of acceleration of the beam is made by a miniature accelerometer (PCB Piezotronics 352C23, 0.3 g). The time signals are recorded by using a National Instrument NI USB-4431 acquisition card. The experimental set up is driven by a Matlab® application which also performs classical signal post-processing operations.

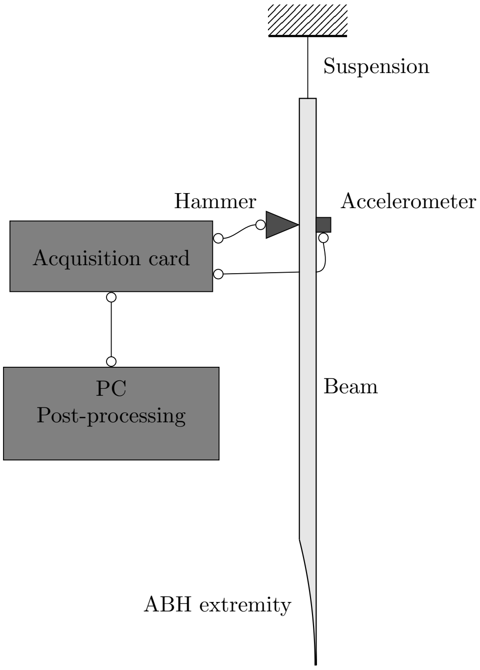

Figure 2.3: Scheme of the experimental setup representing the ABH beam, the accelerometer, the impact hammer and the acquisition system.

2.2.2 Frequency response

The mobility of the beam is defined by

$$Y_{ij} = \frac{V_i}{F_j}, \tag{2.1}$$

where V_i and F_j are the velocity at point i and the force applied at point j, respectively, and where V_i is computed from $V_i = \frac{a_i}{-\mathrm{j}\omega}$, with a_i the acceleration at point i. Fig. 2.4 presents these frequency response functions for the reference and the ABH beams. Clear reduction of the resonance peaks is observed.

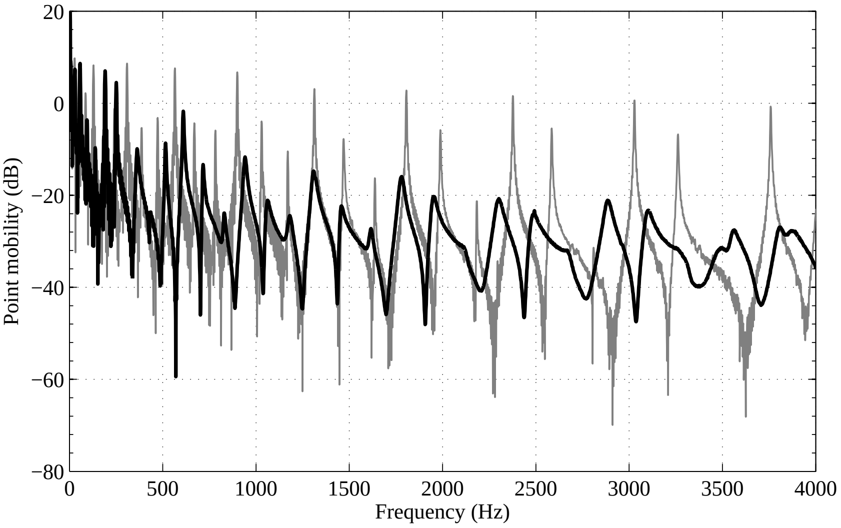

Figure 2.4: Comparison of the measured mobilities of the reference beam (thin full line, excitation and measurement point at 0.4 m of the free extremity) and the ABH beam (thick full line, excitation and measurement point at 0.5 m of the tip of the ABH).

2.2.3 Modal analysis

2.2.3.1 Choice of modal identification method

Many classical methods have been developed to identify eigenfrequencies, modal coefficients and mode shapes of a structure from a set of mobility transfer functions. In reference textbooks such as [44], different single degree-of-freedom techniques (-3dB method, circle fitting) or multiple degrees-of-freedom techniques (curve fit in the frequency domain, least square complex exponential method in the time domain) are presented. Since the modal overlap is expected to be large in the present case, those classic modal identification techniques may be no longer robust [89, 12]. Subspace methods like MUSIC (*MUltiple SIgnal Classification*) [119], Matrix Pencil [65], or ESPRIT (*Estimation of Signal Parameters via Rotational Invariance Techniques*) [117] are then interesting to consider and have already been successfully applied to vibration signals [81, 43]. Indeed, these methods overcome the Fourier resolution limit and are then useful when modes are overlapping, hence the designation *high-resolution* [42]. In this work, ESPRIT is used since it is known to be one of the more robust.

2.2.3.2 ESPRIT method

The velocity response $s(A,t)$ in any point A to an impulse force is modelled as the real part of a sum of complex damped sinusoids, each one being the time response of a mode:

$$s(A,t) = \mathrm{Re}\left[\sum_{k=1}^{K} b_k(A) z_k^t\right], \tag{2.2}$$

where $b_k(A)$ is the complex amplitude of the k-th mode and $z_k = \mathrm{e}^{-a_k + \mathrm{j}\omega_{dk}}$ denotes the corresponding pole with modal damped pulsation ω_{dk} and modal damping factor a_k. K is the number of complex poles in the frequency band $[-F_s/2 \quad F_s/2]$, where F_s is the sampling frequency.

The ESPRIT [117] algorithm estimates the signal parameters corresponding to the modal parameters of the K sinusoidal components embedded in the signal. Like other subspace high resolution methods (such as Matrix Pencil or MUSIC), it is based on the decomposition of the data vector space onto two orthogonal subspaces, the so-called signal and noise subspaces. Then, using the so-called rotational invariance property of the signal subspace (it remains invariant from a sample to the next), the poles z_k spanning the signal subspace can be estimated accurately. The reader can refer to Ref. [43] for a detailed description of the ESPRIT algorithm. The subspace decomposition and the use of the rotational invariance property make the ESPRIT method more robust and accurate than classic Prony-based method, such as LSCE [44] for instance.

The estimation of the model order K, related to the number of modes in the frequency band of analysis, is performed thanks to the signal enumeration technique ESTER (*ESTimation of ERror*), designed by Badeau *et al.* [9] and used by Ege *et al.* [42] and Elie *et al.* [43] in the context of musical acoustics. The ESTER criterion has been chosen among other signal enumeration techniques [134, 13, 3, 120, 24, 106] for its reliability and also for its straightforward implementation with the ESPRIT algorithm. This criterion consists in appraising the rotational invariance property of the signal subspace with an error function. This latter being minimal when the rotational invariance property is verified, namely when the modelling order is equal to the right number of sinusoidal components. Note that for impulse responses signal, which is real, the number of components K is twice the number of physical eigenmodes.

2.2.3.3 Results on modal parameters

2.2.3.3.1 Eigenfrequencies and modal loss factors

Modal parameters are estimated by applying the ESPRIT technique described in section 2.2.3.2 on the driving point mobility shown in Fig. 2.4. The method yields the complex poles of the signal, i.e. the eigenfrequencies and the damping coefficients of the tested beams. They are presented in Tab. 2.2 between 1000 and 2000 Hz for the aluminium reference and ABH beams. Fig. 2.5 presents a comparison of the experimental modal parameters between the aluminium reference beam (□) and the ABH beam (○).

An important increase of the modal loss factors is seen on Fig. 2.5(b) for the ABH case. Those of the reference beam, of uniform thickness and material properties, are almost constant against the frequency (*i.e.* independent of the mode) and are equal to approximately 0.2%. This expected weak constant value corresponds to the intrinsic material loss factor of the beam (aluminium) and to coupling with the air. The modal loss factors for the ABH beam are at least ten times higher than those of the reference beam and can reach about 4%

f_k^{Ref} (Hz)	1028.6	1167.0	1314.2	1468.4	1632.7	1806.7	1986.6
η_k^{Ref} (%)	0.17	0.31	0.21	0.29	0.30	0.15	0.25
f_k^{ABH} (Hz)	1006.8	1133.4	1272.9	1416.6	1574.9	1728.9	1887.9
η_k^{ABH} (%)	2.53	2.34	1.97	2.44	2.46	3.24	3.36

Table 2.2: Eigenfrequencies and modal loss factors for aluminium reference and ABH beams between 1000 and 2000 Hz.

2.2.3.3.2 Modal density

Since direct comparison between these eigenfrequencies f_k do not give comprehensive informations, we are more interesting by the study of the modal density $d(f_k)$. This modal density is related to the frequency spacing by the relation

$$d(f_k) = \frac{1}{f_{k+1} - f_k}. \tag{2.3}$$

From a practical point of view, d is obtained as a function of frequency by averaging the discrete values $d(f_k)$ over a sliding window containing a predefined number of modes (typically 5 modes). The theoretical prediction for the modal density of the reference uniform beam is given by the Euler-Bernoulli beam theory [137]:

$$d(f) = \frac{L}{\pi c_\gamma(f)} = \frac{L}{2\pi\sqrt{2\pi f}\sqrt{h_0}} \left(\frac{12\rho}{E}\right)^{1/4}. \tag{2.4}$$

On Fig. 2.5(a), the modal density of the reference beam fits very well with the theoretical prediction. These two results are in good agreement since particular attention has been paid to excite and measure the beam on its centreline: the vibrational field is almost entirely carried by the flexural modes, while the torsional modes only provide a very weak contribution. Fig. 2.5(a) also shows that the ABH termination used in this experiment does not lead to a substantial increase of the modal density. The modal density of the ABH beam is very similar to the one of the reference beam: in fact, it is very slightly higher as it will be explained in Sec. 3.2.3.

2.2.3.3.3 Modal Overlap Factor

The Modal Overlap Factor (MOF) is the ratio between the modal bandwidth at the half amplitude and the average modal spacing [89]:

$$\mathrm{MOF} = \frac{\Delta f_{-3\mathrm{dB}}}{f}. \tag{2.5}$$

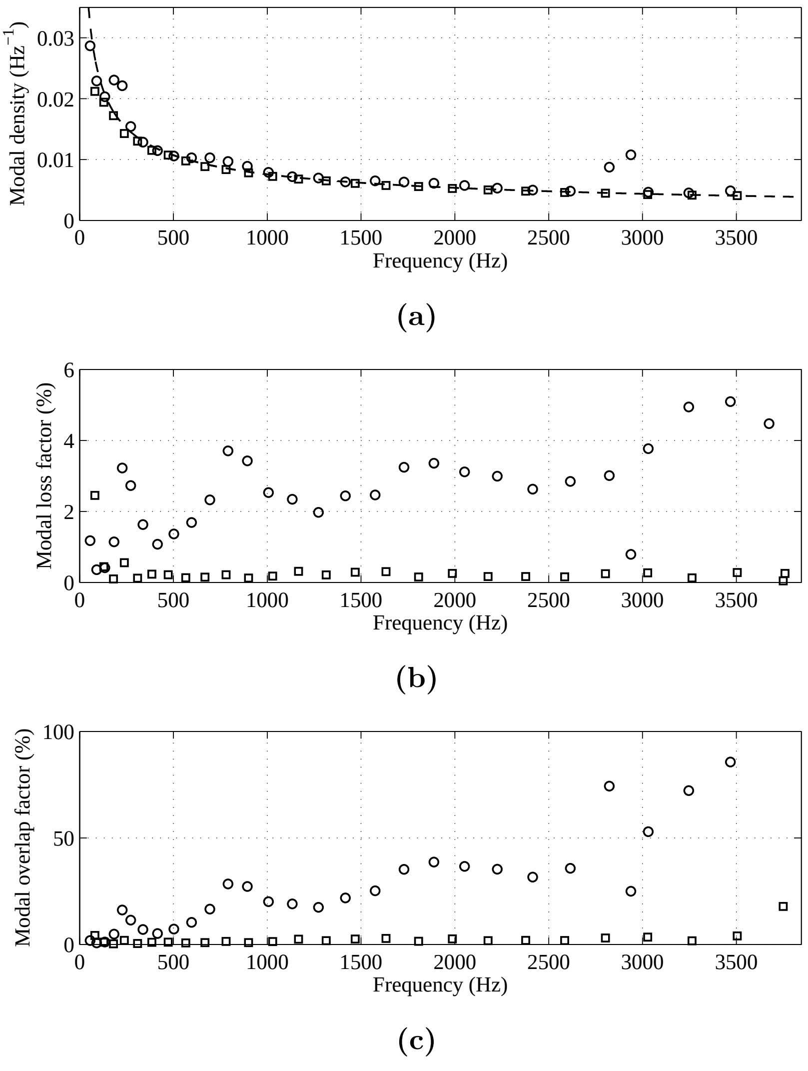

(a)

(b)

(c)

Figure 2.5: Comparison of experimental results between the aluminium reference beam (□) and the aluminium ABH beam (○): (a) Modal densities n and theoretical prediction for flexural waves in a uniform beam according to Eq. (2.4) (dashed line), (b) modal loss factors η, (c) Modal Overlap Factor MOF (published in [38]).

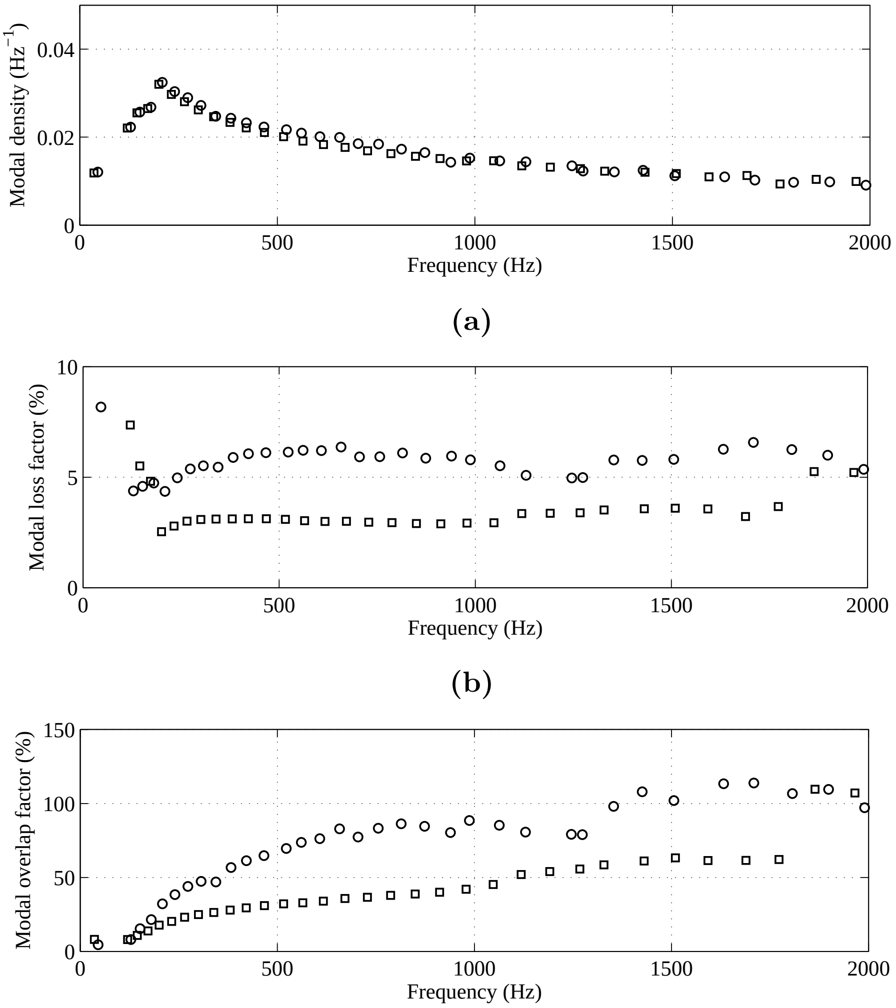

(a)

(b)

(c)

Figure 2.6: Comparison of experimental results between the polymer reference beam (□) and the polymer ABH beam (○): (a) Modal densities n and theoretical prediction for flexural waves in a uniform beam according to Eq. (2.4) (dashed line), (b) modal loss factors η, (c) Modal Overlap Factor MOF.

The MOF can also be calculated as the product [42, 12]

$$\mathrm{MOF} = d\eta f, \tag{2.6}$$

where d is the modal density, η is the modal loss factor and f is the frequency. In structural dynamics, the MOF can be used to establish three frequency ranges: the low frequency range (MOF<30%) in which the structure admits a resonant behaviour, the mid frequency range (30%<MOF<100%) in which the modal overlap and/or loss factor are higher, and the high frequency range (MOF>100%) in which diffuse field assumptions are reached. Diffuse field may easily be obtained in thin-walled structures; this is not the case for the beams presented in this study.

Fig. 2.5(c) shows that the ABH termination results in an increase of the MOF: while it barely reaches 5% for the reference beam, it is more than ten times higher and can reach 50% for the ABH beam above a starting frequency of efficiency (about 400 Hz). This strong increase of the MOF is directly related to the increase of the modal loss factors.

Finally, Fig. 2.5 shows that the result on the mobility seen in Fig. 2.4 corresponds to an important increase of the MOF which is essentially due to the ABH action on the modal loss factor. This result means that the ABH makes the structure vibrate in a frequency range intrinsically more damped. The reasons for this important increase are studied in Sec. 3.1.3, thanks to the numerical model developed in Sec. 3.1.1 and Sec. 3.1.2.

Modal parameters for the polymer beams are plotted on Fig. 2.6. The same tendencies than for the aluminium beams are observed in this case but somehow weakened: the modal loss factor of the reference beam are 3.5 %, corresponding the intrinsic loss factor of the material, but they reach 6.5 % in the ABH case. The same observation can be made on the MOF which is also approximately doubled.

2.3 Anechoic termination and progressive wave field

There exist few ways to passively reduce the vibration of a structure: one is to modify the material damping of the whole structure; one another is to reduce the reflection of the waves at its boundaries, so that an incident wave does not reflect back and cannot contribute to the vibration field in the structure. This section proposes to observe propagation of waves towards the ABH extremity and the reflection it induces.

2.3.1 Displacement field of the structure

To the author's knowledge, measured maps of the displacement field inside an ABH structure only appear in [57] on elliptic plates including ABH. This section proposes to observe how the ABH placed at the extremity modifies the displacement field. The displacement field is observed on the beam made of polymer, with or without a damping layer. A reference uniform beam of the same material is also observed for the sake of comparison (the geometries are indicated on Fig. 2.1 and in Tab. 2.1).

2.3.1.1 Experimental setup

In this experiment, the beam to be observed is hanged vertically as it is shown on Fig. 2.7. An impedance head (B&K type 8001) and a mini-shaker (B&K model 4810) are glued onto the beam. The shaker is suspended by three elastic wires, and excites the beams with a swept signal on the 0-10 kHz range. A multipoint laser vibrometer (Polytec PSV-400) scans the entire extremity (surface 0.1 × 0.02 m, mesh grid 9 × 33 points) in order to acquire signals of displacement.

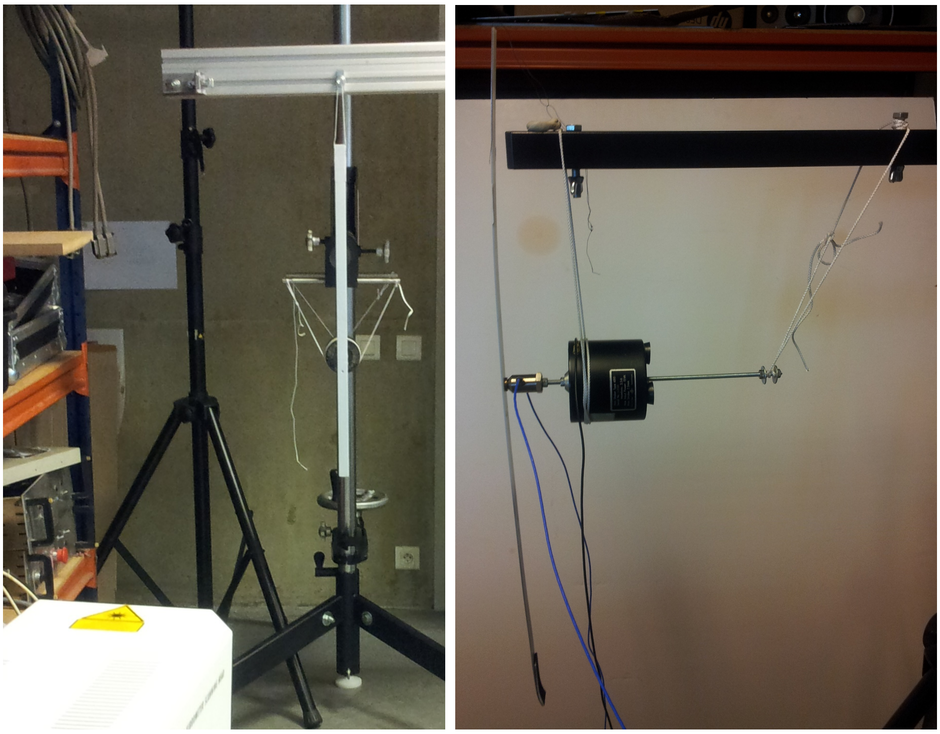
(a) (b)

Figure 2.7: Picture of the experimental setup: (a) front view and (b) side view.

2.3.1.2 Observations in the time domain

Displacement fields are plotted on Figs. 2.8, 2.9 and 2.10 for different beams and at different chosen frequencies. Each plot covers one period T of oscillation, divided in eight. For example, Fig. 2.8 shows the displacement of an extremity of uniform thickness. Nodes and anti-nodes of displacement can clearly be observed. The modes of such a very weakly damped structure are real and present nodes in their modal shapes, hence the nodes in their operational deflection shape.

The displacement field inside an ABH beam (see Fig. 2.9) do not present any nodes: a wave that propagates towards the extremity of the structure can be seen instead. This phenomenon is an indication of the complexity of the modes of the structure, that can be related to wave propagation phenomena as it is mentioned in [2]: when the reflection at

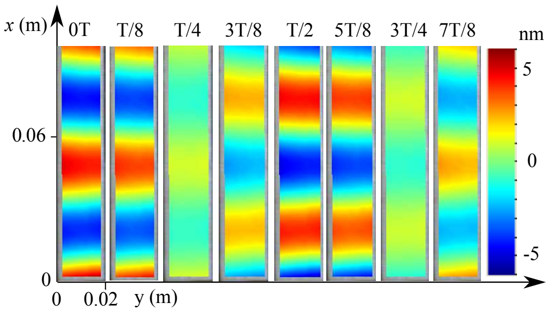

Figure 2.8: Displacement field of the free extremity of an uniform beam à 2330 Hz [45].

a boundary is partial, the superposition of incoming and outcoming waves does not lead to nodes of vibrations. Ref. [2] links wave propagation phenomena to energy propagation to a surrounding media or to a localised dissipation in the structure. The ABH effect consists indeed in a localised dissipation, but can also be viewed as a absorbing media in which energy propagates, therefore as an anechoic termination. This can be seen clearly on Figs. 2.9(a), (b) and (c) for three different frequencies.

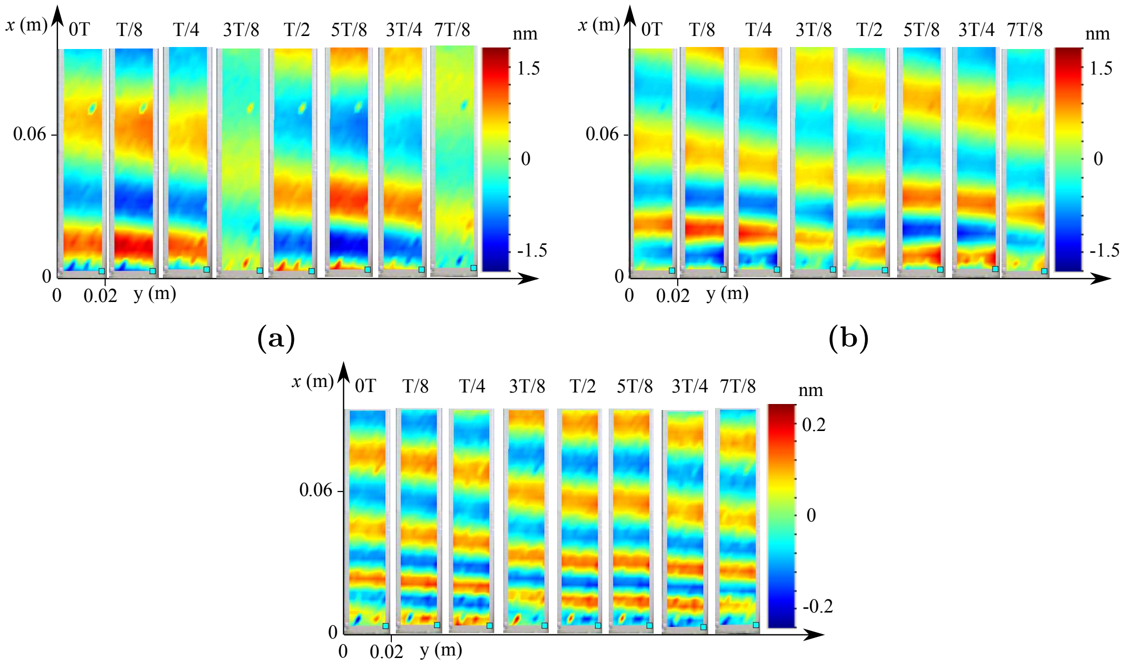

(a)

(b)

(c)

Figure 2.9: Displacement field of the covered ABH extremity at (a) 852 Hz (b) 2022 Hz and (c) 4001 Hz [45]. ABH profile extends from x=0 to x=0.06 m.

Depending on the frequency, the tip of the ABH profile can present a two-dimensional behaviour. It seems easier to observe this phenomenon of the uncovered tapered extremity (see Figs. 2.10(a) and (b)) but it can also be seen on the covered extremity. While the incident wave is plane when the thickness is important, this is not the case when the thickness is small (i.e. in this case, all the points of a cross section are in phase). In fact, it is immediate to see that the local wavelength is smaller that the thickness of the beam, so that the beam behaviour is not valid anymore. The plate hypothesis that is suggested by this observation is developed in subsequent chapters.

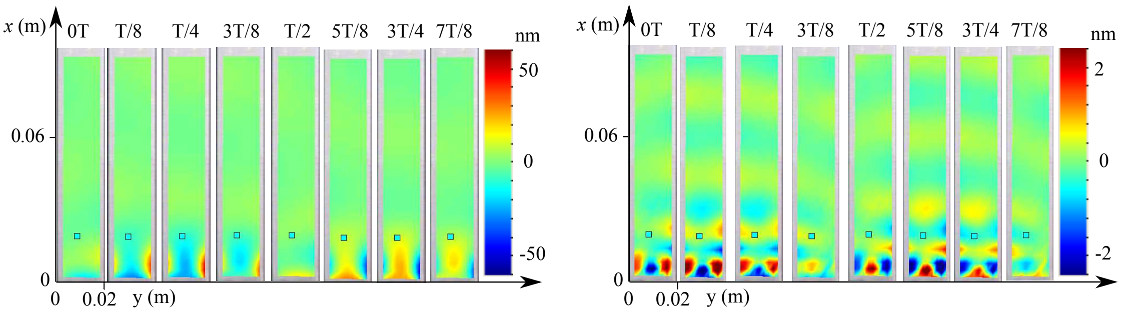

(a) (b)

Figure 2.10: Displacement field of the non covered ABH extremity at (a) 1297 Hz and (b) 3850 Hz [45]. ABH profile extends from x=0 to x=0.06 m.

2.3.2 Measurement of the reflection coefficient of an ABH termination

The reflection coefficient is a simple but meaningful indicator to characterise the ABH effect. The aim of this section presents an estimation method of the reflection coefficient of a beam extremity. The method is based on velocity measurements and shows that the added modal damping seen in Sec. 2.2 translates into a reduced reflection for the waves travelling towards the extremity.

2.3.2.1 Measurement method

Wave reflection and transmission in beams has been thoroughly studied [85, 90]. Several methods allow the estimation of reflection properties of beam extremities. Linjama *et al.* [86, 87] propose to measure the reflection of bending waves using a structural intensity technique. Vemula *et al.* [130] estimate the reflected energy of bending waves in a graded impedance interface using the half power bandwidth of the resonance peaks of the transfer function. Carniel *et al.* [22] and Piaud *et al.* [109] both propose expressions for the far field reflection coefficient in a beam. Moulet *et al.* [54, 98] use a Kundt tube-like technique in order to estimate the scattering properties of a junction between two beams from the measurements of velocities along the beam. This method is used in the current study.

2.3.2.1.1 Experimental setup

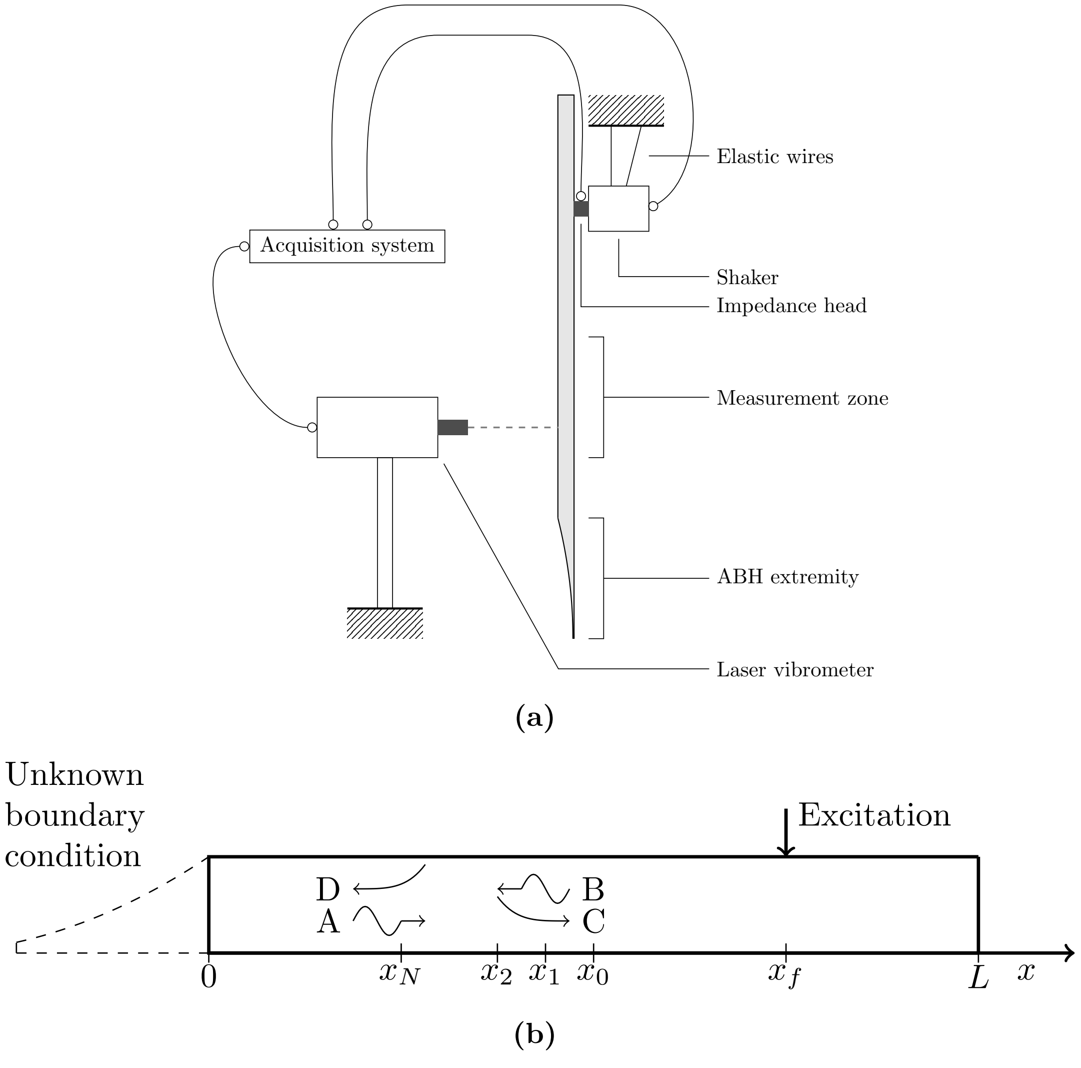

Figure 2.11: (a) Scheme of the experiment. (b) Scheme of the beam showing the excitation point at $x = x_f$, the $N + 1$ measurement points x_0 to x_N, the attenuating and propagating waves and the point x=0 at which the reflection coefficient is evaluated.

Setup

The estimation of the reflection coefficient is based on mobility transfer functions measurements. In order to avoid static deformation due to gravity, the beam to be tested is hanged vertically (see Fig. 2.11(a)); this point is found to be quite important. The extremity whose reflection coefficient is estimated is directed toward the bottom. An impedance head (B&K type 8001) and a shaker (B&K type 4810) are glued onto the beam. The shaker is suspended with three elastic wires. Velocities are measured using a laser vibrometer (Polytec OFV 303). The impedance head, shaker and vibrometer are linked to a LMS acquisition system (Scadas Mobile, 4 channels, Test.Lab Rev 13) which acquires force and acceleration signals at the excitation point and velocity signal at measurement points.

Measurement conditions

Transfer mobility measurements are performed at 21 abscissas 5 mm apart from each other. In the case of the aluminium ABH beam, the closest abscissa is distant of 0.1 m from the tapered region. Let A_0 be the point on the neutral axis of the beam at abscissa x_i (see Fig. 2.12(a)). Let A_l and A_r be two points at the right and left hand side of the neutral axis, with distances $a_l = A_l A_0$ and $a_r = A_r A_0$, respectively. Let E and $F(E)$ be the excitation point at abscissa x_f and the force applied in E, respectively. The measured velocity $\dot{W}_i$ at point A at a given abscissa x_i (A being A_0, A_r or A_l) can be written as

$$\dot{w}_i(A) = \dot{w}_{if}(A) + \dot{w}_{it}(A), \tag{2.7}$$

where $\dot{w}_{if}(A)$ and $\dot{w}_{it}(A)$ correspond to pure beam flexural motion and beam torsional motion, respectively. Only the flexural contribution should be estimated since the investigations on ABH only concern flexural motions.

Identification of the flexural contribution

The mobility on the neutral axis, where there is no torsional contribution, is defined as

$$Y(A_0, E) = \frac{\dot{w}_{if}(A_0)}{F(E)}. \tag{2.8}$$

Because of the symmetry and the antisymmetry of w_{if} and w_{it} with respect to the neutral axis, it can be shown that

$$Y(A_0, E) = \frac{a_l Y(A_l, E) + a_r Y(A_r, E)}{a_l + a_r} = \frac{\gamma Y(A_l, E) + Y(A_r, E)}{1 + \gamma}, \tag{2.9}$$

where $\gamma = a_l / a_r$. In practice, $Y(A_0, E)$ is not measured directly since it is not possible to guarantee that A_0 is on the neutral axis. The quantity $Y(A_0, E)$ is obtained in an indirect manner from measurements at points A_r and A_l. The γ coefficient is adjusted in order to minimize the amplitude of the first torsional resonance peak. This peak is identified in a preliminary step. In the present study, the frequency of this first torsional mode is 196.5 Hz. The torsional contribution $\dot{w}_{it}$ on the wave field is therefore efficiently separated from $\dot{w}_{if}$ on a wide frequency range, for each abscissa. Fig. 2.12(b) shows the mobility transfer function $\dot{w}_{if}/F(E)$ between excitation and a random measurement abscissa for the uniform aluminium beam at left and right hand sides of the centreline (full and dashed grey lines). The transfer function on the neutral axis (thick black line) is also plotted and shows that the first torsional peak vanishes. Mobilities of the uniform and ABH beams made of aluminium are plotted on Fig. 2.12(c); the torsional peaks are minimized and the smoothing effect of the ABH treatment is clearly observed.

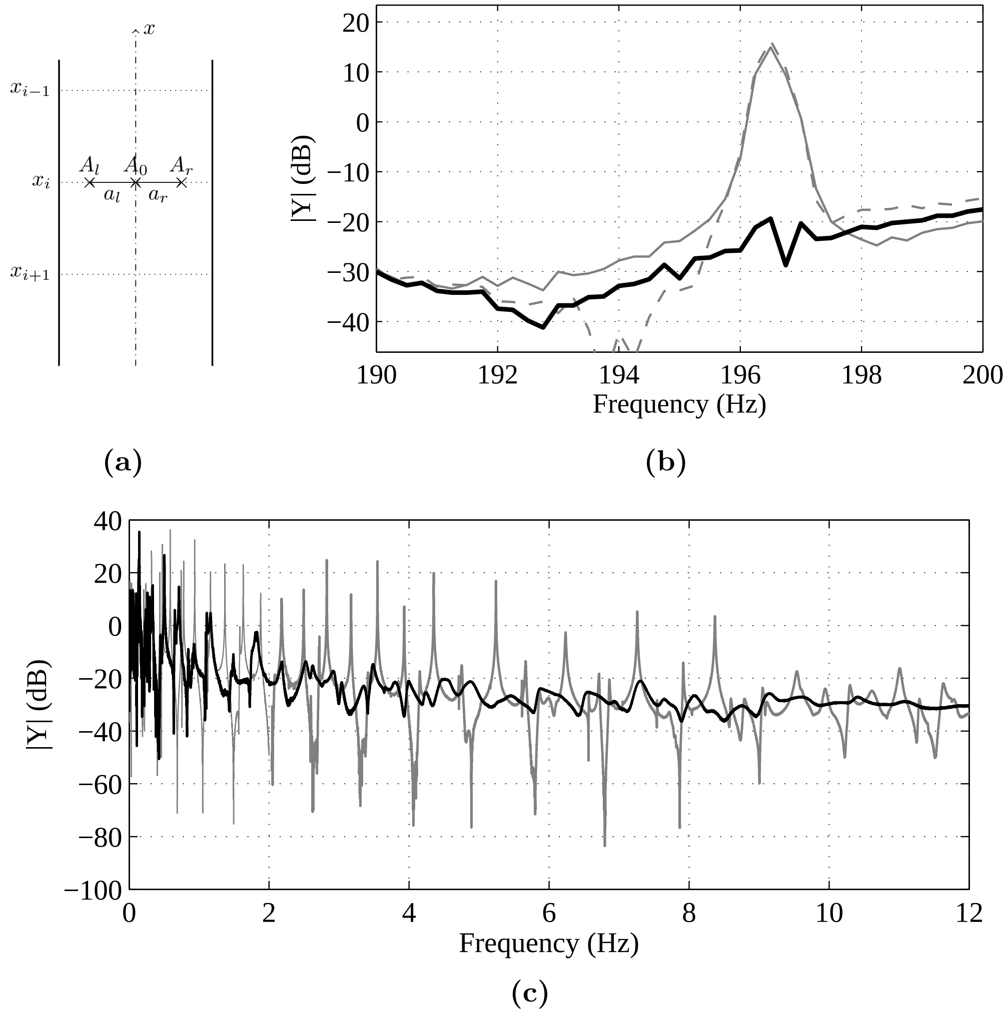

(a) (b)

(c)

Figure 2.12: (a) Left, neutral axis and right measurement points A_l, A_0 and A_r at abscissa x_i. (b) Transfer mobility measurement $Y(A_l, E)$ (full grey line) , $Y(A_r, E)$ (dashed grey line) and $Y(A_0, E)$ (thick full black line) on the uniform aluminium beam (dB, ref. 1 m.s^{-1}.N^{-1}). Force is applied at $x_f = 0.58$ m, velocity is measured at $x_i = 0.3$ m (see Fig. 2.11) (c) Transfer mobility measurement $Y(A_0, E)$ for uniform (grey line) and ABH (black line) beams made of aluminium (dB, ref. 1 m.s^{-1}.N^{-1}). Force is applied at $x_f = 0.58$ m, velocity is measured at $x_i = 0.3$ m.

Coherence function of the mobility measurements

The quality of the transfer function measurements is estimated using classical coherence function C between the excitation force F and the acquired velocity $\dot{w}$. It is defined as

$$C = \frac{|R_{\dot{w}F}|^2}{R_{\dot{w}} R_F}, \tag{2.10}$$

where $R_{\dot{w}F}$ is the cross spectral density between signals $\dot{w}(A_0)$ and $F(E)$, and $R_{\dot{w}}$ and R_F are the autospectral density of $\dot{w}(A_0)$ and $F(E)$, respectively. It is easily shown that excitation level has to be high enough to get coherence function close to 1. In practice, to ensure this issue on a wide frequency range, the whole useful band 0–12 kHz is split in two bands: 0–2 kHz and 2–12 kHz for which two different levels are applied for the swept sine excitation. Hence, for each couple (E, A_0), two sets of measurements are performed in order to get the complete mobility signal. Coherence functions for measurement made in these two ranges are shown on Fig. 2.13(a). Moreover, it is shown on Fig. 2.13(b) that in the ABH case, a particular attention has to be paid to the excitation level, and that an insufficient excitation level results in a coherence far from unity and leads to unreliable results on the reflection coefficient.

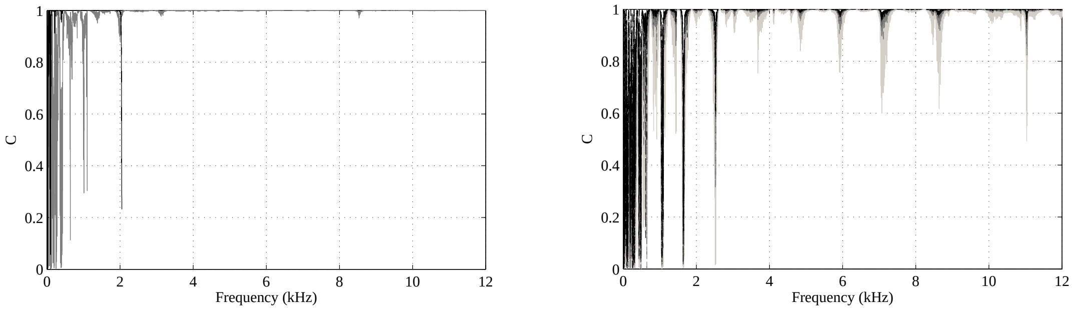

(a) **(b)**

Figure 2.13: Coherence functions (displacement/force) for aluminium ABH (a) on the 0–2 kHz (black) and 0–12 kHz (grey) ranges and (b) on the 0–12 kHz range with different excitation RMS levels corresponding to increased electrical tension applied to the shaker: 0.25 V, 0.5 V, 0.75 V and 1 V (from light grey to black, respectively). Force is applied at x_f=0.58 m and velocity is measured at x_i=0.3 m.

2.3.2.1.2 Methodology for the estimation of the reflection coefficient

Wave field solution for beams

Let us consider a beam of constant cross-section whose extremity x=0 bears an ABH profile seen as an unknown boundary condition (see Fig. 2.11(b)). Under the Euler-Bernoulli assumptions, the equation of harmonic flexural motion $w(x, \omega)$ of such a beam in the absence of excitation, assuming a harmonic motion with time dependence $e^{-j\omega t}$ is [90]

$$EI\frac{\partial^4 w(x,\omega)}{\partial x^4} - \rho S \omega^2 w(x,\omega) = 0 \qquad \forall x \in [0, L], \tag{2.11}$$

where ω is the angular frequency, E is the Young's modulus, I is the moment of inertia of the cross-section, ρ is the mass density, S is the area of the cross-section and L is the length of the uniform part of the beam.

The general solution for the displacement can be written as the sum of four waves [90]:

$$w(x,\omega) = A(\omega)e^{-jk_f x} + B(\omega)e^{+jk_f x} + C(\omega)e^{-k_f x} + D(\omega)e^{+k_f x} \qquad \forall x \in [0, L], \quad (2.12)$$

where the flexural wavenumber k_f is such that

$$k_f^4 = \frac{\rho S}{EI}\omega^2. \quad (2.13)$$

The scalar coefficients A, B, C and D represent the magnitude of backward and forward propagative and attenuating waves, respectively (see Fig. 2.11(b)).

At the ABH extremity (x=0), the boundary conditions associated to the equation of motion (2.11) can be written as a reflection matrix $\mathbf{R}$ such that

$$\begin{bmatrix} A \\ C \end{bmatrix} = \mathbf{R} \begin{bmatrix} B \\ D \end{bmatrix}, \quad (2.14)$$

where

$$\mathbf{R} = \begin{bmatrix} R_{pp} & R_{ap} \\ R_{pa} & R_{aa} \end{bmatrix}, \quad (2.15)$$

with R_{ij} the reflection coefficient between incident wave i and reflected wave j; i and j symbolize p and a standing for *propagating* and *attenuating* respectively. Note that the origin $x = 0$ is not placed at the end of the ABH beam but at its beginning. Point $x = 0$ is the point where the reflection matrix or coefficient is estimated.

We are interested in measuring terms of $\mathbf{R}$. The boundary condition at x=L has to be fixed for the experiment but do not play any role in the measurements of $\mathbf{R}$. In practice, free boundary conditions are supposed at x=L.

Far field assumption

Far from the excitation point and from the boundaries, attenuating waves vanish and the wave field can be well approximated as the sum of two propagating waves only

$$w(x,\omega) = A(\omega)e^{-jk_f x} + B(\omega)e^{+jk_f x}. \quad (2.16)$$

The boundary condition can then be described as far field reflection coefficient R that corresponds to R_{pp} in Eq. (2.15). It is arbitrarily assumed that the far field assumption is valid at a given frequency when the attenuating waves coming from an excitation point or a boundary condition lose 90 % of their amplitude. Then, there should be

$$\begin{cases} x_N > l \\ x_f - x_0 > l, \end{cases} \quad (2.17)$$

where the distance l satisfies [54]

$$\exp\left(-k_f l\right) = 0.1. \tag{2.18}$$

In the experiment described in Sec. 2.3.2.1.1, the closest measurement point is at l=0.1 m of the tapered zone of the aluminium ABH beam, so that the far field assumption is theoretically valid above 200 Hz (with parameters of Tab. 2.1).

Estimation of the wave and reflection coefficients

Let us consider $N+1$ points along the beam satisfying the far field assumption (see Fig. 2.11(b)). The displacement measured for all abscissas x_i ($i \in [0, N]$) can be related to the coefficients A and B through the matrix equation

$$\begin{bmatrix} w(x_0,\omega) \\ w(x_1,\omega) \\ w(x_2,\omega) \\ \dots \\ w(x_N,\omega) \end{bmatrix} = \underbrace{\begin{bmatrix} e^{-jk_f x_0} & e^{jk_f x_0} \\ e^{-jk_f x_1} & e^{jk_f x_1} \\ e^{-jk_f x_2} & e^{jk_f x_2} \\ \dots & \dots \\ e^{-jk_f x_N} & e^{jk_f x_N} \end{bmatrix}}_{\mathbf{M}} \begin{bmatrix} A(\omega) \\ B(\omega) \end{bmatrix}, \tag{2.19}$$

with $\mathbf{M}$ a $(N \times 2)$ matrix. A least-squares estimation of the $[A, B]^T$ vector can be effectively obtained with

$$\begin{bmatrix} A(\omega) \\ B(\omega) \end{bmatrix} = \mathbf{M}^\dagger \begin{bmatrix} w(x_0,\omega) \\ w(x_1,\omega) \\ w(x_2,\omega) \\ \dots \\ w(x_N,\omega) \end{bmatrix}, \tag{2.20}$$

where $\mathbf{M}^\dagger = (\mathbf{M}^*\mathbf{M})^{-1}\mathbf{M}^*$ is the Moore-Penrose generalized inverse [108] of $\mathbf{M}$ and $\mathbf{M}^*$ is the conjugate transpose of $\mathbf{M}$.

From this estimation of the wave coefficients, the far field reflection coefficient of the extremity can be derived:

$$R(\omega) = \frac{A(\omega)}{B(\omega)}. \tag{2.21}$$

Consistency of the estimation method

The estimation method of R uses measurements at 21 abscissas in order eliminate noise. It is verified that the results do not depend on the abscissas or the number of measurement points. Fig. 2.14 shows the same estimation done with measurements 1 to 21, 1 to 10 and 11 to 21, in the case of the covered ABH beam made of aluminium. The results superimpose and are a good illustration of the consistency of the estimation method: it can be considered that complex variations of $|R|$ are not due to noise but to physical deterministic phenomena.

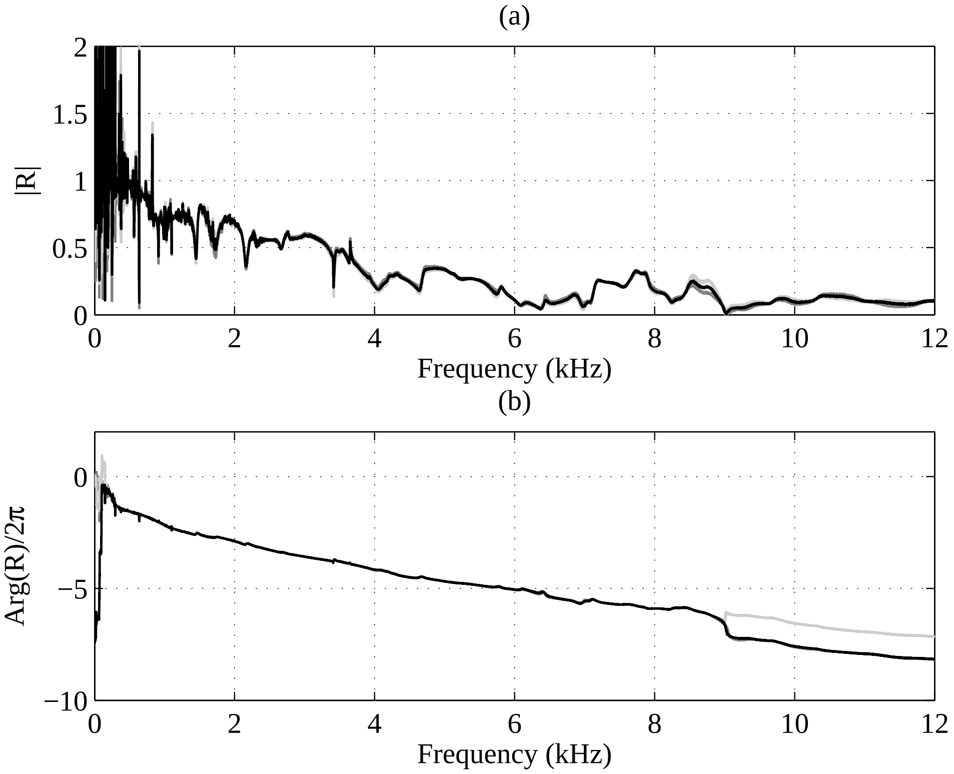

Figure 2.14: Reflection coefficient in (a) modulus and (b) phase estimated with measures 1 to 21 (black), 1 to 10 (dark grey) and 11 to 21 (light grey).

2.3.2.2 Measurement of the reflection coefficient

2.3.2.2.1 Validation on the uniform beam

It can be shown that the reflection coefficient for a free end is given by (see [90] for a demonstration of this result)

$$R = \frac{A}{B} = -\mathrm{j}. \tag{2.22}$$

This result is used to validate the proposed measurement method. Fig. 2.15 presents the reflection coefficient of the free end measured on aluminium (full black line), estimated with the method described in Sec. 2.3.2.1. It is checked that the theoretical result is experimentally obtained: modulus and phase are constant with respect to frequency and equal to 1 and $-\frac{\pi}{2}$, respectively. It is remarkable to see that the experimental result of Fig. 2.15 is conform to the theoretical result of Eq. (2.22) on a wide frequency range. Coherences of the measurements are close to 1 until 12 kHz and make this estimation reliable. This verification of the theoretical result assesses the measurement method.

Fig. 2.15 also shows the reflection of the free end in the polymer case with the assumed material characteristics of Tab. 2.1 (full light grey line). The unexpected phase increase suggests an incorrect knowledge of the wavenumber. Indeed, modulus and phase of the reflection coefficient are related to the imaginary and real parts of the wavenumber, respectively. The wavenumber has then to be carefully corrected in order to fit the measured reflection coefficient with the free end theoretical result, in modulus and phase. The fit made on the characteristics of the polymer material consists in increasing by 2 % the real part of the wavenumber calculated with characteristics of Tab. 2.1, in order to obtain the theoretical reflection coefficient of a free end (E_1=3.8 GPa). Modulus and phase of R with fitted wavenumber (see Fig. 2.15, dashed dark grey line) are constant and show that the estimation method relies on a precise knowledge of the wavenumber.

However, it can be noticed that the reflection coefficient for the polymer beam behaves poorly after 7 kHz. This can be expected since the structure cannot be considered anymore as a beam above this frequency and is likely to display a two-dimensional plate behaviour, because the wavelength neighbours the width of the cross-section, that is:

$$\lambda_{f=7\mathrm{kHz}}^{\mathrm{Polymer}} \simeq 1.3b. \tag{2.23}$$

Consequently, the estimation based on one-dimensional wave decomposition does not make sense above 7 kHz for the polymer beams. This issue does not appear with the aluminium structures in which the assumption of undeformed cross-section remains valid until 16 kHz.

Small singularities appear on the curves, especially for the aluminium beam. This is due to a drop of coherence at anti-resonances. A more damped structure such as the polymer beam shows less coherence drops and thus, a smoother curve for the reflection coefficient.

2.3.2.2.2 Results on ABH beams

Fig. 2.16 shows the estimated reflection coefficient for the ABH extremity in modulus

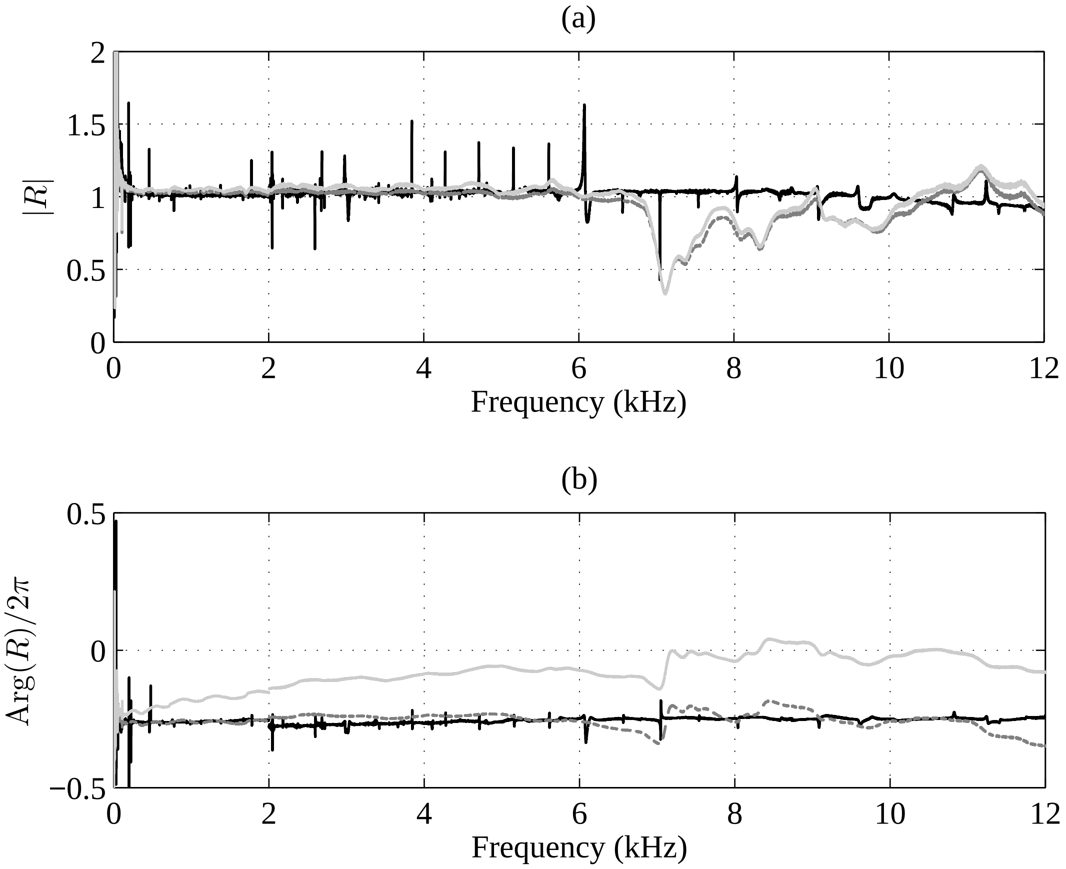

Figure 2.15: Estimated reflection coefficient R for the free end of uniform beams made of aluminium (full black line), polymer with fitted wavenumber (dashed dark grey line) and polymer with non-fitter wavenumber (full light grey line), in (a) modulus and (b) phase.

and phase, in aluminium (full black line) and polymer (dashed dark grey line) beams. Compared to the free end, it is very clear that the modulus of R diminishes with increased frequency. Values in modulus can be as low as 0.1. Moreover, oscillations can be observed on the modulus. The phase of the reflection coefficient displays a significant additional roll down with frequency.

Qualitative variations of $|R|$ are similar for the aluminium and polymer cases. The modulus of the reflection coefficient is lower for the polymer beam, showing that the ABH is more efficient. The phase also rolls down quicker in the polymer case below 7 kHz.

To the authors's knowledge, such reflection coefficient measurements are the first ones performed on ABH beams.

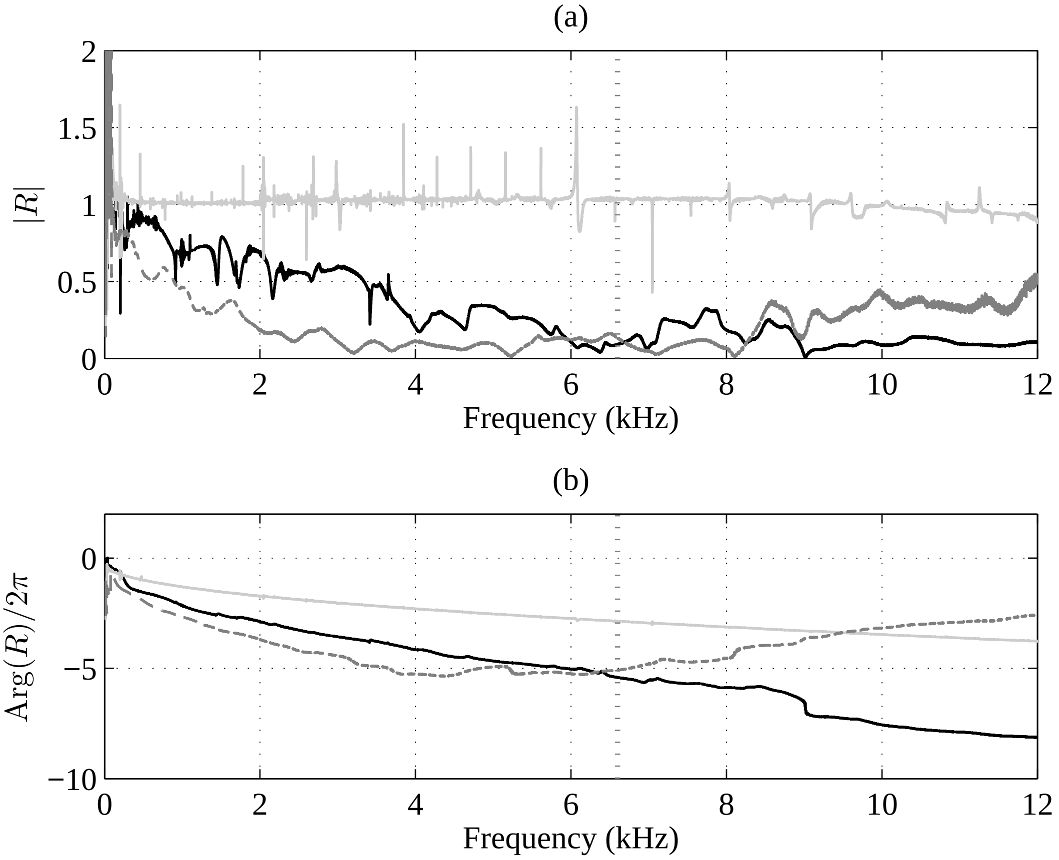

Figure 2.16: Estimated reflection coefficient R for the termination of the aluminium (full black line) and polymer (dashed grey line) ABH beams and reflection coefficient for the reference beam at l_{ABH} of the free end (full light grey line), in (a) modulus and (b) phase. Frequency limit for beam behaviour of polymer beam is indicated (vertical gray dotted line).

2.4 Linearity of the ABH beam

The decrease of thickness has a consequence on the vibration amplitude. From Sec. 2.3.1, it is clear that the amplitude of displacement is larger in the tapered region on the non covered ABH beam; it is less clear on the covered ABH. Large amplitudes generate geometrical non-linearities that influence the damping properties.

Using the experimental setup described in Sec. 2.3.2.1.1, measurements of transfer function are made on an ABH beam with a thin damping layer (desk tape), using the same swept-sine excitation with different RMS level: 0.25 V, 0.5 V, 0.75 V and 1 V. Fig. 2.17 displays no differences between the transfer functions at different excitation levels. The only actual difference is the noisiness of the curves as the lower is the excitation, the noisier is the curve; this translates in a poor coherence function. Resonances and damping properties are identical. This observation shows that the structure responds linearly and suggests that non linear phenomena are unlikely to participate in the damping that is observed, despite the high displacement amplitudes of the tapered extremity.

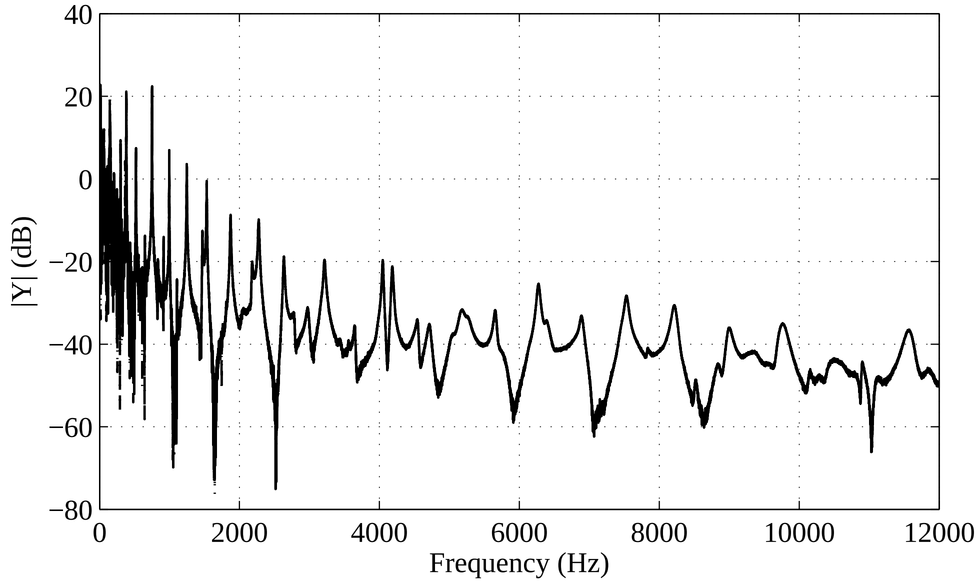

Figure 2.17: Mobility transfer function of an ABH beam at a random point for different with different excitation RMS levels corresponding to increased electrical tension applied to the shaker: 0.25 V (full), 0.5 V (dashed), 0.75 V (dotted) and 1 V (dashdotted).

2.5 Conclusions

This chapter presents experimental observations and analyses of beams with an ABH termination. The following conclusions can be drawn:

- Two manufacturing techniques can be used to obtain the required thin and precise beam profiles (conventional high speed machining and prototyping). These techniques are used for getting aluminium and polymer ABH beams. Thicknesses at the end are 16 μm for the polymer beams and between 10 and 20 μm for the aluminium ones.

- Using a high resolution technique, a modal analysis is performed and permit to quantify the change in the modal loss factor and in the modal overlap of the beam. For the aluminium beam, the modal loss factors are multiplied by 10 to 20 when introducing the ABH . For the polymer, they are multiplied by 2.

  the change in the modal damping induced by the ABH termination is measured. It provides an increase of the modal overlap factor of the beam. Note that the loss factors of the reference polymer beam are indeed higher than those of the aluminium one, so that the relative change in damping between is lower compared to the uniform structure.

- Velocity measurement inside the ABH using a laser vibrometer confirm that the wavelength decreases in the tapered extremity and allow to see wave propagation phenomena: progressive waves near the ABH termination are observed instead of stationary waves near usual terminations.

- A Kundt-like method for estimating the reflection coefficient of a beam extremity is presented and applied to the ABH beams. The measurement method is validated by comparisons with the known analytical result for a free end, for the two different materials. It is clearly seen that the reflection coefficient of the ABH termination decreases with frequency, with oscillations. The phase of the reflection coefficient rolls down, indicating a relatively important travel time of the waves in the tapered extremity.

- Finally, measurements at different excitation levels reveal that the structure responds linearly, suggesting that no non-linear effects participate in the damping provided by the ABH effect.

Chapter 3

Role of the spatial variations of the complex bending stiffness of the ABH beam

The modal parameters of the ABH beams have been studied experimentally in Sec. 2.2. It has been shown that the ABH termination corresponds to an increase in modal loss factor and modal overlap factor. It is proposed here to give better understanding of the experimental results and to explain how the heterogeneity of both rigidity and damping is responsible for this increase. For this matter, a model of flexural vibrations in a non uniform thin plate is proposed in Sec. 3.1. A plate model is considered instead of a beam one because the expected flexural wavelength at the end of the ABH extremity reaches down the width of the cross-section in the frequency band studied. In Sec. 3.2, an observation of two-dimensional modes in the tapered region of the beam justifies this assumption. Additionally, the effect of the geometrical and material heterogeneity on the modal density of the structure is studied.

3.1 Observation using a numerical model

3.1.1 Governing equations

The equation of the free transverse vibration $w(x, y)$ of the structure in the case of an harmonic motion is given by Ref. [84]:

$$\nabla^2(D(x)\nabla^2 w(x,y)) - (1-\nu)\Big(\frac{\partial^2 D(x)}{\partial x^2}\frac{\partial^2 w(x,y)}{\partial y^2}\Big) - \rho(x)h(x)\omega^2 w(x,y) = 0, \qquad (3.1)$$

where $\rho(x)$ is the mass density, $h(x)$ is the thickness, ω is the angular frequency, $D(x)$ is the local complex bending stiffness and ν the Poisson's ratio. Coordinates x and y are defined in Fig. 3.1. In Eq. (3.1), the bending stiffness, thickness and mass density are characteristics of the sandwich structure composed by the association of the aluminium beam and the damping layer.

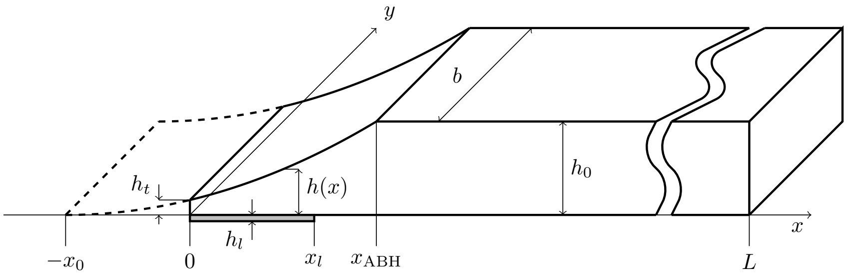

Figure 3.1: Scheme of an ABH profile at a beam extremity. Note the change in notation compared to Fig. 2.1(a): $x_{\text{ABH}} = l_{\text{ABH}}$, $x_{\text{ABH}} + x_0 = l_t$ and x_l=l_l.

The model uses structural damping, represented with a loss factor included in the imaginary part of the complex bending stiffness $D(x)$ in Eq. (3.1). The effect of the layer is represented with equivalent mechanical properties that modify the bending stiffness, the mass density and the thickness, following the model of Ross-Ungar-Kerwin [116] as used in the current context by Georgiev [57]. The complex bending stiffness is thus given by

$$D(x) = \begin{cases} D_p(x) = \dfrac{E_p h_p(x)^3}{12(1-\nu^2)}(1+\mathrm{j}\eta_p), & \forall x > x_l \\ D_p(x)\Bigg[(1+\mathrm{j}\eta_p) + \frac{E_l}{E_p}\left(\dfrac{h_l}{h_p(x)}\right)^3(1+\mathrm{j}\eta_l) & \\ +\dfrac{3\left(1+\frac{h_l}{h_p(x)}\right)^2 + \frac{E_l h_l}{E_p h_p(x)}(1-\eta_p\eta_l+\mathrm{j}(\eta_p+\eta_l))}{1+\frac{E_l h_l}{E_p h_p(x)}(1+\mathrm{j}\eta_l)}\Bigg], & \forall x \leq x_l, \end{cases} \tag{3.2}$$

where $D_p(x)$, E_p, η_p and $h_p(x)$ are the bending stiffness, the Young's modulus, the loss factor and the thickness of the plate alone, respectively , E_l, η_l and h_l are the Young's modulus, the loss factor and the thickness of the damping layer, respectively. One must also take into account the effect of the mass of the layer and its thickness using an equivalent mass density $\rho(x)$:

$$\rho(x) = \begin{cases} \rho_p, & \forall x > x_l \\ \dfrac{\rho_p h_p(x) + \rho_l h_l}{h_p(x) + h_l}, & \forall x \leq x_l, \end{cases} \tag{3.3}$$

where ρ_p and ρ_l are the mass densities of the structure and the layer, respectively, and a total thickness $h(x)$ of the sandwich plate:

$$h(x) = \begin{cases} h_p(x), & \forall x > x_l \\ h_p(x) + h_l, & \forall x \leq x_l, \end{cases} \tag{3.4}$$

where the thickness of the plate is, in the ABH case,

$$h_p(x) = \begin{cases} h_0, & \forall x > x_{\text{ABH}} \\ h_0 \dfrac{(x+x_0)^m}{(x_0+x_{\text{ABH}})^m}, & \forall x \leq x_{\text{ABH}}. \end{cases} \tag{3.5}$$

The truncation thickness h_t (see Fig. 3.1) is the thickness at the very tip of the ABH profile ($x = 0$).

Free boundary conditions are considered at the ABH extremity ($x = 0$), the other beam extremity ($x = L$) and on lateral edges ($y = 0$ and $y = b$). The so-called Kelvin-Kirchhoff edge reaction and the bending moment are zero at the edges and can be derived to obtain, respectively,

$$V_x = -\frac{\partial}{\partial x}(D(\frac{\partial^2 w}{\partial x^2} + \nu \frac{\partial^2 w}{\partial y^2})) - 2D(1-\nu)\frac{\partial^3 w}{\partial x \partial y^2} = 0 \qquad \text{for } x = 0, L \quad \forall y, \tag{3.6}$$

$$M_x = -D\Big(\frac{\partial^2 w}{\partial x^2} + \nu \frac{\partial^2 w}{\partial y^2}\Big) = 0 \qquad \text{for } x = 0, L \quad \forall y, \tag{3.7}$$

along the y-direction, and

$$V_y = -D\frac{\partial}{\partial y}(\frac{\partial^2 w}{\partial y^2} + \nu \frac{\partial^2 w}{\partial x^2})) - 2(1-\nu)\frac{\partial}{\partial x}(D\frac{\partial^2 w}{\partial x \partial y}) = 0 \qquad \text{for } y = 0, b \quad \forall x, \tag{3.8}$$

$$M_y = -D\Big(\frac{\partial^2 w}{\partial y^2} + \nu \frac{\partial^2 w}{\partial x^2}\Big) = 0 \qquad \text{for } y = 0, b \quad \forall x, \tag{3.9}$$

along the x-direction. Free boundary conditions also require [84] that

$$M_{xy} = -D(1-\nu)\frac{\partial^2 w}{\partial x \partial y} = 0 \qquad \text{at points } (0,0), (0,b), (L,0) \text{ and } (L,b). \tag{3.10}$$

The equation of motion and the boundary conditions lead to an eigenvalue problem, that will be presented and solved according to the numerical method described in Sec. 3.1.2.

A discussion on the validity of the model is relevant at this point. It is emphasized that the dispersion relation is such that at a given frequency, if the wavelength is greater than the thickness in the uniform part of the plate, it is also the case in the tapered zone. Indeed, it is straightforward that at a given frequency, the ratio of wavelength over thickness

$$\frac{\lambda}{h} = \frac{2\pi\sqrt[4]{Eh^2/12\rho(1-\nu^2)\omega^2}}{h}, \tag{3.11}$$

diminishes with the thickness. Therefore, since the classical theory of plate based on the Kirchhoff model is valid in the region of uniform thickness (i.e. the wavelength is much larger than the thickness), it also applies in the tapered zone and shear and rotary inertia are expected to be negligible. One is also reminded that the model does not take into account some characteristics of the practical realisation of the ABH effect: the lack of symmetry and added damping may move the neutral plane of the structure and generate plane extension behaviour that is coupled with flexural behaviour. According to the literature [75, 57, 93], flexural behaviour seems sufficient to produce the ABH effect and may therefore be the dominant mechanism. Other effects are thus neglected in this paper but may be investigated in a further study. Note that the curvature of the neutral plane could nevertheless be addressed using a shell theory, such as the one presented in [125]. The formulation allows to see a shallow shell as a deformed or imperfect configuration of a thin plate and uses an Airy stress function and a Monge-Ampère bilinear operator that easily allows to consider also geometrical non linearities due to large displacements, using the Von Karman model [20, 6].

Note that the coupling between the beam and the air (acoustic radiation) can be an additional source of damping [80], that is not taken into account in this model. Using the tools presented in Chap. 2, it is possible to evaluate the importance of this coupling by estimating the reflection coefficient and modal parameters of the experimental ABH beams in the absence of air. This would be feasible using a vacuum chamber. Such a chamber is now available in the laboratory but has not been used during this PhD.

3.1.2 Numerical scheme

The problem described in Sec. 3.1.1 is numerically solved by using a second-order finite difference scheme [27, 14, 7]. The spatial derivative operators in Eq. (3.1) and Eqs. (3.6)–(3.10) can be approximated from Taylor series. To introduce the needed notations, a discrete approximation by backward finite difference of the first derivative of the function $w(x)$ is given as an example:

$$\frac{\mathrm{d}w(x)}{\mathrm{d}x} \approx \frac{1}{\Delta_x}(w_n - w_{n-1}) = \delta_{x-} w_n, \tag{3.12}$$

where $w_n = w(x)$, $x = n\Delta_x$ with Δ_x the spatial step and n the spatial index, and δ_{x-} is the backward differential operator. The double derivative is approximated by the operator δ_{xx} defined as

$$\frac{\mathrm{d}^2 w(x)}{\mathrm{d}x^2} \approx \delta_{xx} w_n = \frac{w_{n+1} - 2w_n + w_{n-1}}{\Delta_x^2}. \tag{3.13}$$

A backward spatial averaging operator μ_{x-} defined such that $\mu_{x-} w_n = (w_n + w_{n-1})/2$, is also applied for the numerical scheme suitability.

In classical cases for which the thickness of the plate is constant, such a second-order finite difference scheme is straightforward. The present case is more difficult since the thickness is locally reduced, leading to an important numerical dispersion or an important computation cost. Indeed, the wavelength in the ABH structure dramatically decreases along the ABH profile, since it depends on the local thickness for a given frequency. To correctly represent very small wavelengths and to avoid numerical dispersion, a non uniform mesh grid is proposed. A practical implementation consists in using a coordinate change that switches a non-uniform "physical" mesh grid into a transformed uniform mesh grid where a transformed equation of motion is solved [14]. The interest is to avoid a tedious resolution on a non-uniform grid. Variable x defines the physical coordinate and variable $\tilde{x}$ defines the transformed coordinate. Variable $\lambda = 2\pi\sqrt[4]{Eh^2/12\rho(1-\nu^2)\omega^2}$ represents the wavelength in the physical space whereas variable $\tilde{\lambda}$ is the wavelength in the transformed space. The coordinate change may be chosen in order to match the change in wavelength so that

$$\frac{\lambda(x)}{\mathrm{d}x} = \frac{\tilde{\lambda}}{\mathrm{d}\tilde{x}}, \tag{3.14}$$

remains constant. Since λ varies with the square root of the thickness according to classical plate theory [84], the coordinate change is chosen as follows:

$$\mathrm{d}\tilde{x} = \frac{\mathrm{d}x}{\tilde{x}_{\mathrm{av}}\sqrt{h(x)}} \qquad \text{with} \qquad \tilde{x}_{\mathrm{av}} = \int_0^L \frac{1}{\sqrt{h(x)}}\mathrm{d}x, \tag{3.15}$$

where L is the dimension of the plate along the x-direction. $\tilde{x}_{av}$ permits the coordinate $\tilde{x}$ to be adimensional. It is verified that the wavelength $\tilde{\lambda}$ is constant in this case:

$$\tilde{\lambda} = \frac{\mathrm{d}\tilde{x}}{\mathrm{d}x}\lambda(x) = \frac{2\pi\sqrt[4]{E/12\rho(1-\nu^2)\omega^2}}{\tilde{x}_{av}}\frac{\sqrt{h(x)}}{\sqrt{h(x)}}. \tag{3.16}$$

Figs. 3.2(a) and (b) illustrate this transformation: the spatial step on the physical grid decreases with x according to the thickness profile, while the spatial step on the resolution grid is constant. Note that no coordinate change is applied to the y coordinate.

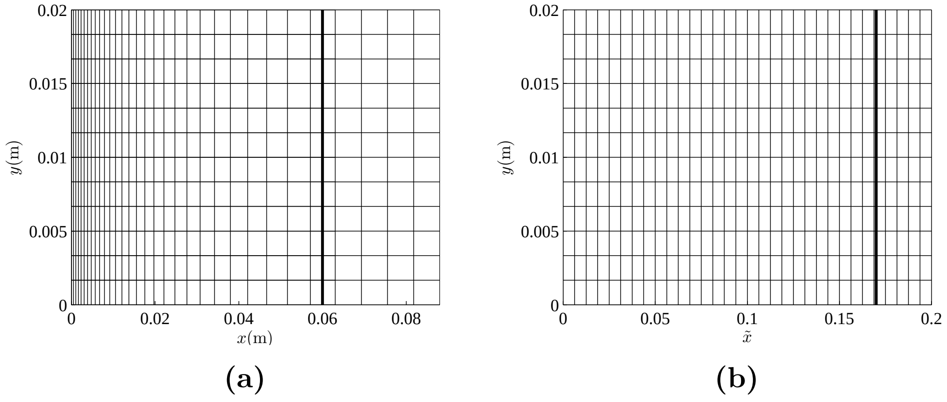

(a) **(b)**

Figure 3.2: (a) Physical grid, non-uniform in x and (b) resolution grid, uniform in $\tilde{x}$. The thick line indicates x_{ABH}.

The equation to solve on the transformed grid, derived from Eq. (3.1), is finally the following:

$$\begin{aligned}\frac{h_n^{-1/2}}{\tilde{x}_{\mathrm{av}}^2}\delta_{\tilde{x}+}\Big[(\mu_{\tilde{x}-}h_n^{-1/2})\delta_{\tilde{x}-}\Big[D_n\Big(\frac{h_n^{-1/2}}{\tilde{x}_{\mathrm{av}}^2}\delta_{\tilde{x}+}((\mu_{\tilde{x}-}h_n^{-1/2})\delta_{\tilde{x}-}w_{n,q}) + \delta_{yy}w_{n,q}\Big)\Big]\Big] \\ + D_n\delta_{yy}\Big[\frac{h_n^{-1/2}}{\tilde{x}_{\mathrm{av}}^2}\delta_{\tilde{x}+}((\mu_{\tilde{x}-}h_n^{-1/2})\delta_{\tilde{x}-}w_{n,q}) + \delta_{yy}w_{n,q}\Big] \\ - (1-\nu)\Big(\frac{h_n^{-1/2}}{\tilde{x}_{\mathrm{av}}^2}\delta_{\tilde{x}+}((\mu_{\tilde{x}-}h_n^{-1/2})\delta_{\tilde{x}-}D_n)\delta_{yy}w_{n,q}\Big) - \rho h_n\omega^2 w_{n,q} = 0. \quad (3.17)\end{aligned}$$

where n and q are the spatial indexes of the grid related to $\tilde{x}$ and y respectively, $\delta_{\tilde{x}-}$ and $\delta_{\tilde{x}+}$ are respectively the backward and forward finite difference operators, $\mu_{\tilde{x}-}$ and $\mu_{\tilde{x}+}$ are respectively the backward and forward averaging operators and δ_{yy} is the approximation to the second derivative in y [14]. The transformed boundary conditions are also derived from finite difference operators [14] but they are shown in Appendix A.3 for the sake of conciseness.

The eigenproblem formulated by Eq. (3.17) can be written under matrix formulation:

$$(\mathbf{K} - \alpha^2\mathbf{M})\boldsymbol{\phi} = 0, \quad (3.18)$$

where $\mathbf{K}$ and $\mathbf{M}$ are respectively the complex stiffness matrix and the mass matrix of the structure, α is an eigenvalue and $\boldsymbol{\phi}$ is an eigenvector. A validation of the approach against FEM solution (commercial Comsol software) can be found in Appendix A.3.

3.1.3 Results

Results obtained on simulated beams made of aluminium, whose dimensions are those appearing in Tab. 3.1, are presented in this section. The finite difference model uses a 640×240 grid ($\Delta_{\tilde{x}} = 1.6 \times 10^{-3}$, $\Delta_y = 4.2 \times 10^{-4}$ m).

Parameters of the beam						
E_p [GPa]	ρ_p [kg m^{-3}]	ν	η_p [%]	h_0 [mm]	L [m]	b [mm]
69.8	2700	0.3	0.2	1.5	0.895	20
Parameters of the ABH						
x_0 [mm]	x_{ABH} [mm]	h_t [µm]	m			
5.3	6	10	2			
Parameters of the damping layer						
E_l [GPa]	ρ_l [kg m^{-3}]	η_l [%]	l_l [m]	h_l [µm]		
7	1000	40	0.05	100		

Table 3.1: Values of the parameters for used the numerical model.

3.1.3.1 Typical results

According to the literature (see [59] for example), the eigenvalues α_k of the problem defined in Eq. (3.18) can be written:

$$\alpha_k = -\omega_k \left(\xi_k - \mathrm{j}\sqrt{1-\xi_k^2} \right), \tag{3.19}$$

which allows us to define ω_k, the natural frequencies and ξ_k, the modal damping ratios (with $\eta_k = 2\xi_k$ the modal loss factors).

Fig. 3.3(a) displays the thickness profile of the reference beam ($\triangle$) and the ABH beam ($\triangledown$). The eigenvalues for these two cases are plotted in the complex plane on Fig. 3.3(b). For any mode k with eigenvalue α_k of coordinates $(-\mathrm{Re}(\alpha_k), \mathrm{Im}(\alpha_k))$ on Fig. 3.3(b), the modal loss factor of this mode is related to the angle between the imaginary axis and the direction $\big((0,0), (-\mathrm{Re}(\alpha_k), \mathrm{Im}(\alpha_k))\big)$ so that an increase of this angle is simply an increase of the modal loss factor.

It is shown that most of the eigenvalues of the ABH are located along a straight line in the complex plane. The associated modes have then a loss factor that is roughly close to a constant value and that is higher than that of the reference: ABH effect leads to an increase of the modal loss factor for the majority of the modes. This is the case of modes 14 and 42 indicated on Fig. 3.3(b), as examples. This phenomenon can be more clearly viewed on Fig. 3.4 where are plotted the modal loss factors for the two cases in the frequency range 0–4000 Hz. On this figure, small variations around 2 % can be observed in the ABH case.

Some eigenvalues of ABH do not belong to the same line and have a higher real part. The associated modes have then a greater loss factor. Examples of modes 23 and 41 are indicated on Fig. 3.3(b). They can conveniently be called "hyper-damped" modes.

3.1.3.2 Consequence of the non-uniformity of the damping loss factor

The inhomogeneity of the mechanical properties all over the domain has some consequences on the eigenfrequencies and the eigenmodes of the structure. In a conservative case, $D_p(x)$ is real. The problem has purely imaginary eigenvalues α_k and purely real eigenmodes ϕ_k. In a dissipative case where the dissipation is homogeneous, the bending stiffness can be written $D_p(x) = E_p h_p^3(x)/12(1-\nu^2) \times (1+\mathrm{j}\eta_p)$ where η_p is constant, and $(1+\mathrm{j}\eta_p)$ can get out of the spatial operator in Eq. (3.1); the eigenmodes are real and are the same than in the conservative case; the eigenvalues however are multiplied by a complex number depending on the material loss factor only [59]. This implies that the loss factor of a uniform structure and a non-uniform structure are the same if they are equally and homogeneously damped, even if their natural frequencies are different. In a dissipative case where the dissipation is non homogeneous over the space, both eigenvalues and modes are complex and different from the conservative or dissipative with homogeneous dissipation cases. This means that the increase of loss factor seen on Fig. 3.3(b) and

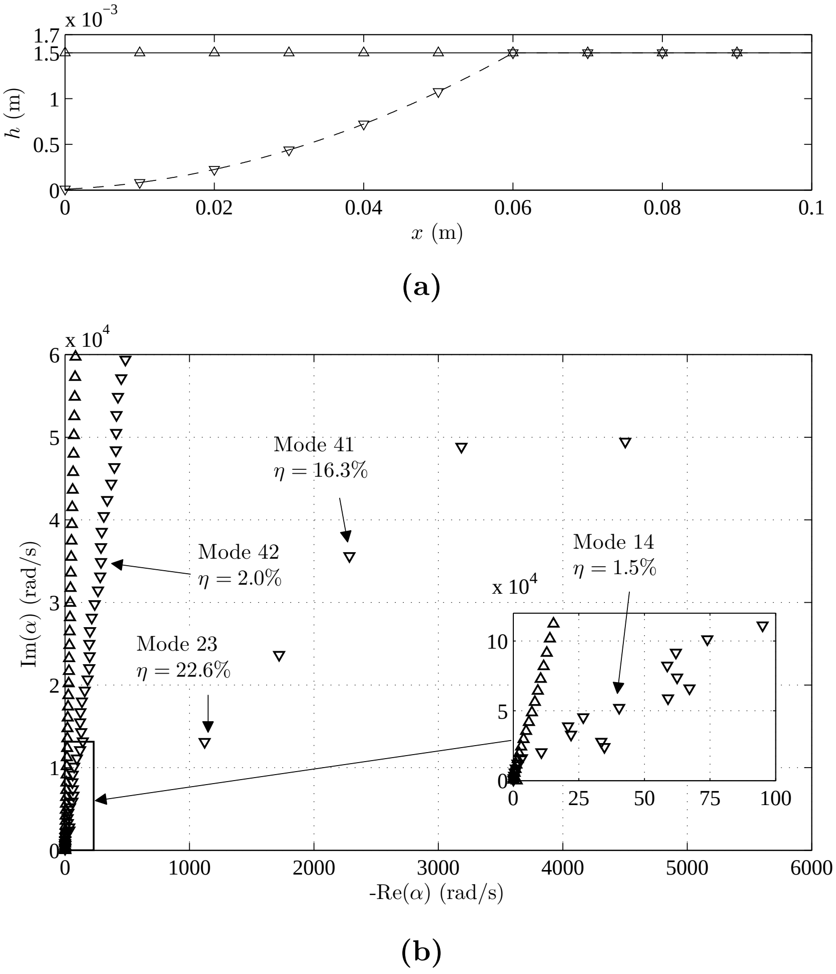

Figure 3.3: (a) Thickness profile and (b) spectrum of the complex eigenvalues of Reference (△) and ABH (h_t=10 µm) (▽) beams (published in [38]).

Fig. 3.4 comes from the spatial repartition of the losses. It puts the light on the role of the damping layer: without it, the damping properties are homogeneous and the loss factors are the same than in the reference case.

3.1.3.3 Frequency limit for ABH efficiency

Fig. 3.4 shows the modal loss factors on the frequency range 0–4000 Hz and allows to see an efficiency threshold in frequency for the ABH: in the simulated case, below 200 Hz modal loss factors of the ABH beam and the reference beam have the same order of magnitude. From 250 Hz, the loss factors of the ABH beam suddenly increase to reach a value of about 2% in the rest of the frequency range, with local peak values for the hyper-damped modes (see dashed line on Fig. 3.4). In this case, the length x_{ABH} of the tapered profile correspond to one quarter of the wavelength in the uniform region at 250 Hz. This observation can give a rule of thumb to size the ABH profile:

$$l_{\mathrm{ABH}} \simeq \lambda/4. \tag{3.20}$$

Previous works [75, 57] do not explicitly mention this limit, although the point was made that the covered tapered profile was not playing any role at low frequency. The observation of Fig. 3.4 confirms what is observed in Sec. 2.2 about the attenuation being noticeable above a starting frequency.

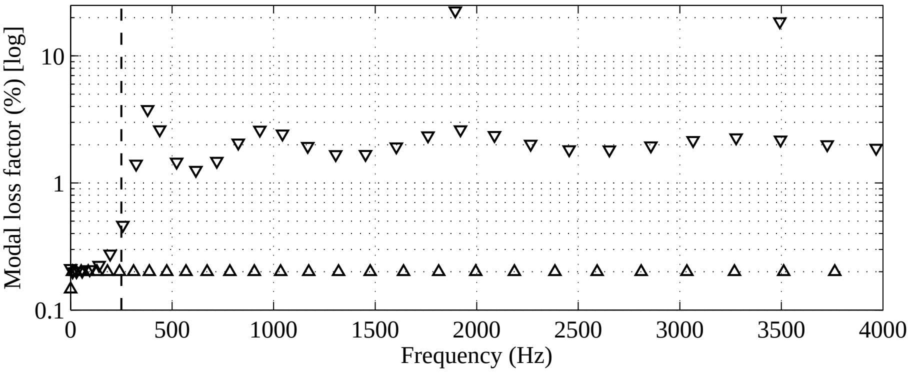

Figure 3.4: Modal loss factor for Reference (△) and ABH (▽) beams made of aluminium, and frequency limit for ABH efficiency (dashed line).

3.1.3.4 Modal Overlap Factor

The modal overlap factor is a convenient quantity to observe if one wishes to compare the experiment and the model in the framework of a mid or high frequency study. It embeds fine phenomena such as the change in modal density or the damping mechanisms, but allows to globally quantify and qualify the adequateness of the model. Fig. 3.5

represents the estimated MOF for the experimental reference and ABH cases and their simulated counterparts. One can remark that the hyper-damped and transverse modes are not represented since experiments did not allow to identify them: they are localised thus non observable using the experiment described in Sec. 2.2 and they induce a MOF far superior to 100%, according to the model. The plotted MOF is then an *apparent* MOF [15]. With carefully chosen parameters, one can see very similar tendencies on these plots in the ABH case. Especially interesting are the local maxima around 400, 900 and 2000 Hz which are present in both the experiment and the simulation; these are likely to come from the variations of the modal loss factor, observed on Fig. 3.4. Although some of these peaks are localised at the same frequencies than hyper-damped modes according to Fig. 3.4, the two phenomena are not related: a numerical analysis using different structural parameters does not yield matching frequencies; moreover there is no transverse behaviour in the shapes of the modes constituting these small peaks.

Over 3000 Hz, the model fails to reproduce experimental observations. One may think of an imperfect estimation of the experimental parameters. One can also remind that the model uses a very simple structural damping: combined with frequency-independent material loss factors, the Ross-Ungar-Kerwin model is a convenient way to express the effect of the damping layer but does not reflect the complexity of the vibrating layered structure, mainly due to its imperfections, the spatial variability of glueing and the relative importance of the layer versus the structure.

This figure shows the general effect of the ABH on the structure, which is the increase of its MOF. This way to characterize the frequency response is common for mid and high frequency problems. It appears here as a convenient approach to study the ABH effect on plate-like structure, on which the same fine phenomena take place.

3.2 Physical interpretation

3.2.1 Combined effects of thickness and loss factor

In order to understand how eigenvalues evolve from the reference case to the ABH case, intermediate structures are simulated by changing only the truncation thickness. Some examples of thickness profiles are plotted on Fig. 3.6(a) and results are given on Fig. 3.6(b) (● in grey levels), completing the results of Fig. 3.3(b).

From Fig. 3.6(b), it is clear that the imaginary part of a given eigenvalue decreases with the thickness of the tapered profile. This suggests a small increase in modal density : since the natural frequencies are shifted towards the bottom of the frequency range, there is more modes in a given range.

Another phenomenon is the increase of the real part of the eigenvalues with the decrease of the thickness of the profile, as seen in Sec. 3.1.3.1. This leads to a progressive augmentation of the modal loss factors in most of the cases. An explanation is a greater

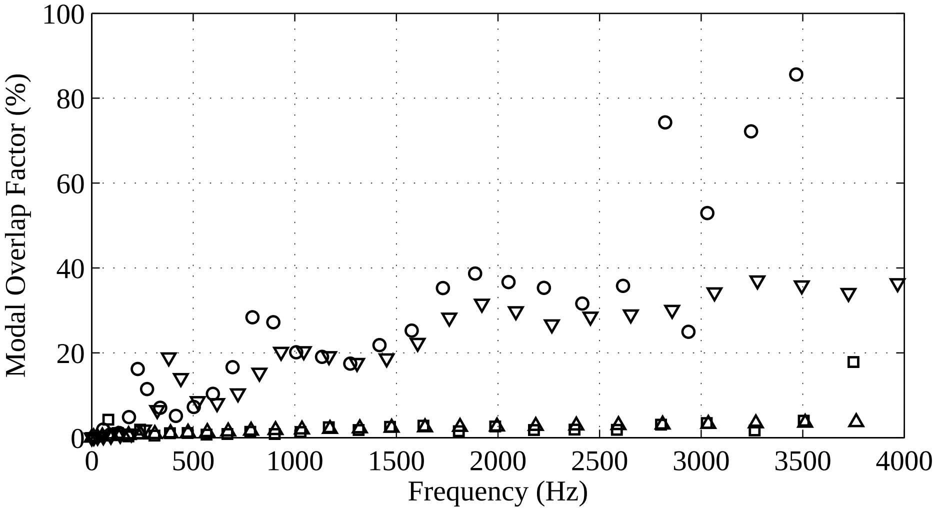

Figure 3.5: Simulated MOF for Reference (△) and ABH (▽) beams made of aluminium. For comparison, experimental MOF for Reference (□) and ABH (○) beams (published in [38]).

action of the damping layer at small thicknesses. However, as shown in the work of Georgiev *et al.* [57], for very small thicknesses, the bending stiffness and the added mass of the layer counterbalance their effects on the equivalent material loss factor.

Hyper-damped modes (such as modes 23 and 41 on Fig. 3.3(b)) appear at lower frequencies with the decrease of the truncation thickness. This lowering effect is much more pronounced for them than for the majority of modes. They add to the rest of the modes in a given frequency band and so have an effect on modal density. As with other modes, the real parts of the associated eigenvalues are moved towards the right of the spectrum, resulting in an increase of their loss factor as the truncation thickness decreases.

3.2.2 Trapped modes

Fig. 3.7 shows the modal shapes of modes 14, 23, 41 and 42 that are indicated on Fig. 3.3(b). The modal shapes are here represented on the transformed grid, on which the problem was solved (see Sec. 3.1.2). This means that the tapered region is magnified in an adapted manner which is convenient to observe the local behaviour of the ABH. Note that in this case the wavelength appears to be the same everywhere, which is not the case in reality.

For a given mode $\phi_n(x,y)$, the localisation of the kinetic energy is described by the localisation index I_k:

$$I_k = \frac{\int_0^b \int_0^{x_{\mathrm{ABH}}} \rho(x)\phi_k(x,y)^2 \mathrm{d}x\mathrm{d}y}{\int_0^b \int_0^L \rho(x)\phi_k(x,y)^2 \mathrm{d}x\mathrm{d}y}. \tag{3.21}$$

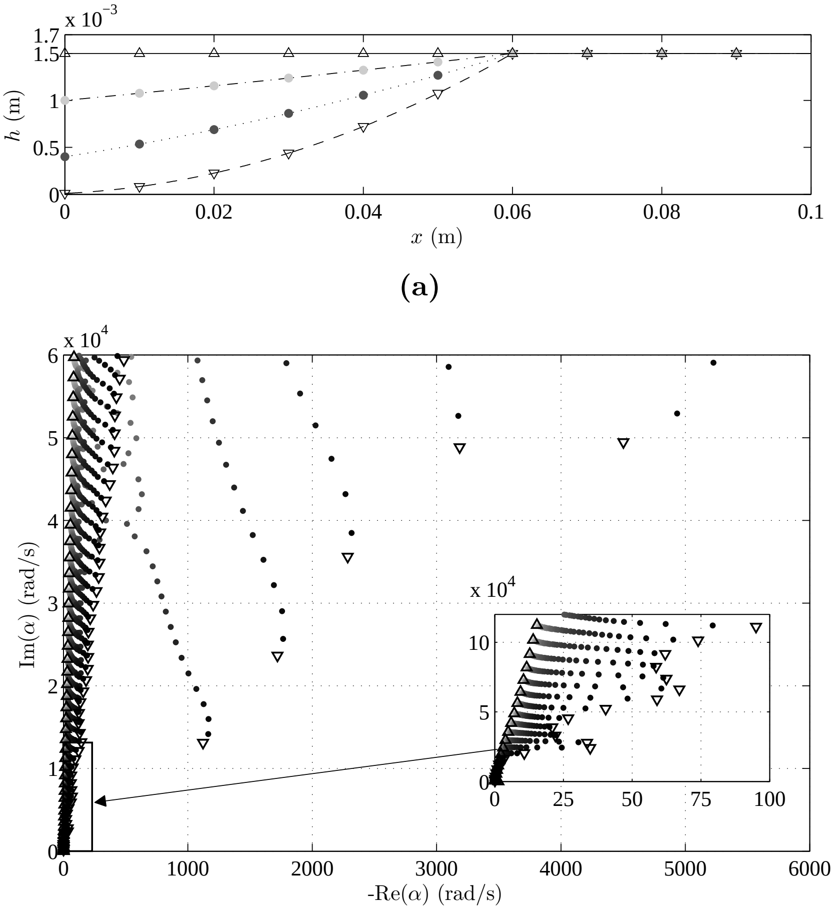

(a)

(b)

Figure 3.6: (a) Thickness profile and (b) spectrum of the complex eigenvalues of Reference (△), ABH ($h_t = 10$ µm) (▽) and intermediate structures, gradually thinned, between Reference and ABH (● in grey levels) (published in [38]).

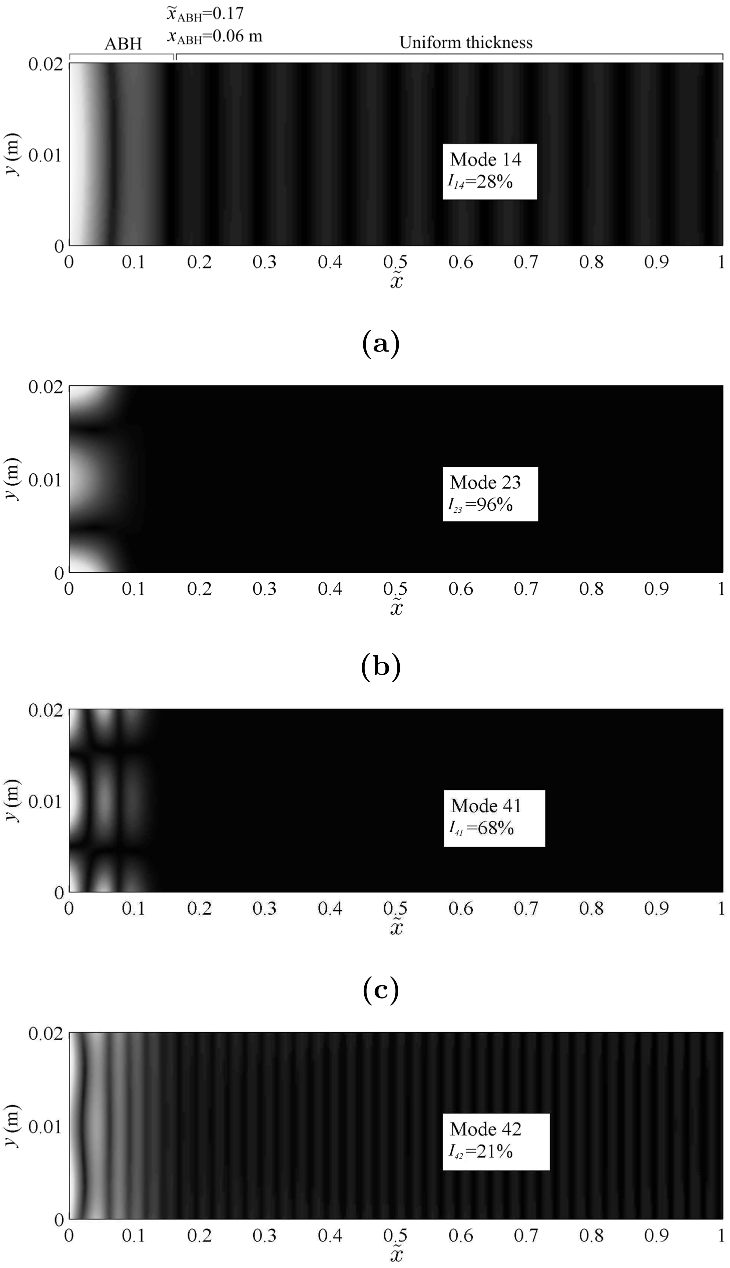

(a)

(b)

(c)

(d)

Figure 3.7: Moduli of the mode shapes (modulus) and localisation indicator for modes (a) 14, (b) 23, (c) 41 and (d) 42 in the ABH case. The ABH region is $x \in [0, \tilde{x}_{\rm ABH}]$. The axial coordinate is the transformed coordinate $\tilde{x}$ defined by Eq. 3.15 (published in [38]).

This indicator is simply the ratio between the kinetic energy in the varying thickness region ($0 \leq x \leq x_{\mathrm{ABH}}$) and the total kinetic energy in the structure. The same indicator can be defined for the modes of the reference beam; in this case, it is still the kinetic energy in the region $0 \leq x \leq x_{\mathrm{ABH}}$ that is used. In the reference case, the structure is uniform and the energy of a given mode tends to be uniformly distributed. It implies that the localisation index is low and tends to a constant value for each mode k. Results show values around 7%.

Modes 14 and 42 of ABH (Fig. 3.7(a) and (d)) are typical beam flexural modes. Their localisation index is between 20 and 30 %. The localisation of the energy originates from the higher amplitude and the smaller wavelength. This beam behaviour and this moderate localisation are common to the majority of modes among which modes 14 and 42 lie. Note also that the localisation in this case is higher than that of the uniform beam. The kinetic energy is localised in a region that has a high equivalent material loss factor, according to the Ross-Ungar-Kerwin model; it implies an important energy dissipation and it can be related to an augmentation of the global modal loss factor.

Modes 23 and 41 (Fig. 3.7(b) and (c)) are some of the hyper-damped modes (see Sec. 3.1.3.1). They have a strong localisation index (higher than 60 %) meaning they are in fact quasi-local modes. These modes have a locally two dimensional behaviour. One can infer that part of the very high damping of these comes from the extreme localisation, as for modes 14 and 42. It also comes from the transverse behaviour, since physically it implies more motion of the damping layer and, thus, a higher energy dissipation. The explanation of this transverse behaviour lies in the wavelengths being smaller than the width of the plate in this region. As the beam can be seen as a waveguide, such modes correspond to transverse modes of the guide. For curiosity sake, modes of similar shape are seen on clarinet reeds which also have a tapered, though empiric profile [124].

3.2.3 Modal density and correction length for the ABH beam

The purpose of this paragraph is to show that the specific tapered profile placed at one end of a otherwise uniform beam can lead to an increase of its modal density, as the experimental result (Fig. 2.5(a)) and the study of the eigenvalues (Fig. 3.6) suggest. Two parametric studies are made: the first one makes the truncation thickness h_t vary while the second one makes the exponent m of the profile vary. Results concern conservative structures without damping layer, in order to evaluate only the influence of the profile on the modal density. One has to remind that the damping layer modifies the real part of the flexural rigidity and the mass; it has indeed an influence on the eigenfrequencies, especially at low thicknesses, and thus modifies the obtained modal densities. The modification of modal density is then explained as a correction length induced by the tapered termination; this theory is supported by experimental results.

3.2.3.1 Effect of the truncation thickness

Fig. 3.8 shows the estimated modal densities for the flexural modes of the reference beam and three cases of ABH profile with different truncation thicknesses. Undoubtedly, there is an increase of modal density for the beams with tapered profiles compared to the reference beam. This increase can be related to the local change in wave speed. While for the reference beam, the modal density is proportional to $1/\sqrt{\omega}$ (see Eq. (2.4)), the repartition of modes is less predictable for the ABH beam. Moreover, the decrease of the truncation thickness is related to an increase in the modal density, and ultimately, the shape of the result does not have anything to do with the modal density of the uniform beam.

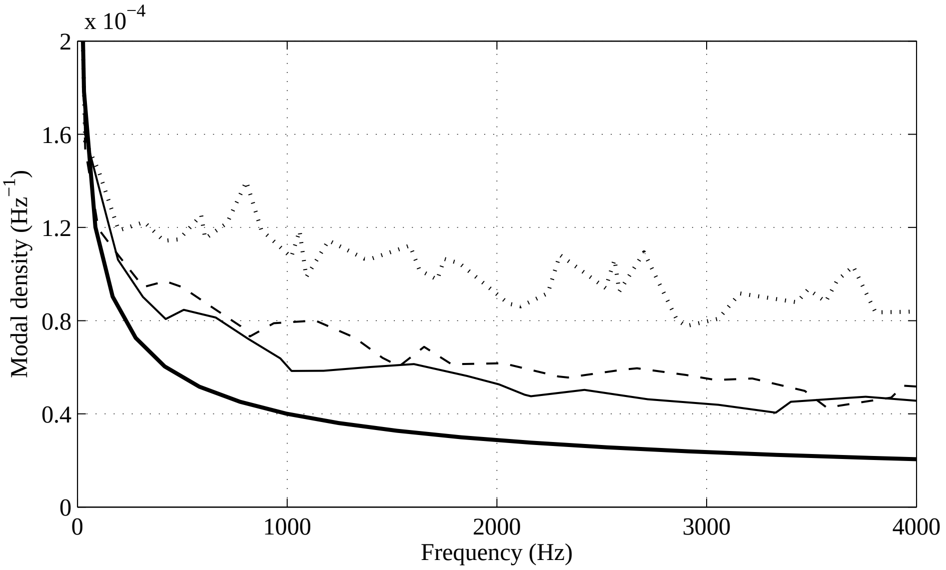

Figure 3.8: Numerical simulation of the modal density for the reference beam (thick full line) and ABH beams with different truncation thicknesses: 10 µm (thin full line), 5 µm (dashed line) and 1 µm (dotted line), and an exponent of $m = 2$.

3.2.3.2 Effect of the exponent of the power-law defining the thickness profile

Fig. 3.9 shows the modal densities for beams with tapered profiles having a different exponent, ranging from 2 to 3, and the same truncation thickness. A higher exponent gives a profile that is thin over a greater length. From these estimations, it can be concluded that a higher exponent leads to a higher modal density, but it is not as obvious as the case of a lower truncation thickness. This means that the thickness of the extremity influences more the modal density than the value of the exponent of the power-law defining the thickness profile. Practically, a structure will not have its modal density significantly increased if the lower limit in thickness is not overcome.

These results allow to conclude that a significant increase in modal density is unlikely to happen with the real damped structures, as it was seen in Fig. 2.5(c).

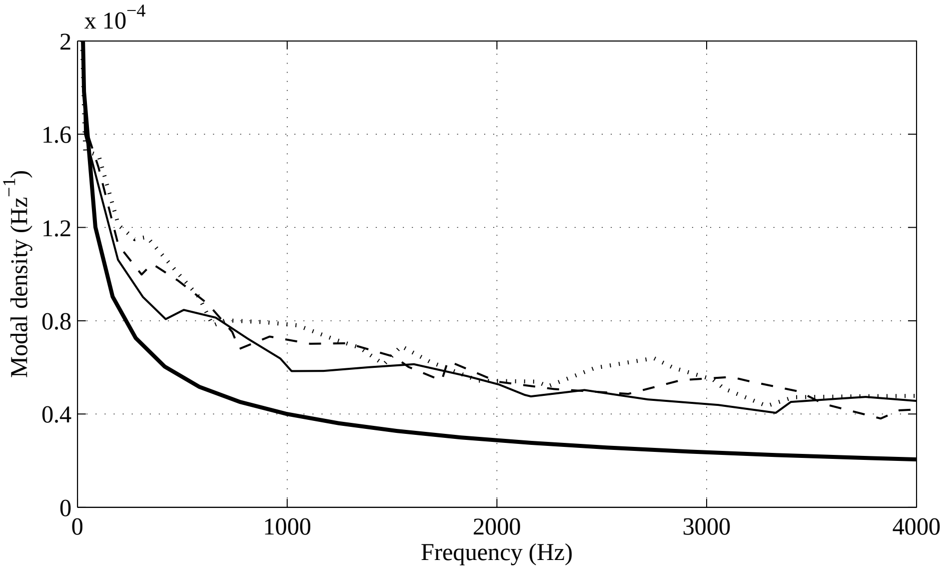

Figure 3.9: Numerical simulation of the modal density for the reference beam (thick full line) and ABH beams with different exponents: $m = 2$ (thin full line), 2.5 (dashed line) and 3 (dotted line), and a truncation thickness of $h_t = 10$ µm.

3.2.3.3 Correction length induced by ABH

3.2.3.3.1 Definition

1140 An explanation of the small modification of the modal density is proposed here. For this matter, a special attention is paid to the phase of the reflection coefficient that is estimated in Sec. 2.3.2 in the experimental case. The phase of the reflection coefficient of the free end of the uniform aluminium beam (named R_{Ref}) is estimated at distance l_{ABH} (see Fig. 2.1) from the edge and plotted on Fig. 2.16 (full light grey line). It is 1145 compared with the phase the reflection coefficient of the aluminium ABH termination (named R_{ABH}). The phase discrepancies between R_{Ref} and R_{ABH} are studied in order to investigate the role of the ABH profile. The phase of R_{ABH} decreases more than the phase of R_{Ref}, for the same actual length. It means that an incident wave spends more time in the tapered profile because it is slowed down. An alternative point of view is 1150 to consider a uniform profile longer than the tapered profile, in which the bending wave speed remains constant (see Fig. 3.10). This leads to define a correction length as it can be done in acoustic pipes to take into account acoustic radiation at the open end of the pipe [72]. Hence, the correction length Δl provided by the ABH profile corresponds to the length of uniform cross-section that should be added to l_{ABH} in order obtain the same 1155 phase. The reflection coefficient of ABH termination estimated at $x = 0$ (referring to Fig. 2.1) can be written as

$$R_{\text{ABH}} = |R_{\text{ABH}}| e^{2\text{j}k_f(l_{\text{ABH}}+\Delta l)}, \tag{3.22}$$

where k_f is the wavenumber in the beam of uniform cross-section. The argument of Eq. (3.22) yields

$$\mathrm{Arg}(R_{\mathrm{ABH}}) = 2\mathrm{Re}\,(k_f)\, l_{\mathrm{ABH}} \left(1 + \frac{\Delta l}{l_{\mathrm{ABH}}}\right), \tag{3.23}$$

where $\Delta l / l_{\mathrm{ABH}}$ is the dimensionless correction length.

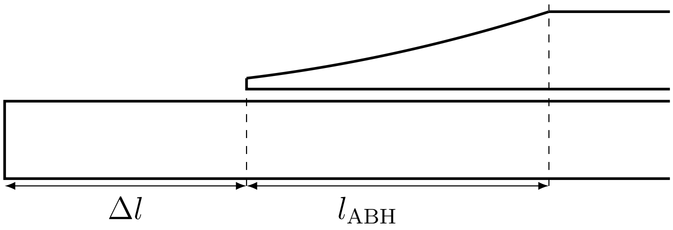

Figure 3.10: Scheme of the correction length induced by ABH.

1160 3.2.3.3.2 Experimental results

From the experimental results, the calculated correction length is plotted on Fig. 3.11 for aluminium and polymer ABH beams. The correction length for the aluminium case is remarkably constant on the 0-9 kHz range. The value close to 0.8 m means that a tapered and covered profile of 0.06 m is equivalent to a uniform profile of 0.11 m (i.e. the 1165 length is approximately doubled) from the phase viewpoint. This observation even less conclusive in the polymer case still yields an quasi-constant correction length close to 1 on the 0-4 kHz range. This correction length phenomenon has been theoretically showed by Mironov [95] for the case of a retarding tube termination, constituting the acoustical analogy of the ABH termination for flexural waves studied in this paper.

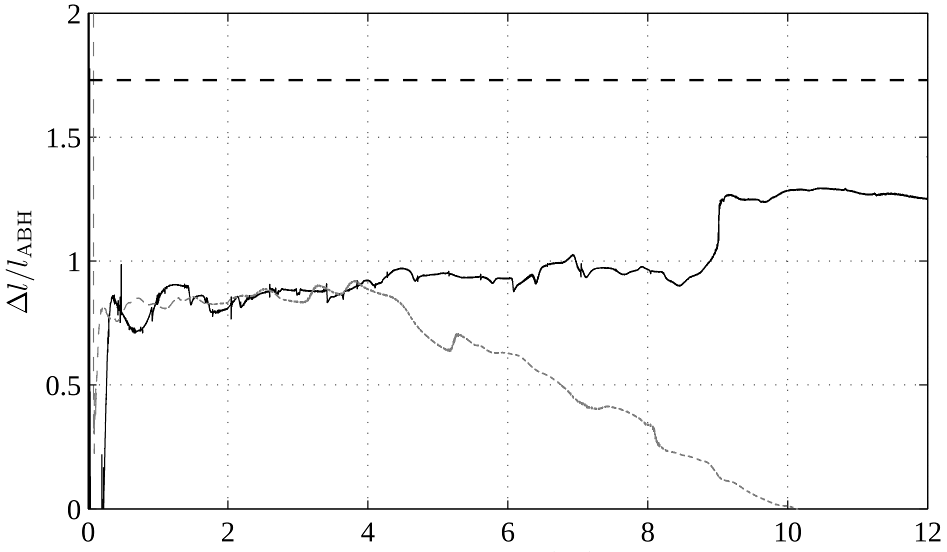

Figure 3.11: Measured dimensionless correction length $\Delta l / l_{\mathrm{ABH}}$ due to ABH termination for aluminium (full black line) and polymer (dashed grey line) ABH beams.

3.2.3.3.3 Expression of the correction length

An analytical estimation of the correction length induced by a quadratic profile can be made. Using the geometrical acoustics model of [93] for the ABH termination (while keeping the notations of Fig. 2.1(a)), it is possible to derive

$$\mathrm{Arg}(R_{\mathrm{ABH}}) = 2\mathrm{Re}\,(\Phi)\,, \quad \text{with} \quad \Phi = \int_{-l_{\mathrm{ABH}}}^{0} k(s)\,\mathrm{d}s. \tag{3.24}$$

Therefore

$$\frac{\Delta l}{l_{\mathrm{ABH}}} = \left(\frac{\mathrm{Re}\,(\Phi(l_{\mathrm{ABH}}))}{l_{\mathrm{ABH}}\mathrm{Re}\,(k_f)} - 1\right). \tag{3.25}$$

Noting that

$$k(x) = \sqrt[4]{\frac{12\rho(1-\nu^2)\omega^2}{Eh(x)^2}}, \quad \text{and} \quad k_f = \sqrt[4]{\frac{12\rho(1-\nu^2)\omega^2}{Eh_0^2}}, \tag{3.26}$$

(assuming a conservative case), the relative correction length is finally

$$\frac{\Delta l}{l_{\mathrm{ABH}}} = \left(\frac{l_t}{l_{\mathrm{ABH}}}\ln\left(\frac{l_t}{l_t - l_{\mathrm{ABH}}}\right) - 1\right). \tag{3.27}$$

This expression only depends on the length ratio (or thickness ratio) but not on the frequency. The result with the numerical values of Tab. 2.1 (aluminium) is plotted on Fig. 3.11 (dashed black line). It is much higher than the experimental result.

3.2.3.3.4 Remark on the modal density

The modal density d of a uniform beam depends on the length L of the structure according to the following relation [137]:

$$d(\omega) = \frac{L}{\pi c_\gamma(\omega)}, \tag{3.28}$$

for basic boundary conditions, where $c_\gamma(\omega)$ is the group velocity of flexural waves. Hence the variation of modal density $\Delta d(\omega)$ due to the correction length Δl on the homogeneous beam of length L is given by

$$\Delta d(\omega) = \frac{\Delta l}{\pi c_\gamma(\omega)}. \tag{3.29}$$

The numerical values of Tab. 2.1 (aluminium) give a variation Δd=4.3×10^{-5} Hz^{-1} at 2000 Hz, which has the same order of magnitude than the results plotted on Fig. 3.8 (black full thin line).

These observations can be put in parallel with the coordinate change that is made in Sec. 3.1.2 for the numerical resolution. Indeed, the numerical scheme uses a distorted space that magnifies the length of the ABH region, compared to the length of the uniform region but keep a constant wavelength and speed along the whole transformed structure. It thus corresponds well to a structure that is homogeneous but longer, just as it is shown here.

1195 3.2.4 Effect of the stiffness of the layer

In order to complete the parametric study of the damping layer characteristics done by Georgiev *et al* [29, 57], Fig. 3.12(a) shows eigenvalues of the structure (parameters of Tab. 3.1) with a damping layer having E_l=1 GPa instead. Compared to Fig. 3.6, it is noticeable that the angle between the imaginary axis and the direction $\big((0,0),(-\mathrm{Re}(\alpha_k),\mathrm{Im}(\alpha_k))\big)$
1200 is similar or slightly lower for beam modes, with however a decrease of eigenfrequencies. Moreover, an increased number of hyper-damped modes is found; this is related to the decrease of stiffness at the extremity. Two 'families' of hyper-damped modes appear that possess either a lower or higher modal loss factor. Fig. 3.12(b) shows that the drop of parameter E_l influences positively only the peak value of equivalent loss factor $\eta(x)$; it is
1205 lower otherwise. The softer damping layer seems then of practical interest only for the trapped hyper damped modes.

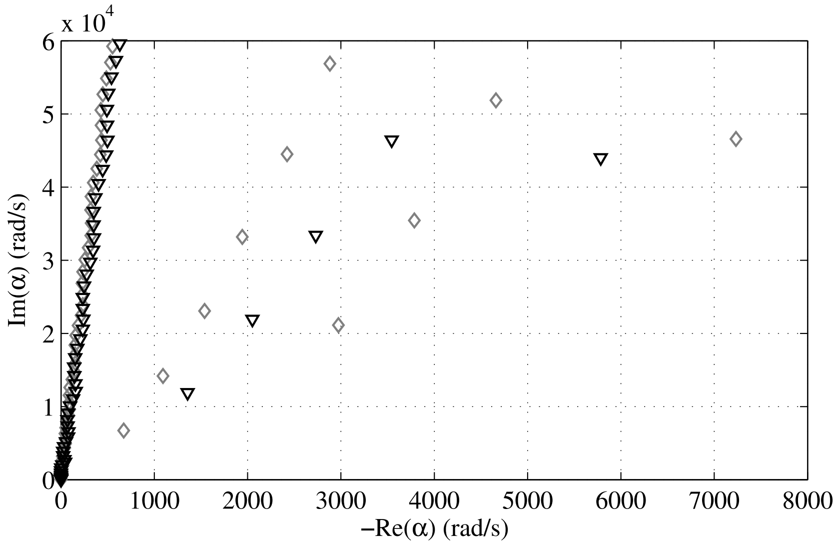

(a)

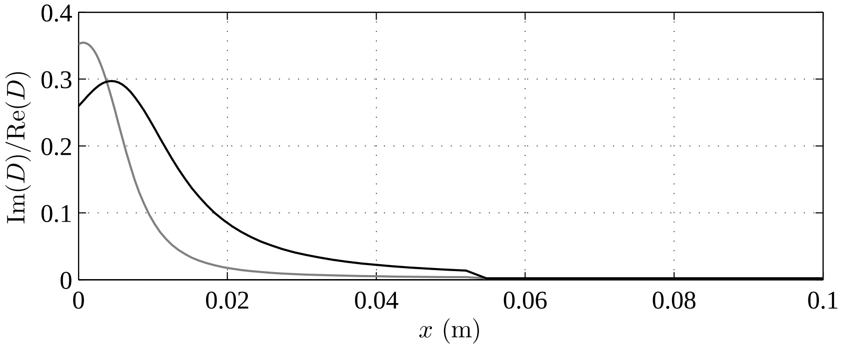

(b)

Figure 3.12: (a) Spectrum of the complex eigenvalues and (b) Equivalent loss factor for ABH with E_l=7 GPa ($\triangledown$, black) and E_l=1 GPa ($\diamond$, grey).

3.3 Validation of the model using R measurements

3.3.1 Simulation of R

The inhomogeneous plate model developed in Sec. 3.1.1 can be modified and used to compute the reflection coefficient of the ABH extremity. The following equation of motion is solved:

$$\nabla^2(D(x)\nabla^2 w(x,y)) - (1-\nu)\Big(\frac{\partial^2 D(x)}{\partial x^2}\frac{\partial^2 w(x,y)}{\partial y^2}\Big) \\ - \rho(x)h(x)\omega^2 w(x,y) = F\delta(x-x_f)\delta(y-y_f), \quad (3.30)$$

where the right member is an harmonic excitation at (x_f, y_f) of amplitude F and angular frequency ω. It allows to compute displacement field and mobility transfer functions. The discretized problem leads to the matrix problem

$$(\mathbf{K} - \omega^2\mathbf{M})\mathbf{W} = \mathbf{F}, \quad (3.31)$$

where $\mathbf{K}$ and $\mathbf{M}$ are respectively the complex stiffness matrix and the mass matrix of the structure, $\mathbf{F}$ is the force vector and $\mathbf{W}$ is the displacement field. Using the numerical model, frequency responses are simulated and can be post-processed using the estimation method described in Sec. 2.3.2.1, with parameters of Tab. 3.1. The result for the reflection coefficient is plotted on Fig. 3.13 (full line) along with the reflection coefficient given by the beam waveguide model [57].

On Fig. 3.13, plane wave and plate models yield the same results when fed with the same parameters of Tab. 2.1. Actually, the phase of the reflection coefficient is slightly different; it can be attributed to a small numerical dispersion [14] in the finite difference scheme of the plate model, leading to a difference between theoretical and actual wave speed in the structure.

3.3.2 Comparison between simulated and experimental reflection coefficients

A comparison between experimental beam and simulated counterpart has been shown on Fig. 3.5 by looking at the MOF of the structure. It is interesting to do the same comparison on the reflection coefficient. Using the model of Sec. 3.3.1 (parameters of Tab. 3.1), the reflection coefficient is shown on Fig. 3.14. It is compared with the measurements of R done in Sec. 2.3.2. As expected the comparison hold quite well on this indicator: the modulus of the experimental reflection coefficient presents oscillations the same way the model does, and the parameters give the same order of magnitude. The phase of the reflection coefficient unwraps in a remarkably similar manner for the two cases. The modulus and phase can be linked to the similarity of both modal loss factors and eigenfrequencies (see Sec. 3.1.3.4).

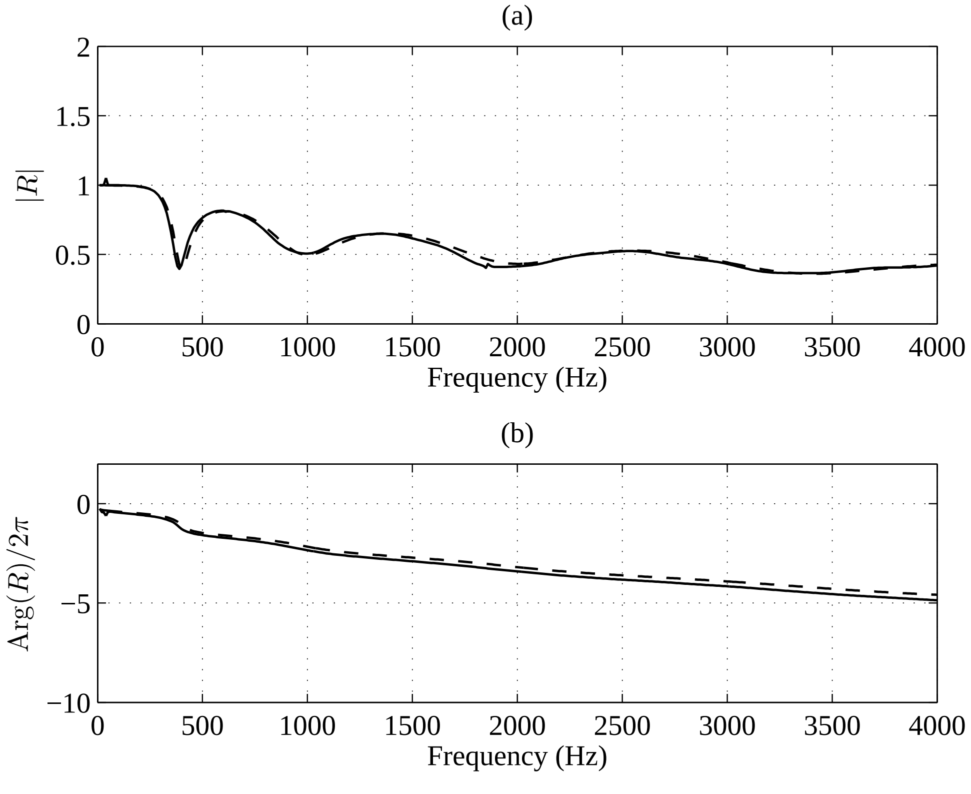

Figure 3.13: Reflection coefficient calculated with beam waveguide model (dashed line) and plate model (full line) in (a) modulus and (b) phase.

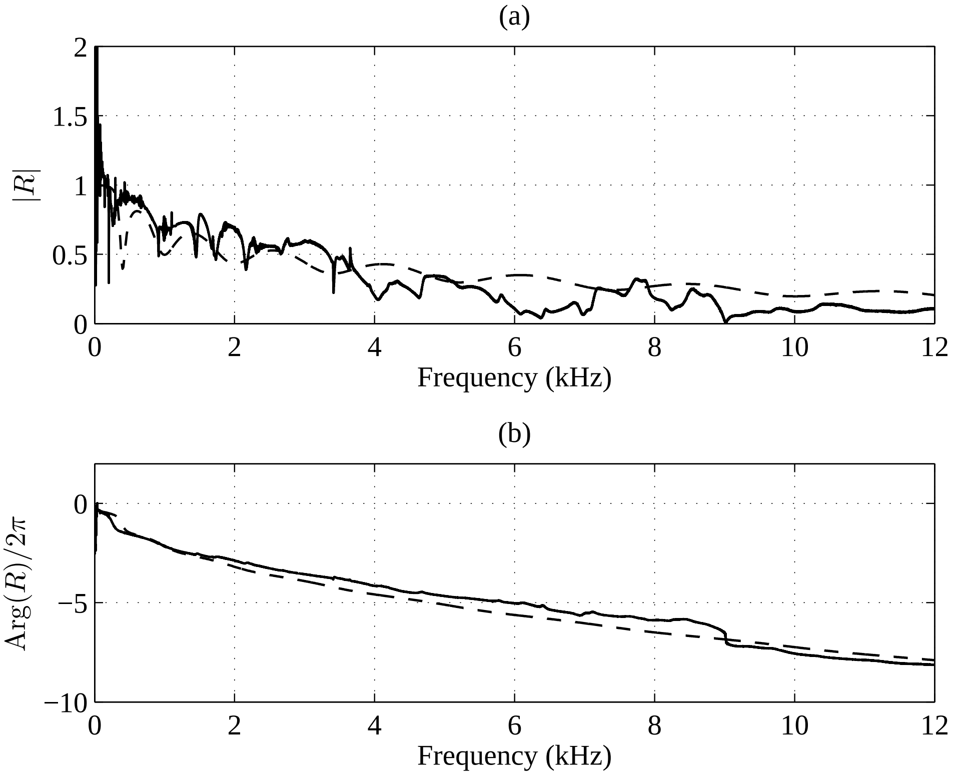

Figure 3.14: Reflection coefficients: from measurements of Sec. 2.3.2 (full line) and plate model of Sec. 3.3.1 with parameters of Tab. 3.1 (dashed line) in (a) modulus and (b) phase.

3.4 Conclusions

A numerical model based on the finite difference method has been developed for ABH beams and plates in order to explain the experimental observations made in Chap. 2. The main conclusions of this chapter are the followings:

- The modal loss factors of an ABH beam are much higher than those of the corresponding uniform beam. Numerical computation of the complex mode shapes and complex eigenfrequencies are obtained. It permits to relate the increase of the loss factor with a higher localisation of the energy in the ABH region, since the local material loss factor in this region is higher due to the viscoelastic damping layer. The heterogeneity of both the bending stiffness and the equivalent material damping is emphasised as the cause of these phenomena.
- Transverse and local modes of vibration for the ABH are also found by numerical simulation. As their energy is very localised in the tapered and damped region, they are hyper-damped.
- The modal density of an ABH beam is slightly higher tan the corresponding reference beam.
- Both the modal density and the modal loss factors contribute to a higher modal overlap factor in the ABH case. Such an indicator is a convenient way to quantify the damping effect of ABH on the frequency response curve. With values as high as 40% for the MOF in the numerical case, the ABH effect applied to the conventional beam studied in this document still classifies it as a low frequency phenomenon.
- On the other hand, it is shown that the increase in modal density essentially comes from the truncation thickness but that this increase is not significant in the practical cases.
- The phase of the reflection coefficient measured in Chap. 2 allows to define a correction length for the tapered termination that appears to be quasi-constant with respect to frequency; This correction length can be related to the variation of modal density.
- A good agreement is found between the simulated and measured reflection coefficient: the order of magnitude and the main variations of R with the frequency are approached.

Chapter 4

SCATTERING AND DAMPING INDUCED BY AN IMPERFECT ABH TERMINATION

Manufacturing imperfections cannot be avoided in practice. We propose in this chapter to investigate the role of these defaults in the behaviour of ABH terminations. It will be seen that an irregular edge creates couplings between the incident plane wave to excite the local modes of the extremity. These couplings have a positive and significant effect on the damping induced by the ABH termination, all things being equal. Sec. 4.2 presents an experimental observation of the effect of imperfections. A model is developed in Sec. 4.3 in order to compute the modal coupling in the inhomogeneous plate seen as a multimodal structural waveguide, using a Levy-type solution [60]. From a numerical resolution of the model, typical results for the reflection coefficent of an ABH termination are presented in Sec. 4.4 and interpretations for the phenomena are proposed. Effects of variations of the imperfection characteristics are also investigated in a parametric study on the reflection coefficient.

4.1 Imperfections on ABH profiles

Most of the published literature [75, 57] and the work done in Chap. 3 consider a perfect tapered extremity: the free edge is considered as straight and normal to the direction x of propagation. The consequence is that an incident plane wave propagating along the x-axis is staying plane and that the reflected wave is also stricly plane. Thus there should be no excitation of the trapped eigenmodes mentioned in Chap. 3. However the practical realisation fails the assumption of perfect edge because the manufacture of such small thicknesses is difficult and leads to irregular and teared extremities (see Figs. 4.1(a) and (b)). Moreover, it is observed in Sec. 2.3.1 that the wave is not plane anymore for certain frequencies. Bowyer *et al.* [19] study experimentally imperfections of ABH by comparing an imperfect termination and a shorter thus thicker perfect termination; From this experimental comparison, they conclude that even imperfect, a thinner extremity has a better damping performance. It is proposed here to observe what effects are induced by imperfections for a given thickness at the end. A theoretical framework for analysing these experimental results is also proposed.

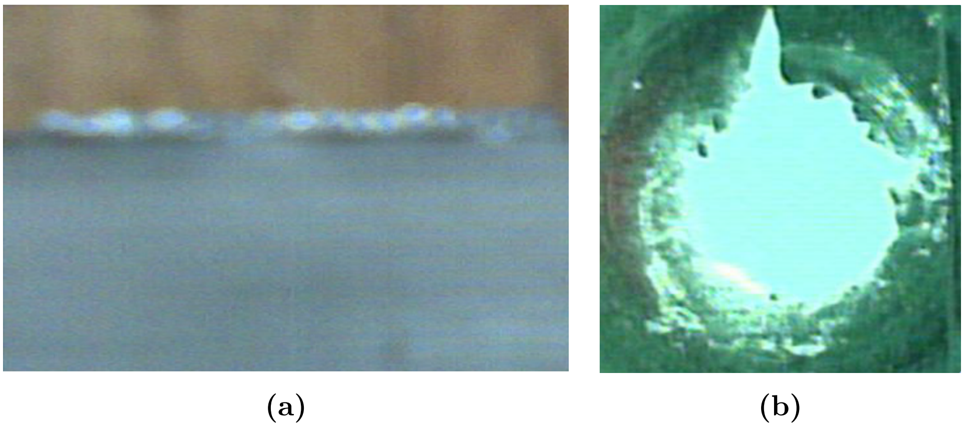
(a) (b)

Figure 4.1: (a) Machine damage to a wedge tip (after [19]) and (b) teared edge of a circular ABH profile at the truncation radius (after [10]).

4.2 Experimental investigations on an imperfect ABH termination

4.2.1 Experimental setup

This experiment uses the setup described in Sec. 2.3.2. An unique sample is used and consists in an aluminium beam with an ABH extremity, whose parameters are described in Tab. 2.1 (see Fig. 4.2(a)). The tip is as clean and undamaged as possible. A thin damping layer (desk tape) is stuck on the flat side of the tapered profile (see Fig. 4.2(b)). The layer is deliberately chosen as thin and relatively inefficient: it does not add stiffness to the tapered profile and provides a damping low enough to observe small perturbations. This configuration is referred as "non-damaged". After a first measurement of the reflection coefficient of the beam, artificial damages (small cuts) are made at the tip of the tapered profile, using a blade (see Fig. 4.2(c)). This second configuration is referred as "damaged". A second measurement of the reflection coefficient is then made on the damaged beam.

4.2.2 Results

The reflection coefficients for the ABH extremity before and after making the imperfections are shown on Fig. 4.3. The reflection coefficient for the non-damaged extremity

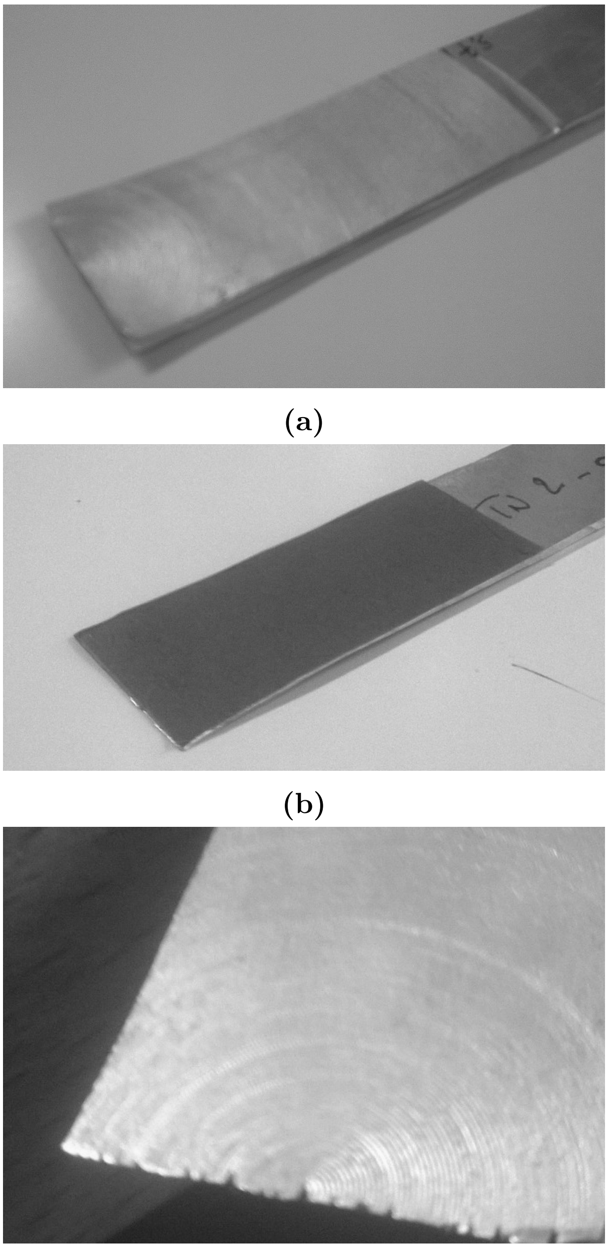

(a)

(b)

(c)

Figure 4.2: (a) Machined side of the tapered profile, (b) flat and covered side of the tapered profile and (c) extremity after making cuts.

is rather high and displays important variations with several localised minima. Note that R is slightly noisy at low frequency because the close-to-unity coherence needed for a smooth estimation is difficult to obtain when the tapered extremity is poorly damped. It is reminded that the measurement method for such a beam remains valid until 16 kHz, as discussed in Sec. 2.3.2.

After making several random cuts in the tapered extremity, the reflection coefficient is definitely modified: it presents more minima close to zero. In some frequency ranges, the reflection coefficient is lower than for the non-damaged extremity (2.8–3.3, 4.4–5.2 and 8.6–12 kHz) while the frequency range 7.4–8.3 kHz actually displays a higher reflection coefficient for the damaged extremity.

These results show that the experimental reflection coefficient is very sensible to the quality of the extremity when the ABH is covered with an relatively inefficient damping layer. Sec. 4.3 provides a model and a theoretical background allowing to explain these experimental results.

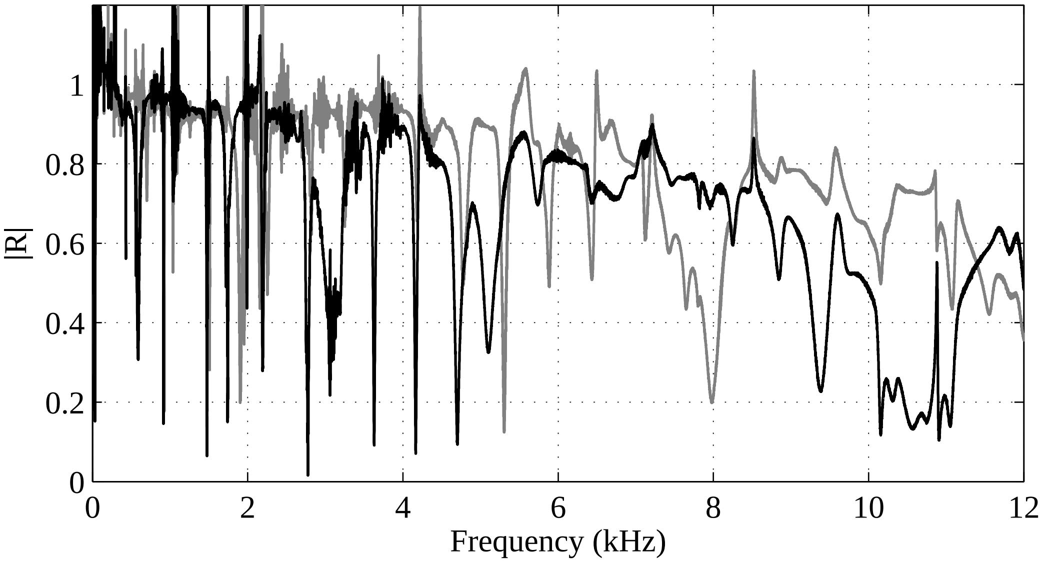

Figure 4.3: Experimental comparison of $|R|$ for non damaged (gray line) and damaged (black line) ABH termination

4.3 Model of an imperfect ABH termination

4.3.1 Multimodal waveguide formulation

The ABH extremity (see Fig. 4.4)is considered as an inhomogeneous structural waveguide. In order to describe coupling phenomena between guided modes at the extremity from imperfect edge conditions and to extend the study of the reflection coefficient made in Chap. 2, the aim is to obtain the reflection matrix of the extremity or of a region of the waveguide. This reflection matrix can be obtained by either the knowledge of the impedance matrix of the waveguide when it is closed, or as part of the scattering matrix of a region of the waveguide. We propose in this section to derive a Riccati equation for the impedance matrix. This equation is solved numerically. Using the same formalism, a method for computing the scattering of a waveguide region is also developed.

4.3.1.1 Governing equations

The governing equations for the flexural motion of plate with inhomogeneities along the longitudinal x-direction (plate parameters remains invariant along transverse y-direction), and in harmonic regime (with the $e^{-\mathrm{j}\omega t}$ time convention) are [84]:

$$w = w(x,y) \tag{4.1}$$

$$\theta_x(x,y) = \frac{\partial w}{\partial x}, \tag{4.2}$$

$$M_x(x,y) = -D\left(\frac{\partial^2 w}{\partial x^2} + \nu\frac{\partial^2 w}{\partial y^2}\right), \tag{4.3}$$

$$M_y(x,y) = -D\left(\frac{\partial^2 w}{\partial y^2} + \nu\frac{\partial^2 w}{\partial x^2}\right), \tag{4.4}$$

$$M_{xy}(x,y) = -D(1-\nu)\frac{\partial^2 w}{\partial x\partial y}, \tag{4.5}$$

$$Q_x(x,y) = \frac{\partial M_x}{\partial x} + \frac{\partial M_{xy}}{\partial y}, \tag{4.6}$$

$$Q_y(x,y) = \frac{\partial M_{xy}}{\partial x} + \frac{\partial M_y}{\partial y}, \tag{4.7}$$

$$\frac{\partial Q_x}{\partial x} + \frac{\partial Q_y}{\partial y} = -\rho h\omega^2 w, \tag{4.8}$$

where $w(x,y)$ is the displacement, $\theta_x(x,y)$ and $\theta_y(x,y)$ are the slopes along x and y-direction, $M_x(x,y)$ and $M_y(x,y)$ are the bending moments around x and y, $M_{xy}(x,y)$ is the twisting moment, $Q_x(x,y)$ and $Q_y(x,y)$ are the shear forces, $D(x)$ is the bending stiffness, ν is the Poisson's ratio, $\rho(x)$ is the mass density, $h(x)$ is the thickness and ω is the angular frequency. Moreover, the total shear forces V_x and V_y including the effects of the twisting moments are defined:

$$V_x(x,y) = Q_x + \frac{\partial M_{xy}}{\partial y} = \frac{\partial M_x}{\partial x} + 2\frac{\partial M_{xy}}{\partial y}, \tag{4.9}$$

$$V_y(x,y) = Q_y + \frac{\partial M_{xy}}{\partial x} = \frac{\partial M_y}{\partial y} + 2\frac{\partial M_{xy}}{\partial x}. \tag{4.10}$$

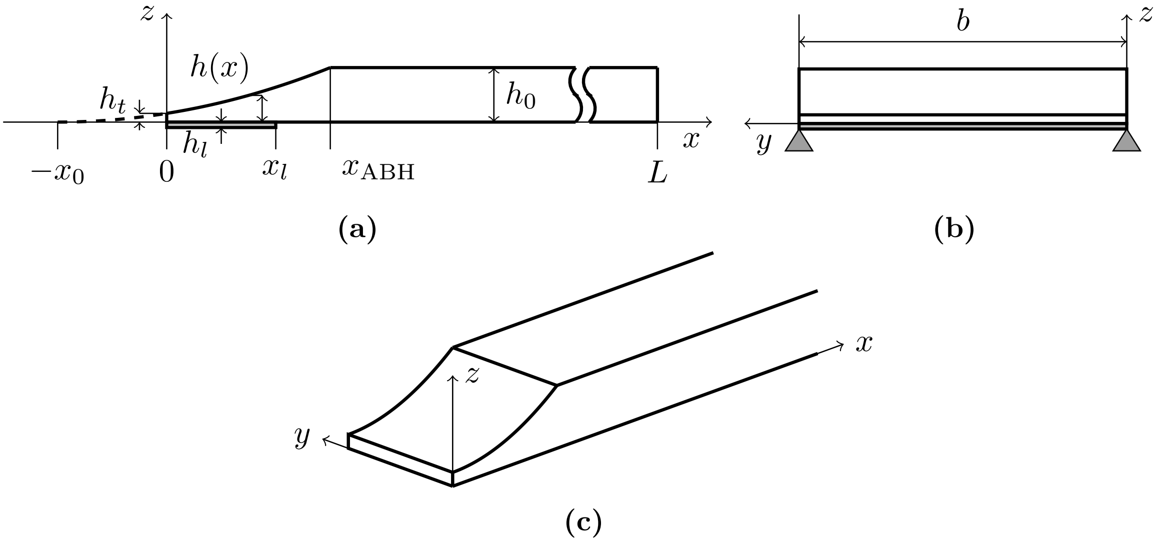

Figure 4.4: Model of plate with ABH extremity: edges along x are simply supported, edges along y are free. (a) Side view, (b) front view and (c) perspective.

Bending stiffness $D(x)$ and thickness $h(x)$ describe the waveguide and their expressions are given by (see Fig. 4.4)

$$D(x) = \frac{Eh(x)^3}{12\rho(1-\nu^2)}(1 - \mathrm{j}\eta(x)), \tag{4.11}$$

where E is the Young's modulus of the plate material and $\eta(x)$ is the loss factor, and the thickness is

$$h(x) = \begin{cases} h_0 \frac{(x+x_0)^m}{(x_0+x_{\mathrm{ABH}})^m} & \text{if} \quad x \leq x_{\mathrm{ABH}}, \\ h_0 \quad \text{if} \quad x > x_{\mathrm{ABH}}. \end{cases} \tag{4.12}$$

To take into account the effect of the viscoelastic layer can be modelled by an equivalent loss factor [116] which depends on x via [75]

$$\eta(x) = \begin{cases} \eta_p, \quad \text{if} \quad x \leq x_l, \\ \eta_p + \eta_l \frac{3E_l h_l}{Eh(x)}, \quad \text{if} \quad x > x_l, \end{cases} \tag{4.13}$$

where η_p is the loss factor of the plate, and E_l, η_l h_l the Young's modulus, the loss factor and the thickness of the viscoelastic layer, respectively.

Consider now the relations between variables w, θ_x, M_x and V_x and their first-order partial derivatives with respect to x. After several derivations detailed in Appendix A.4, the following relations are obtained:

$$\frac{\partial w}{\partial x} = \theta_x, \tag{4.14}$$

$$\frac{\partial \theta_x}{\partial x} = -\frac{1}{D}M_x - \nu\frac{\partial^2 w}{\partial y^2}, \tag{4.15}$$

$$\frac{\partial M_x}{\partial x} = V_x - 2(1-\nu)D\frac{\partial^2 \theta_x}{\partial y^2}, \tag{4.16}$$

$$\frac{\partial V_x}{\partial x} = -\rho h\omega^2 w + D(1-\nu^2)\frac{\partial^4 w}{\partial y^4} - \nu\frac{\partial^2 w}{\partial y^2}. \tag{4.17}$$

4.3.1.2 Definition of the waveguide

For simplicity, the two edges along x (y=0 and y=b) are simply supported, allowing to write a Levy-type analytical solution [60, 83, 136] for Eqs. (4.14)–(4.17) as a product of beam functions. Such lateral boundary conditions define the waveguide which will be studied. This waveguide is represented on Fig. 4.4(c) and is called a Levy-waveguide. Note that this choice automatically rules out a direct comparison with the experiment made with beams. The two edges along y (x=0 and x=L) are free. The boundary condition of the edge $x = 0$ is modified in Sec. 4.3.2 for taking into account the imperfect extremity.

4.3.1.3 Multimodal expansion

Each variable $g(x, y)$ (w, θ_x, M_x and V_x) is then written as the multimodal expansion

$$g(x,y) = \sum_{q=1}^{\infty} g_q(x)\Psi_q(y), \tag{4.18}$$

where

$$\Psi_q(y) = \sqrt{2}\sin\left(\frac{q\pi}{b}y\right) \tag{4.19}$$

are the modes of a simply supported beam [61] also called the transverse modes of the waveguide. The modes are orthogonal and verify

$$\frac{1}{b}\int_0^b \Psi_q(y)\Psi_j(y)\,\mathrm{d}y = \delta_{qj}, \tag{4.20}$$

where δ_{qj} is the Kronecker symbol and b is the width of the plate (i.e. the length of the transverse "beam").

The projection of Eqs. (4.14)-(4.17) on the transverse modes yields

$$\frac{\partial w_q}{\partial x} = \theta_{xq}, \tag{4.21}$$

$$\frac{\partial \theta_{xq}}{\partial x} = -\nu w_q \frac{1}{b}\int_0^b \frac{\partial^2 \Psi_q}{\partial y^2}\Psi_q\,\mathrm{d}y - \frac{1}{D}M_{xq}, \tag{4.22}$$

$$\frac{\partial M_{xq}}{\partial x} = -2(\nu-1)D\theta_{xq}\frac{1}{b}\int_0^b \frac{\partial^2 \Psi_q}{\partial y^2}\Psi_q\,\mathrm{d}y + V_{xq}, \tag{4.23}$$

and

$$\frac{\partial V_{xq}}{\partial x} = -\rho h \omega^2 w_q + D(1-\nu^2) w_q \frac{1}{b}\int_0^b \frac{\partial^4 \Psi_k}{\partial y^4} \Psi_q \,\mathrm{d}y - \nu M_{xk} \frac{1}{b}\int_0^b \frac{\partial^2 \Psi_q}{\partial y^2} \Psi_q \,\mathrm{d}y. \tag{4.24}$$

In practice, the infinite sums are truncated to K modes. The $K \times K$ matrices $\mathbf{I_2}$ and $\mathbf{I_4}$ are defined as

$$\begin{aligned} I_{2qj} &= \frac{1}{b}\int_0^b \frac{\partial^2 \Psi_q}{\partial y^2} \Psi_j \,\mathrm{d}y, \\ I_{4qj} &= \frac{1}{b}\int_0^b \frac{\partial^4 \Psi_q}{\partial y^4} \Psi_j \,\mathrm{d}y. \end{aligned} \tag{4.25}$$

Furthermore, considering the expression of Ψ_q (see Eq. (4.19)), Eq. (4.25) leads to analytical expressions:

$$\begin{aligned} I_{2qj} &= -\left(\frac{q\pi}{b}\right)^2 \delta_{qj}, \\ I_{4qj} &= \left(\frac{q\pi}{b}\right)^4 \delta_{qj}. \end{aligned} \tag{4.26}$$

4.3.1.4 State vector formulation

Eqs. (4.14)-(4.17) can finally be rewritten as the following state equation

$$\frac{\mathrm{d}}{\mathrm{d}x}\mathbf{W}(x) = \mathbf{H}(x)\mathbf{W}(x), \tag{4.27}$$

where the state vector $\mathbf{W}(x)$

$$\mathbf{W}(x) = \begin{bmatrix} \mathbf{w}(x) \\ \theta_{\mathbf{x}}(x) \\ \mathbf{M_x}(x) \\ \mathbf{V_x}(x) \end{bmatrix}, \tag{4.28}$$

is the concatenation of displacement, slope, bending moment and force modal vectors. For example:

$$\mathbf{w}(x) = {}^{\mathrm{T}}[w_1(x), w_2(x), ..., w_K(x)]. \tag{4.29}$$

Matrix $\mathbf{H}$ embeds the plate equations and writes

$$\mathbf{H}(x) = \begin{bmatrix} \mathbf{H}_1(x) & \mathbf{H}_2(x) \\ \mathbf{H}_3(x) & \mathbf{H}_4(x) \end{bmatrix}, \tag{4.30}$$

with

$$\begin{aligned} &\mathbf{H}_1(x) = \begin{bmatrix} \mathbb{O} & \mathbb{I} \\ -\nu \mathbf{I_2} & \mathbb{O} \end{bmatrix}, \quad \mathbf{H}_2(x) = \begin{bmatrix} \mathbb{O} & \mathbb{O} \\ -\mathbb{I}/D & \mathbb{O} \end{bmatrix}, \\ &\mathbf{H}_3(x) = \begin{bmatrix} \mathbb{O} & -2(\nu-1)D\mathbf{I_2} \\ -\rho h \omega^2 \mathbb{I} + (1-\nu^2)D\mathbf{I_4} & \mathbb{O} \end{bmatrix}, \quad \mathbf{H}_4(x) = \begin{bmatrix} \mathbb{O} & \mathbb{I} \\ -\nu \mathbf{I_2} & \mathbb{O} \end{bmatrix}, \end{aligned} \tag{4.31}$$

where $\mathbb{I}$ is the $K \times K$ identity matrix and $\mathbb{O}$ is the $K \times K$ zero matrix.

4.3.1.5 Impedance matrix method

An impedance matrix $\mathbf{Z}(x)$ can be defined as

$$\begin{bmatrix} \mathbf{M_x}(x) \\ \mathbf{V_x}(x) \end{bmatrix} = -\mathrm{j}\omega\mathbf{Z}(x)\begin{bmatrix} \mathbf{w}(x) \\ \theta_\mathbf{x}(x) \end{bmatrix}. \tag{4.32}$$

Substituting Eq. (4.32) in Eq. (4.27), a Riccati non-linear equation is obtained for the impedance matrix [46, 57]:

$$\frac{\partial \mathbf{Z}(x)}{\partial x} = -\mathbf{Z}(x)\mathbf{H_1}(x) + \mathrm{j}\omega\mathbf{Z}(x)\mathbf{H_2}(x)\mathbf{Z}(x) - \frac{\mathbf{H_3}(x)}{\mathrm{j}\omega} + \mathbf{H_4}(x)\mathbf{Z}(x). \tag{4.33}$$

The boundary value problem is transformed in an initial value problem. The free boundary condition translates into the initial condition $\mathbf{Z}(x=0) = \mathbb{O}$. The numerical resolution of Eq. (4.33) is presented in Sec. 4.3.3.

4.3.1.6 Wave expansion of the state vector

Eigenspace of matrix $\mathbf{H}(x)$ is described by $4K$ eigenvalues and their associated eigenvectors. The relation between them is

$$\mathbf{E}(x)\mathbf{H}(x) = \mathbf{\Lambda}(x)\mathbf{E}(x), \tag{4.34}$$

where $\mathbf{\Lambda}(x)$ is the diagonal matrix containing the eigenvalues of $\mathbf{H}(x)$ on its diagonal and

$$\mathbf{E}(x) = \begin{bmatrix} \mathbf{E_1} & \mathbf{E_2} \\ \mathbf{E_3} & \mathbf{E_4} \end{bmatrix}, \tag{4.35}$$

with $\mathbf{E_1}$ to $\mathbf{E_4}$ being $2K \times 2K$ matrices, is a matrix whose columns are the associated eigenvectors; $\mathbf{E}$ is also the transition matrix between eigenspace and state space. The change of basis is applied using the relation

$$\mathbf{W}(x) = \mathbf{E}(x)\mathbf{V}(x), \tag{4.36}$$

where $\mathbf{V}(x)$ is the wave vector, describing for each mode k the propagating and attenuating waves travelling towards $x > 0$ and $x < 0$.

For the sake of simplicity, let us first assume a single transverse mode q verifying the dispersion equation

$$k_q^4(x) = -k_f^4(x) + \left(\frac{q\pi}{b}\right)^4. \tag{4.37}$$

Then the eigenvalue matrix $\mathbf{\Lambda}$ of $\mathbf{H}$ writes:

$$\mathbf{\Lambda} = \mathrm{diag}\left(-jk_{1q}, k_{2q}, jk_{1q}, -k_{2q}\right), \tag{4.38}$$

where

$$k_{1q} = \sqrt{k_f^2 - (q\pi/b)^2}, \tag{4.39}$$

$$k_{2q} = \sqrt{k_f^2 + (q\pi/b)^2}, \tag{4.40}$$

and where $k_f = \sqrt[4]{\omega^2 \rho h/D}$ is the flexural wave number. It can easily be shown that the eigenvalues verify the dispersion equation (4.37). In the absence of dissipation, second and fourth eigenvalues are real and are related to attenuating waves. Depending on the sign of $k_f^2 - (q\pi/b)^2$, first and third eigenvalues are real or imaginary and are related to effectively propagating waves ($k_f^2 - (q\pi/b)^2 > 0$) or evanescent waves ($k_f^2 - (q\pi/b)^2 < 0$). The sign of the eigenvalue indicates the travelling direction of the associated wave: from the chosen convention first and second eigenvalues are related to travelling waves towards $x < 0$ and third and fourth eigenvalues are related to travelling waves towards $x > 0$. When several transverse modes are considered, a similar classification is chosen, thus:

$$\mathbf{\Lambda} = \mathrm{diag}(\mathbf{p}-, \mathbf{a}-, \mathbf{p}+, \mathbf{a}+), \tag{4.41}$$

where **p** and **a** indicate a vector of eigenvalues related to *propagating* or *attenuating* waves, respectively, and the sign indicates the direction of travel of the associated waves. The wave vector is thus noted

$$\mathbf{V} = \begin{bmatrix} \mathbf{V}_p^- \\ \mathbf{V}_a^- \\ \mathbf{V}_p^+ \\ \mathbf{V}_a^+ \end{bmatrix}. \tag{4.42}$$

4.3.1.7 Reflection and scattering matrices

Let Ω be a region of a waveguide delimited by two abscissas t_- and t_+ (see Fig. 4.5). $\mathbf{V}_{out}$ and $\mathbf{V}_{in}$ are the outcoming wave vector from Ω and incoming wave vector to Ω, respectively. They write

$$\mathbf{V}_{out} = \begin{bmatrix} \mathbf{V}^-(t_-) \\ \mathbf{V}^+(t_+) \end{bmatrix} \quad \text{and} \quad \mathbf{V}_{in} = \begin{bmatrix} \mathbf{V}^-(t_+) \\ \mathbf{V}^+(t_-) \end{bmatrix}. \tag{4.43}$$

The scattering matrix **S** (size $4K \times 4K$) of Ω is defined by

$$\mathbf{V}_{out} = \mathbf{S}\mathbf{V}_{in}, \tag{4.44}$$

and writes

$$\mathbf{S} = \begin{bmatrix} \mathbf{T}^{+-} & \mathbf{R}^- \\ \mathbf{R}^+ & \mathbf{T}^{-+} \end{bmatrix}, \tag{4.45}$$

where matrix $\mathbf{R}^+$ (size $2K \times 2K$) represents the reflection of the incident waves at side t_+ (denoted $\mathbf{V}^-(t_+)$) on the reflected waves at side t_+ (denoted $\mathbf{V}^+(t_+)$). Matrix $\mathbf{T}^{+-}$ (size $2K \times 2K$) represents the transmission of the incident waves at side t_+ on the transmitted waves at side t_-. Matrix $\mathbf{R}^+$ writes:

$$\mathbf{R}^+ = \begin{bmatrix} \mathbf{R}_{pp}^+ & \mathbf{R}_{ap}^+ \\ \mathbf{R}_{pa}^+ & \mathbf{R}_{aa}^+ \end{bmatrix}, \tag{4.46}$$

where $\mathbf{R}_{ir}^+$ is the matrix of the coupling coefficient of incident i on reflected r propagating p or attenuating a waves. A diagonal term $(R_{ir}^+)_{qq}$ represents the reflection of a mode q on itself while an out-of-diagonal term $(R_{ir}^{+})_{kj}$ with $q \neq j$ represents the coupling between a mode q on a mode j. These notations are also applied to the other matrices embedded in $\mathbf{S}$ (Eq. (4.45)). For example, $(T_{pa}^{+-})_{13}$ describes the transmission of the incident propagating wave of mode 1 at side t_+ on the transmitted attenuating wave of the mode 3 at side t_-.

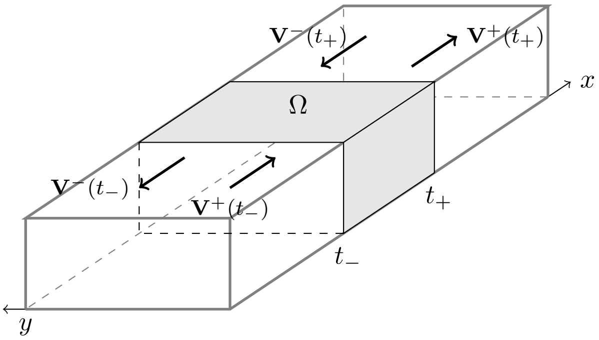

Figure 4.5: Region Ω of the waveguide delimited by $x = [t_-, t_+]$. Incoming and outgoing waves are represented.

4.3.1.8 Boundary condition at x=0

For any region of the waveguide defined by the abscissa x including the end of the waveguide at x=0, the scattering matrix $\mathbf{S}_{[0,x]}$ representing the waveguide free extremity is defined in agreement with the definition of Ref. [130]: transmission towards the surrounding medium $\mathbf{T}^{+-}$, transmission towards the inside $\mathbf{T}^{-+}$ and reflection of the outside $\mathbf{R}^-$ are zero. Only $\mathbf{R}^+$ is non-zero. Hence:

$$\mathbf{S}_{[0,x]} = \begin{bmatrix} \mathbb{O} & \mathbb{O} \\ \mathbf{R}^+(x) & \mathbb{O} \end{bmatrix}. \tag{4.47}$$

Matrix $\mathbf{R}^+(x)$ is then called the reflection matrix of the guide extremity (i.e. the region $[0\ x]$). Using Eqs. (4.34) and (4.32) yields the relation between $\mathbf{R}^+(x)$ and $\mathbf{Z}(x)$:

$$\mathbf{R}^+(x) = (\mathrm{j}\omega\mathbf{Z}(x)\mathbf{E}_2 + \mathbf{E}_4)^{-1}(-\mathbf{E}_3 - \mathrm{j}\omega\mathbf{Z}(x)\mathbf{E}_1). \tag{4.48}$$

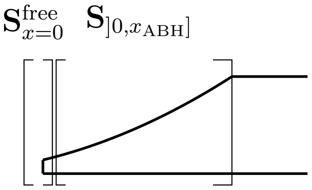

Figure 4.6: Boundary condition at $x = 0$ and region $]0, x_{\text{ABH}}]$. The assembly of the two region defines region $[0, x_{\text{ABH}}]$ (see Eq. (4.49)).

When x=0, $\mathbf{S}_{[0,x]}$ is the scattering matrix of the boundary condition $\mathbf{S}_{x=0}$. The relation between scattering matrix $\mathbf{S}_{[0,x]}$ of region *including* the boundary condition and scattering matrix $\mathbf{S}_{]0,x]}$ of region *excluding* the boundary condition is (see Fig. 4.6)

$$\mathbf{S}_{[0,x_{\text{ABH}}]} = \mathbf{S}_{x=0} * \mathbf{S}_{]0,x_{\text{ABH}}]}, \tag{4.49}$$

where the $\star$ assembly operator is defined in Appendix A.4.2. It is therefore important to distinguish $\mathbf{R}^{+}(x)$ and $\mathbf{R}^{+}{}_{]0,x]}$.

4.3.2 Model of an ABH imperfection

Identifying and modelling imperfections or defaults in a structure is closely related to structural health monitoring [39] where the main interest is usually cracks. Those are usually modelled by local stiffness changes [71]. A simpler model is used in this study: the imperfection is described as a material extension of small variable length $a(y)$ along direction x. It is constituted of infinitesimal rigid bars of width dy, that are not coupled between each other (see Fig. 4.7). These bars are supposed to follow the kinematics of the last cross section of the waveguide: this leads to the fact that the displacement $w(0,y)$ and slope $\theta_x(0,y)$ of the last cross section are the ones of the bars. These bars have a mass density ρ identical to that of the waveguide and their thickness h is assumed constant and equal to that of the extremity of the waveguide. The only actual parameter is then the length $a(y)$ which control for each infinitesimal element the force $V_x(0,y)$ and bending moment $M_x(0,y)$ exerted on the guide extremity. Finally, this simple model is well adapted to represent any arbitrary imperfection by a distribution of mechanical load at the extremity.

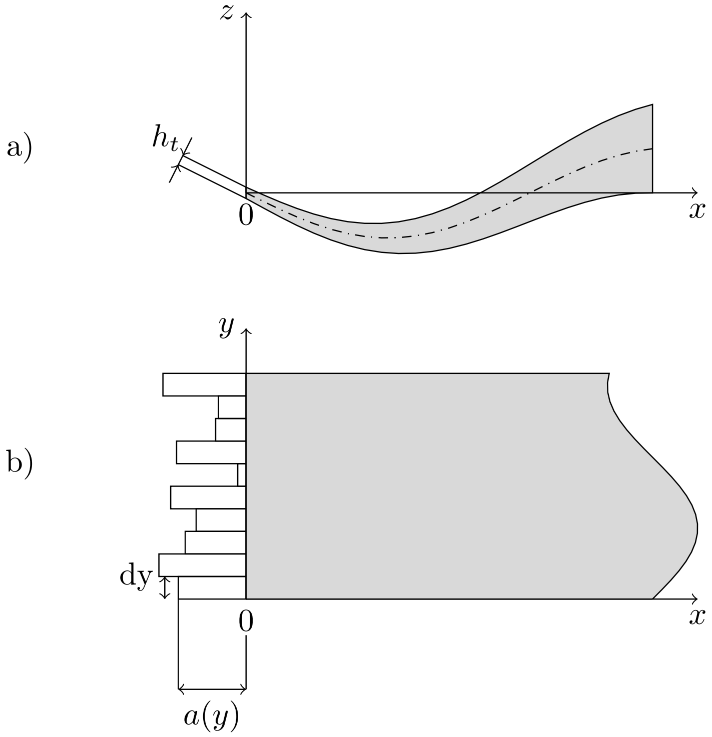

Figure 4.7: Model of imperfection as an extension constituted of infinitesimal rigid bars: (a) side view and (b) top view.

Newton's Second Law is applied to each element and leads to

$$\rho h a(y) \mathrm{d}y \ddot{z}(y) = -V_x(0, y), \tag{4.50}$$

$$I_0 \ddot{\theta}_x(0, y)_x = -M_x(0, y), \tag{4.51}$$

with $\rho h a(y)$ the mass of the element, assumed concentrated in its centre of mass, whose vertical displacement is $z(y) = w(0, y) + \frac{a(y)}{2}\theta_x(0, y)$. The moment of inertia I_0 writes:

$$I_0 = \int_0^{a(y)} s^2 \rho h \mathrm{d}y \, \mathrm{d}s = \frac{\rho h a(y)^3 \mathrm{d}y}{3}. \tag{4.52}$$

Eqs. (4.50) and (4.51) then write

$$V_x(0, y) = \rho h a(y) \mathrm{d}y \omega^2 (w + \frac{a\theta_x}{2}), \tag{4.53}$$

$$M_x(0, y) = \frac{\rho h a(y)^3 \mathrm{d}y}{3} \omega^2 \theta_x. \tag{4.54}$$

From the multimodal development of $w(y) = \sum\limits_{q=1}^{K} w_q \Psi_q(y)$ and $\theta_x(y) = \sum\limits_{q=1}^{K} \theta_q \Psi_q(y)$, the projection of Eqs. (4.50) and (4.51) on the transverse modes $\Psi_j(y)$ yields:

$$V_{xq} = \sum_{j=1}^{K} w_j \frac{\rho h \omega^2}{b} \int_0^b a(y) \Psi_q(y) \Psi_j(y) \, \mathrm{d}y + \sum_{j=1}^{K} \theta_j \frac{\rho h \omega^2}{2b} \int_0^b a(y)^2 \Psi_q(y) \Psi_j(y) \, \mathrm{d}y, \tag{4.55}$$

and

$$M_{xq} = \sum_{j=1}^{K} \theta_j \frac{\rho h \omega^2}{3b} \int_0^b a(y)^3 \Psi_q(y) \Psi_j(y) \, \mathrm{d}y. \tag{4.56}$$

From the impedance matrix definition of Eq. (4.32), the boundary condition at x=0 is expressed as an initial impedance condition:

$$\mathbf{Z}_0 = \frac{1}{-\mathrm{j}\omega} \begin{bmatrix} \mathbb{O} & \frac{\rho h \omega^2}{3b} \int_0^b a(y)^3 \Psi_q \Psi_j \, \mathrm{d}y \\ \frac{\rho h \omega^2}{b} \int_0^b a(y) \Psi_q \Psi_j \, \mathrm{d}y & \frac{\rho h \omega^2}{2b} \int_0^b a(y)^2 \Psi_q \Psi_j \, \mathrm{d}y \end{bmatrix}. \tag{4.57}$$

In the general case, matrix $\mathbf{Z}_0$ does not have a purely analytical expression. The reality of imperfections is complex but this model gives a simple way to represent it with a single parameter $a(y)$. This parameter has to be small in regards of the wavelength at x=0 for the model to be valid and the bars to respect the assumption of inflexibility. The couplings due to elementary imperfections can then be studied.

Because of $a(y)$ is supposed to be small, terms $\frac{\rho h \omega^2}{2b} \int_0^b a(y)^2 \Psi_q \Psi_j \, \mathrm{d}y$ and $\frac{\rho h \omega^2}{3b} \int_0^b a(y)^3 \Psi_q \Psi_j \, \mathrm{d}y$ can actually be neglected in regards of $\frac{\rho h \omega^2}{b} \int_0^b a(y) \Psi_q \Psi_j \, \mathrm{d}y$. The model of Eq. (4.57) is then simplified in the followings: the effects of rigid bars are restricted to their localised masses, therefore

$$\mathbf{Z}_0 = \frac{1}{-\mathrm{j}\omega} \begin{bmatrix} \mathbb{O} & \mathbb{O} \\ \frac{\omega^2}{b} \int_0^b m(y) \Psi_q \Psi_j \, \mathrm{d}y & \mathbb{O} \end{bmatrix}, \tag{4.58}$$

with $m(y) = \rho h a(y)$.

4.3.3 Numerical resolution

4.3.3.1 Magnus method

The Riccati equation (4.33) can be solved numerically for example using a Runge-Kutta scheme or a Magnus scheme [105, 118, 88]. A Magnus scheme is chosen here, because it allows to "jump" the singularities in the impedance matrix [105] and because it is shown to be more efficient than the Runge-Kutta scheme used in [57]. This numerical scheme can also be used for computing the scattering matrix of a section. A fourth-order Magnus scheme is used. The waveguide is discretized along the x-direction with a constant step. The Magnus scheme is applied to Eq. (4.27) and yields:

$$\mathbf{W}(\bar{x}_{n+1}) = e^{\mathbf{\Omega_n}}\mathbf{W}(\bar{x}_n), \tag{4.59}$$

where $\bar{x}_n$ is the longitudinal discrete coordinate and Ω_n is the fourth-order Magnus matrix [66]:

$$\mathbf{\Omega_n} = \frac{\Delta}{2}(\mathbf{H}_1 + \mathbf{H}_2) + \frac{\sqrt{3}}{12}\Delta^2[\mathbf{H}_2, \mathbf{H}_1], \tag{4.60}$$

where $\Delta = \bar{x}_{n+1} - \bar{x}_n$ is the constant spatial step,

$$\mathbf{H}_1 = \mathbf{H}(\bar{x}_n + \left(\frac{1}{2} - \frac{\sqrt{3}}{6}\right)\Delta), \tag{4.61}$$

$$\mathbf{H}_2 = \mathbf{H}(\bar{x}_n + \left(\frac{1}{2} + \frac{\sqrt{3}}{6}\right)\Delta), \tag{4.62}$$

and $[\mathbf{H}_2, \mathbf{H}_1]$ is the commutator between $\mathbf{H}_2$ and $\mathbf{H}_1$. Besides, the following notation is used for the exponential propagator:

$$e^{\mathbf{\Omega_n}} = \begin{bmatrix} \mathbf{O}_1 & \mathbf{O}_2 \\ \mathbf{O}_3 & \mathbf{O}_4 \end{bmatrix}, \tag{4.63}$$

where $\mathbf{O}_1$ to $\mathbf{O}_4$ are $2N \times 2N$ matrices.

From Eq. (4.59), an iterative scheme for the impedance matrix $\mathbf{Z}$ can be built:

$$\mathbf{Z}(\bar{x}_{n+1}) = \frac{1}{-\mathrm{j}\omega}[\mathbf{O_3} - \mathbf{O_4}\mathrm{j}\omega\mathbf{Z}(\bar{x}_n)][\mathbf{O_1} - \mathbf{O_2}\mathrm{j}\omega\mathbf{Z}(\bar{x}_n)]^{-1}. \tag{4.64}$$

Such an iterative scheme allows us to compute $\mathbf{Z}(\bar{x}_n)$ for all values of x_n since $\mathbf{Z}$ is imposed at $x = 0$.

4.3.3.2 Computation of the elementary scattering matrix from Magnus scheme

The scattering matrix $\mathbf{S}_{\text{elem}}$ of an elementary section of length Δ is obtained from Magnus scheme. Combining Eq. (4.59) and Eq. (4.36) gives

$$\mathbf{V}_{\bar{x}_{n+1}} = \mathbf{E}_{\bar{x}_{n+1}}^{-1}e^{\mathbf{\Omega_n}}\mathbf{E}_{\bar{x}_n}\mathbf{V}_{\bar{x}_n}. \tag{4.65}$$

The local transfer matrix $\mathbf{T}$ is identified in Eq. (4.65):

$$\mathbf{T} = \mathbf{E}_{\bar{x}_{n+1}}^{-1} e^{\mathbf{\Omega_n}} \mathbf{E}_{\bar{x}_n} = \begin{bmatrix} \mathbf{T_1} & \mathbf{T_2} \\ \mathbf{T_3} & \mathbf{T_4} \end{bmatrix}. \tag{4.66}$$

Rewriting $\mathbf{V}_{\bar{x}_{n+1}}$ and $\mathbf{V}_{\bar{x}_n}$ in $\mathbf{V}_{out}$ and $\mathbf{V}_{in}$ (referring to the elementary section) allows to reorganize matrix $\mathbf{T}$ in order to obtain the scattering matrix $\mathbf{S}_{\text{elem}}$ of the elementary section:

$$\mathbf{S}_{\text{elem}} = \begin{bmatrix} \mathbf{T_1}^{-1} & -\mathbf{T_1}^{-1}\mathbf{T_2} \\ \mathbf{T_3}\mathbf{T_1}^{-1} & \mathbf{T_4} - \mathbf{T_3}\mathbf{T_1}^{-1}\mathbf{T_2} \end{bmatrix}. \tag{4.67}$$

It can be noticed that, by construction, if transition matrices $\mathbf{E}_{\bar{x}_n}$ are $\mathbf{E}_{\bar{x}_{n+1}}$ are identical (in the case of an homogeneous waveguide), matrix $\mathbf{S}_{\text{elem}}$ is assimilated to the wave propagator between these two abscissas: matrix $\mathbf{S}_{\text{elem}}$ is then diagonal. The $\star$ operator defined in Appendix A.4.2 allows the combination of the numerically computed elementary scattering matrices in order to compute $\mathbf{S}_{]0x]}$ (Sec. 4.4.4) or $\mathbf{S}_{[0x]}$ (Sec. 4.4.2).

4.3.3.3 Convergence of the numerical solution

The convergence of the proposed numerical solution is verified by computing the coefficient $(R_{pp}^{+})_{11}$, first diagonal term of matrix $\mathbf{R}^{+}$ of Eq. (4.45). This coefficient represents the reflection of the propagating transverse mode 1 on itself: on the 400–2000 Hz range, only transverse mode 1 is propagating in the uniform region of the waveguide, therefore $(R_{pp}^{+})_{11}$ is a practical indicator of the ABH effect in this range. The mean error ε on the $[f_{min}, f_{max}]$ range

$$\varepsilon = \frac{1}{f_{max} - f_{min}} \int_{f_{min}}^{f_{max}} \frac{|R_K(f) - R_{K=60}(f)|^2}{|R_{K=60}(f)|^2} \, \mathrm{d}f, \tag{4.68}$$

is considered, where $R_K = (R_{pp}^{+})_{11}$ evaluated at $x = l_{\text{ABH}}$ with K transverse modes and $R_{K=60} = (R_{pp}^{+})_{11}$ evaluated at $x = l_{\text{ABH}}$ with a high number of modes (K=60) for which the numerical solution has converged. For the imperfect non covered ABH case defined in Sec. 4.4.1, Fig. 4.8(a) shows the evolution of $(R_{pp}^{+})_{11}$ with frequency, computed with the spatial step $\Delta = 10^{-4}$ m, and Fig. 4.8(b) shows the evolution of error ε with the number of transverse modes taken into account in the calculation, on the 400–2000 Hz range. The convergence is slow (slope is -0.41) and the error is high but this is explained by the high number of propagating modes at the tip of the profile (N_{propa}=29 at 2000 Hz) and the evolution of $(R_{pp}^{+})_{11}$ with frequency presenting several deep minima. Nevertheless, the result is satisfying and results of Sec. 4.4 are obtained using K=30 modes. Other aspects of the validation of the numerical solution, including comparison to FEM solution for homogeneous and inhomogeneous waveguides and effect of the spatial step Δ can be found in Appendix A.4.

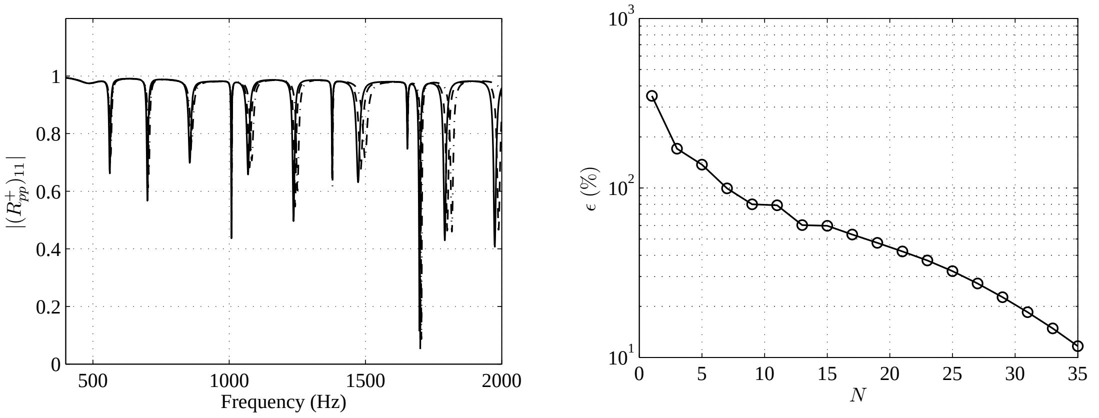

(a) (b)

Figure 4.8: (a) Evolution of coefficient $(R^+_{pp})_{11}$ with frequency for K=19 (dashdotted), K=29 (dashed) and K=60 (full), and (b) evolution of the error ε on coefficient $(R^+_{pp})_{11}$ with the number of mode K.

4.4 Scattering induced by imperfections

4.4.1 Characteristics of the simulated waveguide

The case of an ABH waveguide made of aluminium is considered. Parameters used in the numerical applications of the model are summarized in Tab. 4.1; parameters for the damping layer are realistic but do not result from characterization tests. Moreover, as a first step the imperfection is modelled by a single mass localised at $(x = 0, y_0 = b/2)$. This mass localisation induces that only waveguide modes with odd numbers are concerned with possible coupling. The initial condition (4.57) then simplifies:

$$\mathbf{Z}_0 = \frac{\mathrm{j}m_0\omega}{b}\begin{bmatrix} \mathbb{O} & \mathbb{O} \\ \Psi_j(y_0)\Psi_k(y_0) & \mathbb{O} \end{bmatrix}. \tag{4.69}$$

In this configuration, mode 1 is propagating above 360 Hz in the homogeneous region (this is assessed further in Sec. 4.4.3) and the next odd mode is mode 3 which is propagating above 2000 Hz. Therefore, numerical results are shown in the 400–2000 Hz frequency range.

4.4.2 Typical results for the reflection coefficient

Fig. 4.9 presents variations of reflection coefficient $(R^+_{pp})_{11}$ (of incident mode 1 on reflected mode 1) with frequency, for terminations described in Tab. 4.1 with or without imperfection. The reflection on the ABH extremity without imperfection and without damping layer (full gray line) is close to unity. This is not surprising since the non covered ABH is known to be inefficient. Covered ABH without imperfection (dashed gray line)

Geometrical characteristics	Characteristics of material
Aluminium plate	
L=0.8 m, b=0.1 m, l_{ABH}=0.06 m, l_t=0.07 m, h_0=1.5 mm, m=2.	E_1=70 GPa, η_1=0.2 %, ρ_1=2700 kg.m^{-3}, ν=0.3.
Damping layer	
h_l=0.1 mm, d=0.05 m.	E_2=7 GPa, η_2=20 %, ρ_2=1000 kg.m^{-3}.
Imperfection	
y_0=0.05 m	m_0=1.5× 10^{-3} kg

Table 4.1: Geometrical and material characteristics of the simulated ABH waveguide.

gives an interesting result as its reflection coefficient can be as low as 0.5 with oscillations; this results can be compared to earlier results [57].

The case of the non covered but imperfect ABH termination (single mass at the centre of the cross-section, full black line) is mostly identical to the perfect termination except that it displays several very deep minima localised in frequency. By adding a damping layer on the imperfect termination (dashed black line), $|(R^+_{pp})_{11}|$ is clearly lower than the perfect covered case; the difference can be as much as 0.1. Notice than local minima seen on the non-covered imperfect extremity can still be observed in the covered case but are much less localised in frequency.

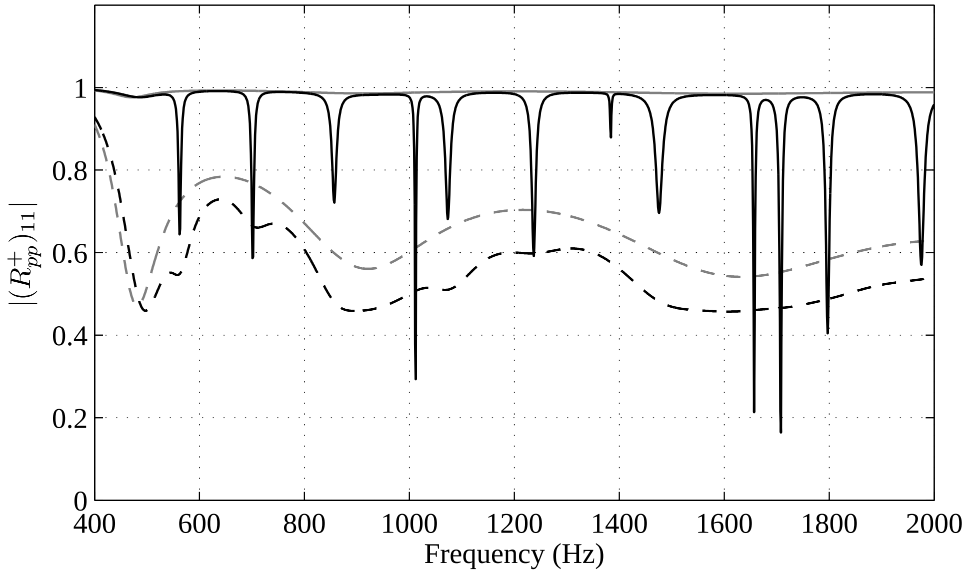

Figure 4.9: Modulus of the reflection coefficient $(R^+_{pp})_{11}$ for perfect non covered (full gray line), perfect covered (dashed gray line), imperfect non covered (full black line) and imperfect covered (full dashed line) ABH terminations (parameters of Tab. 4.1).

4.4.3 Cut-off frequency

In an homogeneous structure of a given thickness, whether a mode q is propagating or not only depends on the frequency according to the dispersion relation for mode q (see Eq. (4.37)). In an inhomogeneous structure such as the tapered profile studied here (see Fig. 4.10(a)), the propagating behaviour depends on both the frequency and the abscissa.

At a given frequency, it is shown on Fig. 4.10(b) that the eigenvalues (i.e. constants of propagation) associated with propagating waves of modes q=1, 3, 5, 7 (for example) are functions of abscissa (see Eq.(4.37)). The abscissa at which the real part of the eigenvalue becomes zero and the imaginary part takes a non-zero value indicates the cut-off abscissa, where the mode becomes propagating. These cut-off abscissas allow for each mode q to define coloured region on Fig. 4.10(a). Fig. 4.10(c) shows that the cut-off frequency of mode q depends on the abscissa, i.e. on the local thickness of the waveguide. In this case, in the uniform region of the waveguide mode 1 is propagating above 360 Hz while modes 3, 5 and 7 are not. They are thus confined in the tapered extremity.

Note that the number of propagating modes at a given abscissa depends on the flexural wavenumber therefore on the bending stiffness. The simplified RKU model used in Eq. (4.13) does not modify the real part of the bending stiffness, which is a reasonable approximation when the thickness of the damping layer is much smaller than the structure thickness. When the thicknesses are in the same range, both real and imaginary parts of the bending stiffness are modified and the damping layer can actually stiffens the structure. A consequence is that there are less propagating modes at a given abscissa.

4.4.4 Reflection induced by the tapered profile itself

The geometrical acoustics analysis [93], which is based on the WKB approximation and only considers propagating waves, suggests that an incident wave reflects only at the boundary and that there is no reflection inside the tapered profile. The model given in Sec. 4.3 allows to observe the reflection, or more generally the scattering, in a region $]0, x_{\text{ABH}}]$ of the waveguide that does not include the free boundary condition. Zero reflection implies that the scattering matrix is diagonal: it contains only transmission terms and reflection terms are zero. Scattering matrices $\mathbf{S}_{]0,x]}$ and $\mathbf{S}_{[0,x]}$ are computed with respect to frequency and allow to observe the reflection of the ABH profile only or the reflection of the ABH profile with the free condition, respectively.

Fig. 4.11 shows indeed that for mode 1, there is a non zero reflection along the tapered profile that does not depend on the free boundary condition: the tapered section reflects a low part of incident waves and transmits the rest (full gray line). Note that covering the profile with a damping layer does not affect much this behaviour (full black line). The observed reflection coefficient displays oscillations that can directly be compared to oscillations in the full ABH termination (i.e. including the boundary condition, dashed black line). Oscillations of the reflection coefficient have been observed first in [57], where the authors emit the hypothesis that oscillations are due to sharpness and length of the

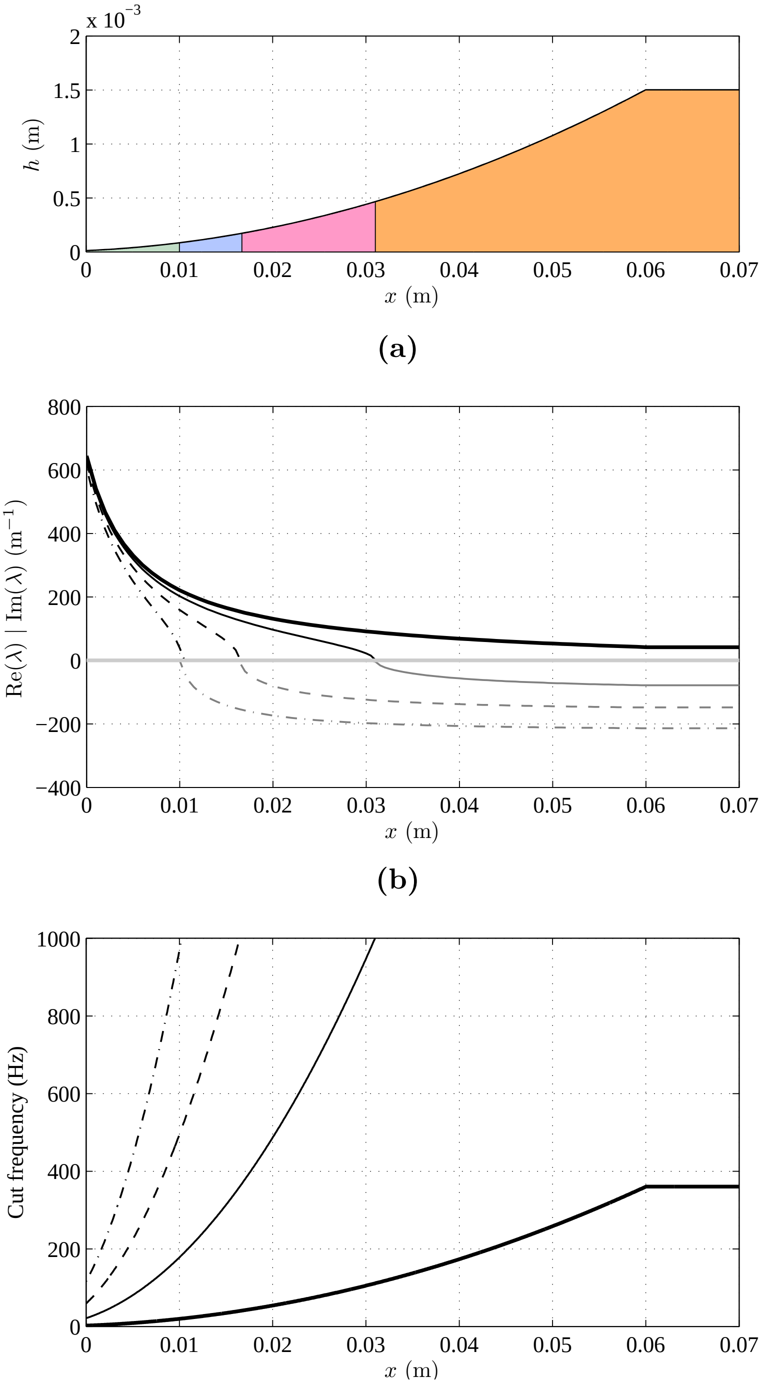

(a)

(b)

(c)

Figure 4.10: (a) Thickness profile of the extremity with zone of propagation of modes k<3 (orange), k<5 (pink), k<7 (blue) and k>7 (green) at 1000 Hz. (b) Real (grey) and imaginary (black) parts of λ_1 (thick full), λ_3 (thin full), λ_5 (dashed) and λ_7 (dashdotted) at 1000 Hz. (c) Cut-off frequency for mode 1 (thick full), 3 (thin full), 5 (dashed), 7 (dashdotted).

profile. Note that the geometrical acoustics approach and the associated WKB solution [93, 77] does not yield oscillations; therefore, it may indicate that the approximations made in this approach are not valid, especially the approximation of sufficient smoothness. This is also recently suggested in a study of Feurtado *et al.* [49] who study the parameters yielding a smooth profile, but was also briefly discussed in Ref. [77].

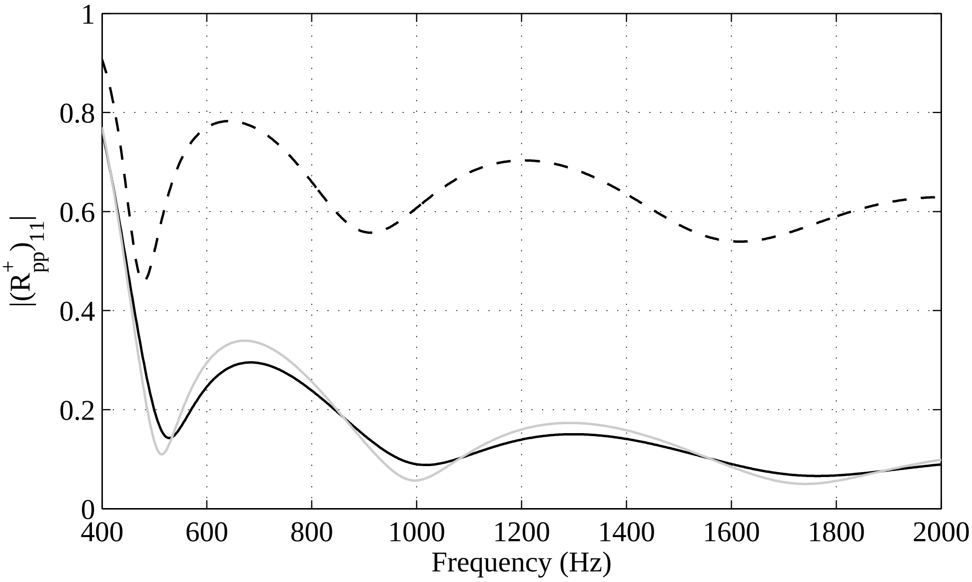

Figure 4.11: Modulus of the term $(1,1)$ of the reflection matrix $\mathbf{R}^+_{]0,x_{\mathrm{ABH}}]}$ with damping layer (full black), without damping layer (full grey) and of the reflection matrix $\mathbf{R}^+(x)$ with damping layer (dashed black).

4.4.5 Coupling mechanisms and mode trapping

Let us consider a propagating incident wave q arriving at the extremity. The reflection matrix $\mathbf{R}^+_{pp}$ at $x{=}0$ (submatrix of $\mathbf{S}_{x=0}$) is displayed on Fig. 4.12(a). It shows the mode coupling at the imperfect free end: on the one hand, diagonal terms of $|\mathbf{R}^+_{pp}|$ are less than unity. On the other hand, some out-of-diagonal terms are non-zero. The incident energy is thus redistributed on modes that are propagating at the extremity. This phenomenon is present at any frequency. The case of a single mass located in the centre of the extremity induces that only odd modes are concerned with couplings, as expected. Note that $|(\mathbf{R}^+_{pp})_{qj}|$ $(q \neq j)$ is close but not equal to $|(\mathbf{R}^+_{pp})_{jq}|$. It means that an incident mode q is partially reflected on mode j, but also that incident mode j is partially reflected on mode q.

Let us now consider a reflected wave j resulting from the redistribution (or scattering) described above. The wave is coming from the edge and its interaction with the propagating medium is described by the reflection matrix $\mathbf{R}^-_{pp}$ associated to scattering matrix $\mathbf{S}_{]0,x]}$. The reflection matrix $\mathbf{R}^-_{pp}$ is diagonal. Fig. 4.12(b) shows diagonal terms of matrix $\mathbf{R}^-_{pp}$, corresponding to reflection of modes q on themselves. The energy coming

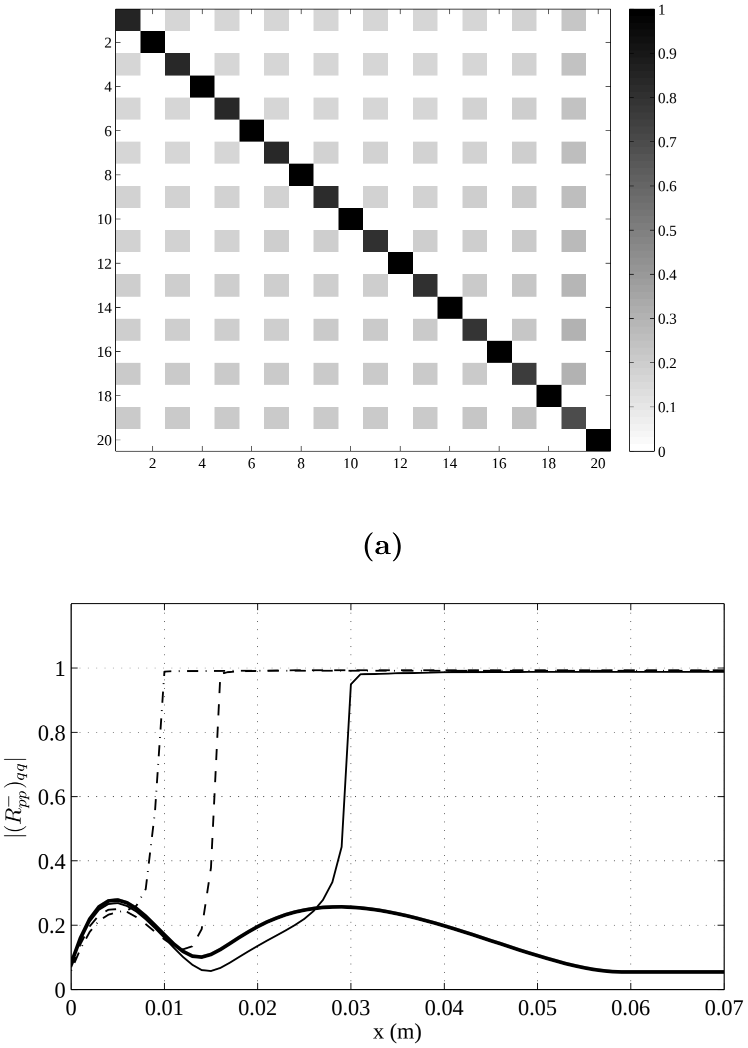

(a)

(b)

Figure 4.12: (a) Reflection matrix $|\mathbf{R}_{pp}^{+}|$ at point x=0 and for f=1000 Hz and (b) Third (full), fifth (dashed) and seventh (dashdotted) diagonal terms of the reflection matrix $|\mathbf{R}_{pp}^{-}|$ of the region $]0,x]$ at f=1000 Hz.

from the extremity toward the uniform part of the waveguide is fully reflected at some point in the tapered zone. The full reflection is indicated by a coefficient equal to 1 in modulus. The point at which there is full reflection corresponds to the cut-off abscissa shown on Fig. 4.10(b). A mode j excited by the imperfection at x=0 can then be reflected *toward the extremity* x=0 at some point in the tapered profile. A scheme for the proposed excitation and reflection mechanisms is displayed on Fig. 4.13.

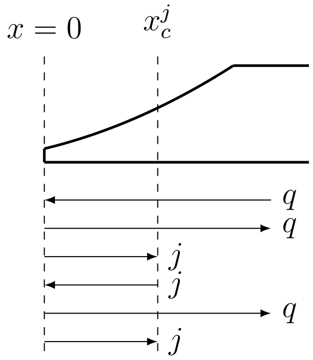

Figure 4.13: Scheme of the excitation and reflection mechanisms in the imperfect ABH termination. x_c^j indicates the cut-off abscissa for mode j.

Waves of a given mode then travel between the extremity and the cut abscissa of this mode, indicating the possibility of local resonances (on this topic, Krylov [76] mentions the ray turning point of a mode). Minima appearing at precise frequencies are shown on Fig. 4.9 for the imperfect case if it is not covered with a damping layer. It suggests that only at these frequencies the energy is trapped and that there exist local resonances responsible for the drop in the reflection coefficient.

4.4.6 Effect of the imperfection parameters

4.4.6.1 Effect of the position of the imperfection

Let us consider the same mass figuring the imperfection at two more positions: y_0=$b/3$ and y_0=$4b/5$. Reflection matrices for these cases are plotted on Fig. 4.14 and show the couplings between modes; note the slight differences compared to Fig. 4.12(a). Fig. 4.15 shows the results for $|(R_{pp}^{+})_{11}|$ in these configurations. In the case of the non covered tapered profile, reflection coefficients for $b/2$ and $b/3$ are fairly different as they do not display the same minima: this can be expected since they do not couple the same modes. When the termination is covered, the three cases are rather similar (see Fig. 4.16). It is however noticeable, that the best performance is reached when y_0=$b/2$, which is the position of maximum displacement for mode 1. Otherwise, the position does not have a significant impact.

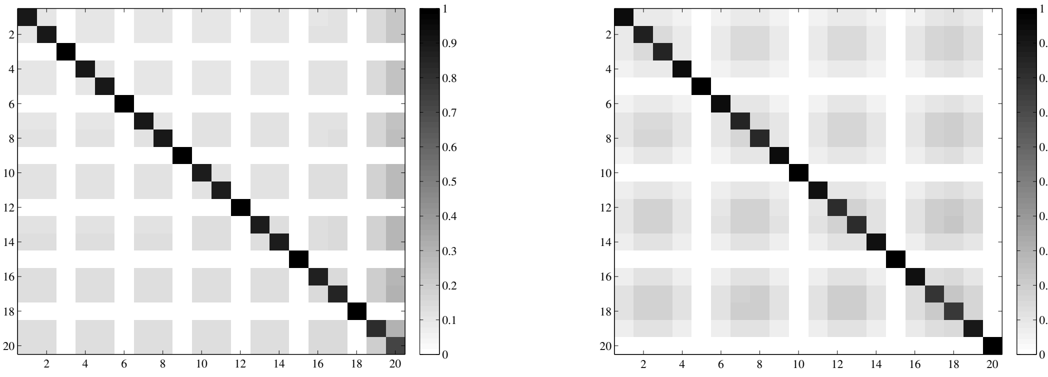

(a) **(b)**

Figure 4.14: Reflection matrices $\mathbf{R}_{pp}^{+}$ at x=0, 1000 Hz for masses located in (a) y=b/2 and (b) y=4b/5.

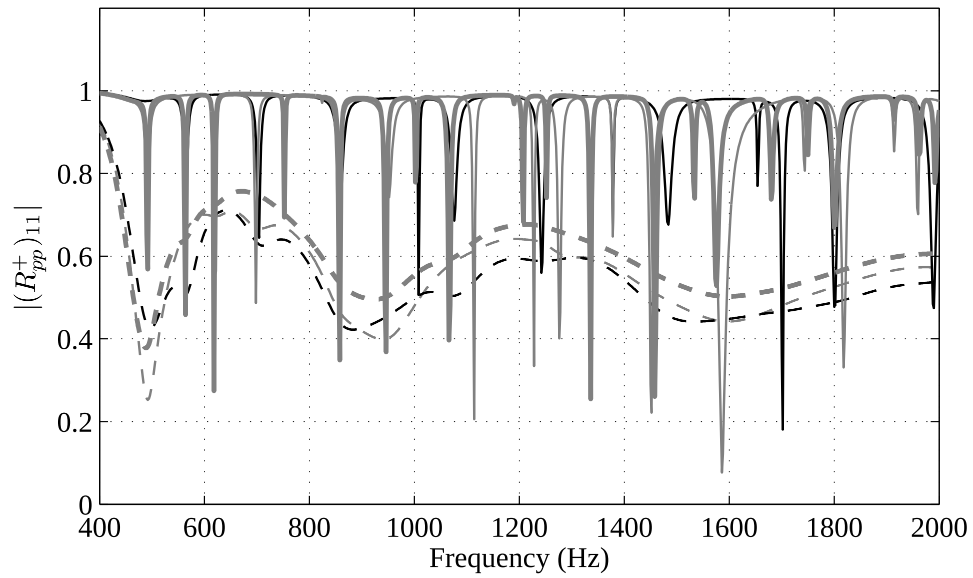

Figure 4.15: Modulus of the reflection coefficient $(R_{pp}^{+})_{11}$ for imperfect cases of ABH termination with mass at y=b/2 (black), y=b/3 (thin grey) and y=4b/5 (thick grey), non covered (full lines) and covered (dashed lines).

4.4.6.2 Effect of the number of imperfections

Fig. 4.16 presents results on $|(R^+_{pp})_{11}|$ for combined imperfections. Combination $b/2 + b/3$ and $b/2 + b/3 + 4b/5$ are studied. Note that theses configurations combines the minima of cases studied in Sec. 4.4.6.1. Cancellation of mutual effect may appear at some frequencies when the termination is not covered. Broad drops of $|(R^+_{pp})_{11}|$ appears (at 1600 Hz) that are the consequence of two close consecutive minima. In the covered case, combining imperfections seems beneficial for the reflection coefficient which is reduced in the 500–700, 900–1100 and 1400–2000 Hz ranges when masses are added to the model. The gain reaches 0.2 at some frequencies. Compared to Sec. 4.4.6.1, it appears that multiplying the imperfections helps obtaining a significant reduction of $|(R^+_{pp})_{11}|$, assuming that there is not cancellation effects. This fact suggests the use of controlled irregularities of the ABH extremity in order to enhance its damping performance.

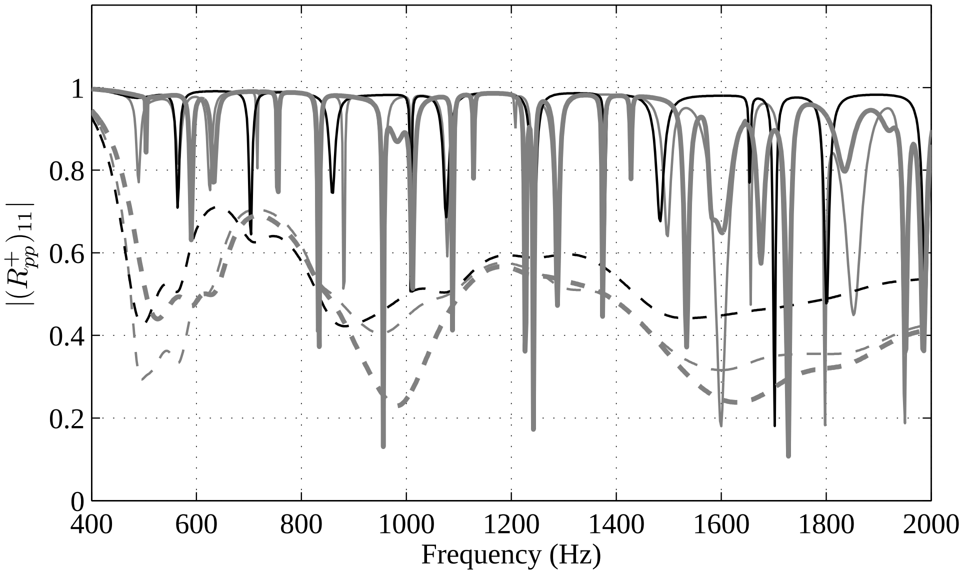

Figure 4.16: Modulus of the reflection coefficient $(R^+_{pp})_{11}$ for imperfect cases of ABH termination with mass at $y=b/2$ (black), $y=[b/2;b/3]$ (thin grey) and $y=[b/2;b/3;4b/5]$ (thick grey), non covered (full lines) and covered (dashed lines).

4.5 Interests of an imperfect termination on ABH beams

4.5.1 Effects of imperfection on loss factors of ABH plate

In Sec. 4.4, the effect of an elementary imperfection at the tip of the tapered profile has been investigated. Numerical computation of the reflection coefficient of the first transverse mode of an ABH waveguide shows a positive effect of the imperfection since

Table 4.2: Frequencies and modal loss factors for non-damaged and damaged case.

f (Hz)	566	850	1220	1696
$\eta_{\text{non damaged}}$ (%)	2.3	2.9	2.3	2.9
η_{damaged} (%)	3.1	3.5	3.4	3.1
Gain (%)	34	20	47	7

$|R|$ is decreased. The waveguide model developed in this analysis also allows to compute the response to a given excitation force, thus a mobility transfer function of the plate; it is then possible to estimate the modal loss factors in a given frequency band. Mobility transfer functions are given in Fig. 4.17. Computations are made with the parameters of Tab. 4.1). The loss factor of four resonance peaks are calculated by the half-power method for the perfect ABH plate and for the imperfect ABH plate, both covered with a damping layer. The results are shown in Tab. 4.2. The additional gain due to the imperfection appears to be irregular, ranging from 6 to 47 %. This increase of modal loss factor is actually quite small compared to the original ABH effect; nevertheless it is not negligible.

It is interesting to observe the imperfect non covered structure on Fig. 4.17 and see that the localised mass modifies the modal characteristics of the structure: It doubles most of the resonances peaks. This is due to eigenmodes splitting because the localised mass creates an asymmetry in the structure [79].

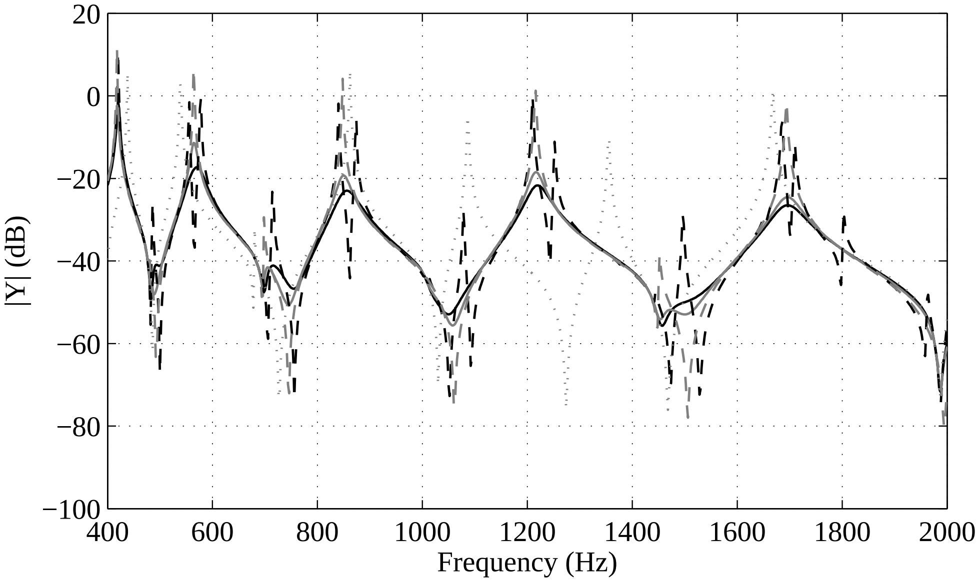

Figure 4.17: Mobility transfer function of homogeneous plate (dotted), ABH plate (dashed grey), ABH plate with damping layer (full grey), imperfect ABH plate (dashed black) and imperfect ABH plate with damping layer (full black).

4.5.2 Combined effect of imperfection and damping layer stiffness

Sec. 4.4 studied an imperfect termination taking into account a simplified model of extensional damping due to the damping layer. As reminded in Sec. 3.2.4, the damping layer can have a considerable effect on the local stiffness, therefore, a thick damping layer modifies the stiffness and reduce the number of propagating transverse modes. Fig. 4.18 shows the reflection coefficient calculated for a single imperfection located in $y{=}b/2$ for the extensional damping model of Eq. (3.2):

$$D(x) = \begin{cases} D_p(x) = \dfrac{E_p h_p(x)^3}{12(1-\nu^2)}(1+\mathrm{j}\eta_p), & \forall x > x_l \\ D_p(x)\Big[(1+\mathrm{j}\eta_p) + \frac{E_l}{E_p}\left(\dfrac{h_l}{h_p(x)}\right)^3(1+\mathrm{j}\eta_l) & \\ +\dfrac{3\left(1+\frac{h_l}{h_p(x)}\right)^2 + \frac{E_l h_l}{E_p h_p(x)}(1-\eta_p\eta_l + \mathrm{j}(\eta_p+\eta_l))}{1+\frac{E_l h_l}{E_p h_p(x)}(1+\mathrm{j}\eta_l)}\Big], & \forall x \leq x_l, \end{cases} \tag{3.2 revisited}$$

which also modifies the mass density (see Eq. (3.3)):

$$\rho(x) = \begin{cases} \rho_p, & \forall x > x_l \\ \dfrac{\rho_p h_p(x) + \rho_l h_l}{h_p(x)+h_l}, & \forall x \leq x_l, \end{cases} \tag{3.3 revisited}$$

The model of Eqs. (3.2) and (3.3) has fewer propagating modes than the model of Eq. (4.13), all things being equal. Nevertheless, the imperfection has a more important effect, compared to Fig. 4.9, indicating that the loss factor compensates the fewer local modes excited by the imperfection. Therefore, in a practical case where the damping layer stiffens the structure, even if there are few local modes, tip imperfections should still have a positive effect.

4.5.3 Imperfections on ABH beam

Clearly, the drop in $|R|$ or the increase of the modal loss factors is linked to the number of guide modes that are excited by the tip irregularities. It makes little sense to use the waveguide model with a beam width in order to estimate the potential gain for a beam because it sends the first resonance at high frequencies. However the numerical model of Chap. 3 can be modified in order to compute transfer mobility functions or eigenvalues for a beam with a tip imperfection similar to the one used in the waveguide model: the mass matrix of Eq. (3.18) is modified in order to embed a point mass:

$$\mathbf{M}' = \mathbf{M} + \mathbf{m}_0 \tag{4.70}$$

where $\mathbf{M}'$ is the modified mass matrix and $\mathbf{m}_0$ is the mass matrix of the point mass defined by

$$(\mathbf{m}_0)_{n,q} = \begin{cases} 0 & \forall n \neq n_0 \text{ and } \forall q \neq q_0 \\ \frac{m_0}{\Delta_{\tilde{x}}\Delta_y} & \text{if } (n,q) = (n_0,q_0) \end{cases}. \tag{4.71}$$

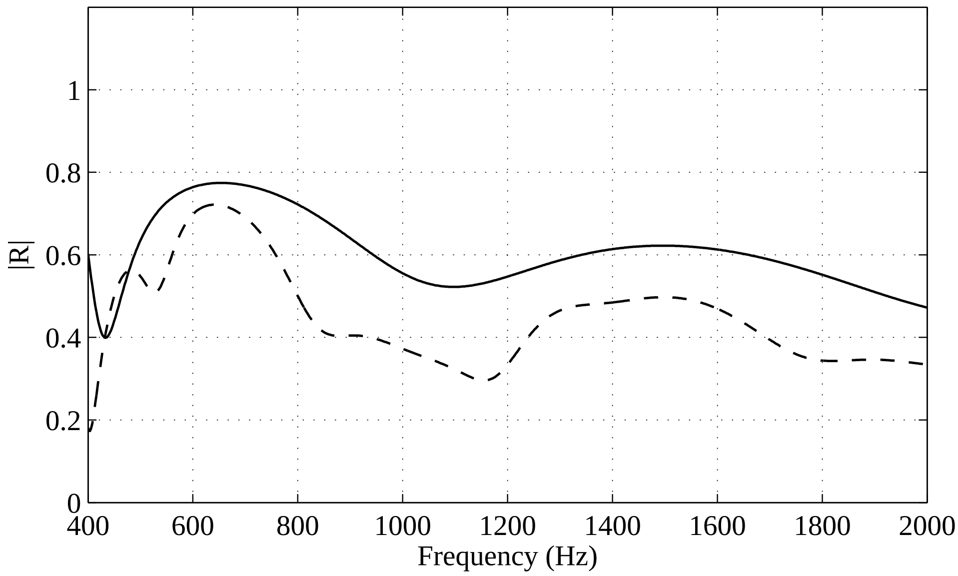

Figure 4.18: Reflection coefficient for a ABH extremity without imperfection (full) and with a imperfection at y=$b/2$ using the extensional damping model of Eq. (3.2) (dashed).

Fig. 4.19(a) shows the results in terms of eigenvalues of the modified finite-difference model for a mass m_0=1.5×10^{-5} kg and the parameters of Tab. 3.1. Fig. 4.19(b) displays the loss factors for the two cases. The effect is small but noticeable: the eigenvalue spectrum displays a slight increase of the loss angle, leading to the small increase of modal loss factors. Globally, the relative gains in the case of a covered ABH beam are rather poor but also irregular (as it is shown in Sec. 4.5.1 for the ABH plate). Nevertheless, the results suggest that a locally wider and thinner beam with irregularities could be more efficient.

4.6 Conclusions

This chapter investigates the role of imperfections that are usually found at the tip of the tapered profile when it is made very thin, due to the limitations of the manufacturing techniques. The raised points are the followings:

- A measurement of the reflection coefficient of an artificially damaged ABH extremity is realised and shows that it differs from the reflection coefficient of a non damaged extremity.
- In order to explain the experimental result, a multimodal model of inhomogeneous waveguide with an ABH termination with a simple imperfection is developed. The model allows to obtain the impedance matrix at any point, the scattering matrix of a region of the waveguide and the reflection matrix of the ABH extremity. It is numerically solved using a Magnus scheme.

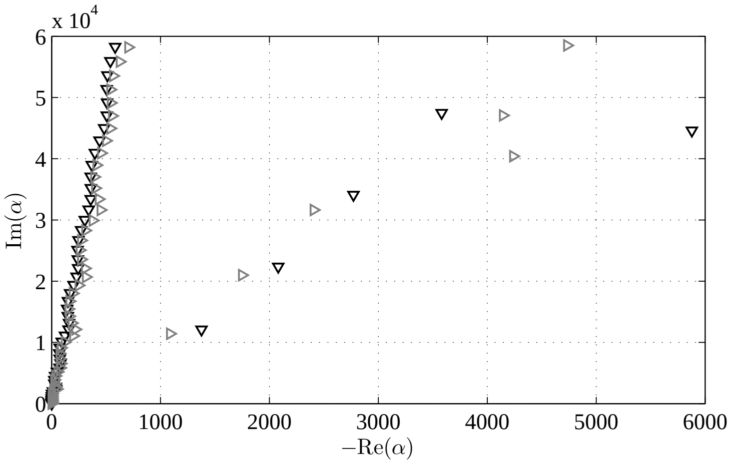

(a)

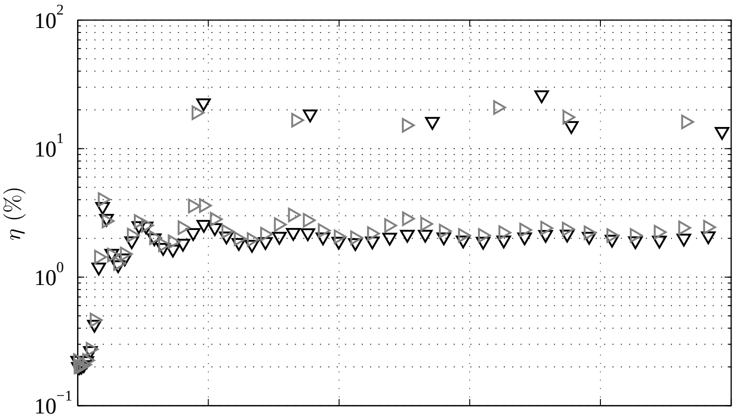

(b)

Figure 4.19: (a) Eigenvalue spectrum and (b) modal loss factors for ABH beam made of aluminium without (black, ▽) and with imperfection (grey, ▷).

- A elementary imperfection on the free extremity of the tapered profile affects the reflection coefficient and reduce it. Effects are localised in frequency when the damping is weak, but are broadly extended when the damping is increased due to the viscoelastic layer.
- At a given frequency, waveguide modes can be propagating in the tapered region while they are not in the thicker uniform region of the waveguide. They are thus confined.
- Due to couplings at the extremity, an incident waveguide mode is partially reflected on multiple modes. The imperfection then allows the excitation of guide modes that are confined in the ABH, leaving the possibility of local resonances that can explain the drop of the reflection coefficient for the incident mode.
- Furthermore, the results suggests the use of controlled imperfection of the tip of the ABH profile in order to enhance its damping performance.
- Finally, it is also shown that waves may be reflected inside the tapered profile itself and not only by the extremity.

Chapter 5

CONCLUSION

5.1 Performances of the ABH treatment for vibration damping

5.1.1 Summary of ABH characteristics

We can summarise the main features of the ABH termination on Fig. 5.1. Results obtained by modal and the wave approaches, including experimental and simulated results, are presented and provide a sort of identity card of the ABH effect. Fig. 5.1(a) reminds that the main effect of ABH on a beam the reduction of its resonant behaviour. It is interpreted on Fig. 5.1(b) as an increase of the loss angle of the complex eigenvalues of the structure, because of the repartition of eigenmodes energy in a highly damped region. Moreover, adding irregularity to the tapered extremity allows a slight additional increase of this loss angle, hence a enhancement of the performance. The inhomogeneous damping properties translate into wave propagation phenomena that are observed on Fig. 5.1(c): a propagating wave pattern is noticeable. It is interpreted as a huge drop in the reflection coefficient, as illustrated on Fig. 5.1(d) by the numerical model proposed in Chap. 4. As in the case of Fig. 5.1(b), the effect of irregularities is seen as an additional drop in $|R|$. This is due to energy scattering on local waveguide modes.

5.1.2 Comparison with classical damping treatments

Let us use the Ashby diagram presented in the introduction (see Fig. 1.6) from comparing different damping strategies. In order to locate the ABH treatment on such a diagram, equivalent characteristics need to be calculated. The mean equivalent ratio of

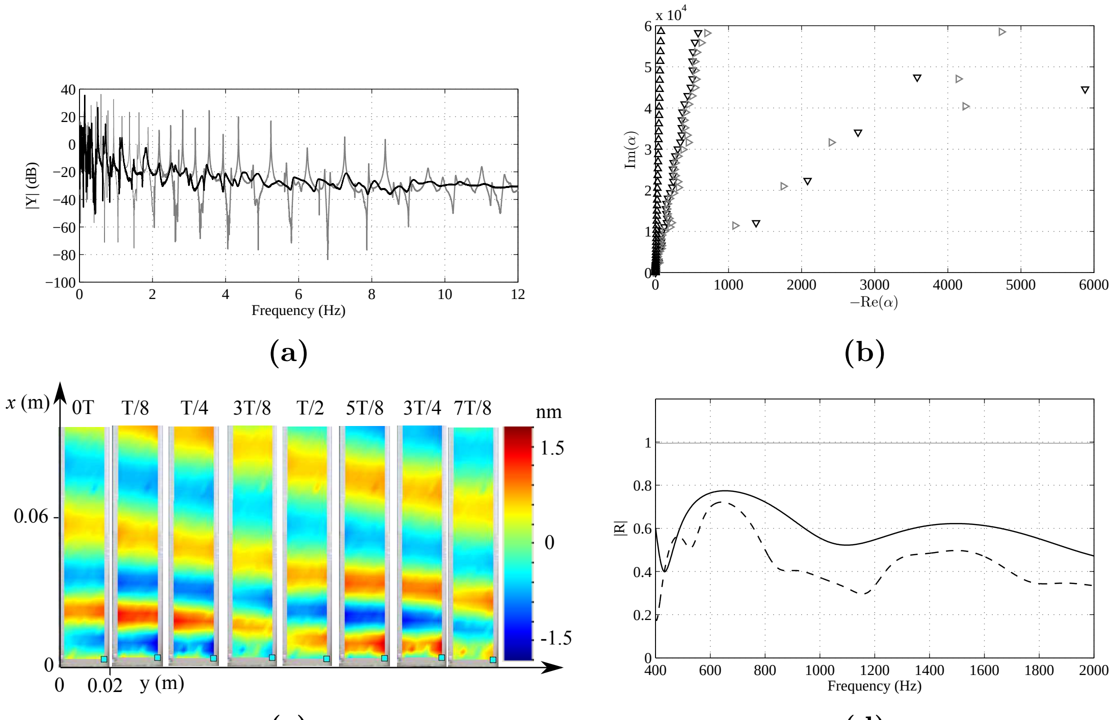

(a) (b)

(c) (d)

Figure 5.1: (a) Mobility transfer function of Ref and ABH (see Fig. 2.12(c)). (b) Eigenvalues spectrum of Ref, ABH and ABH with imperfection (see Fig. 4.19(d)). (c) Displacement field of the aluminium ABH beam (see Fig. 2.9(b)). (d) Reflection coefficient of uniform, ABH and imperfect ABH plate (see Fig. 4.18.)

Young's modulus over mass density for the beam treated with ABH is computed using Eqs. (3.2) and (3.3). The mean modal loss factor is calculated above the ABH frequency limit (see Sec. 3.1.3.3) from the simulated modal loss factors (model without imperfections, Chap. 3). These results are obtained using the finite difference model of Sec. 3.1.1 with parameters of Tab. 5.1. The damping performance is linked to localisation of the energy in the tapered region, hence it is also link to the relative length of the ABH profile. In this case, it represents 10 % of the total length of the simulated beam.

Fig. 5.2 shows where the ABH treatment lays for the studied case. It illustrates the performance of the treatment as it is both more efficient and comparatively lighter than most classical treatments. Note that the configurations proposed in Tab. 5.1 do not compete with heavier classical solutions because loss factors are inferior to 10 %.

Characteristics of material	Geometrical characteristics
Aluminium ABH beam	
E=70 GPa, ρ=2700 kg.m^{-3}	L=2 m, b=0.1 m, m=2
η=0.2 %,	x_0=[0.007, 0.01] m, x_{ABH}=[0.2, 0.3] m, h_t=20 μm
Damping layer	
E_l=20 MPa, ρ_l=950 kg.m^{-3},	x_l=0.05 m
η_l=80 %	h_l=[500, 1000, 2000] μm

Table 5.1: Geometrical and material characteristics of the simulated ABH beam.

5.2 General conclusions

5.2.1 Summary of the results

This document is organized in three main parts. In Chap. 2, experimental observations and analyses were made on beam with an ABH extremity. The two modal and wave approaches are used in conjunction. On the one hand, the reduction of the resonant behaviour of the ABH is due to the increase in modal loss factors that produces an increase of the modal overlap of the structure. On the other hand, the ABH termination is a region where the wavelength decreases; it generates wave propagation phenomena and can be thus seen as an anechoic termination or a pseudo-infinite structure. A measurement of the reflection coefficient with a Kundt-like technique indeed confirms this fact and shows that the ABH termination is characterized by a low reflection coefficient and an important phase unwrapping.

In Chap. 3, a two-dimensional numerical model of the beam based on the finite difference method confirms the increase of modal loss factor as an increase of the imaginary part of the eigenvalues, and reveals that this is due to a higher localisation of the energy in the tapered region, that has a higher structural loss factor. Moreover, the fact that the structure is inherently two-dimensional at the ABH extremity is confirmed as the

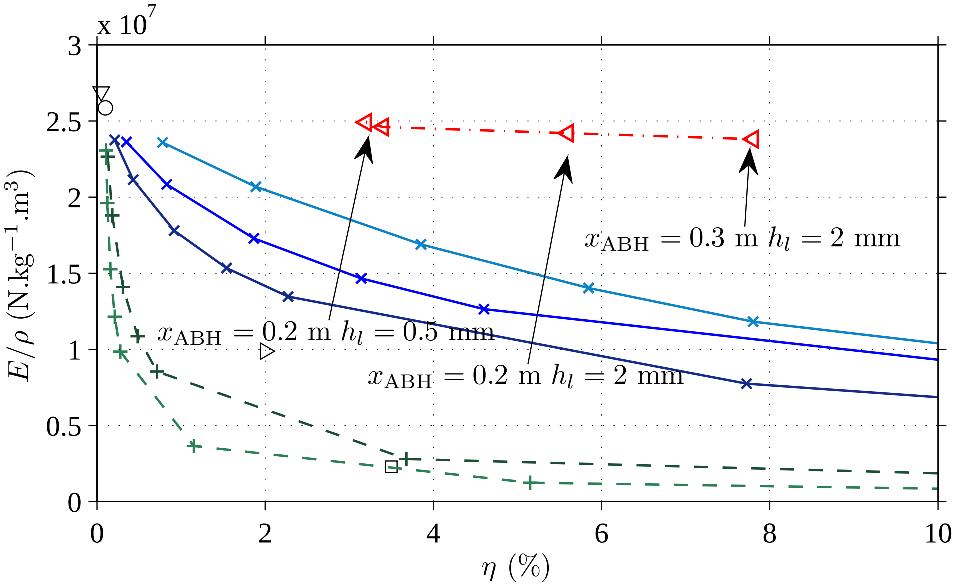

Figure 5.2: Comparison of intrinsic loss factor η versus specific Young's modulus E/ρ for materials: aluminium (○), steel (▽), polymer FullCure (□), Sonoston (◁), surface damping treatments: free layer on aluminium beam with damping layer made of Viton B (dashed line, +, dark green), Paracril BJ 50 (dashed line, +, light green), constrained layer on aluminium beam with damping layer made of Soundcoat DYAD (full line, x, medium blue), 3M ISD 110 (full line, x, dark blue), 3M ISD 112 (full line, x, light blue) and aluminium beam including ABH (dashdotted line, ◁, red). Detailed material properties are given in Appendix A.1.

model contains local modes that are identified as plate modes, and called hyper-damped modes. The ABH can also be seen as a correction length of the beam structure that may generate a small increase of the modal density; this last point do not seem significant in a practical case. The analytical correction length and its measured value have the same order of magnitude. Comparisons between theoretical and measured values of the MOF and the reflection coefficient show a good agreement.

Chap. 4 investigates effects of the tip imperfections due to the manufacturing techniques. This effect is suggested by experimental tests. Thanks to a multimodal waveguide model linked to a simple model of an elementary imperfection, it is shown that couplings between a plane incident wave and local modes happen and translate into a drop of the reflection coefficient of the extremity. The magnitude and the frequency range of this drop are affected by the damping properties of the tapered region. It is due to excitation and local resonance of confined modes. It is also revealed that the tapered profile itself produces reflection. An enhancement of the ABH effect is suggested by a control of the irregularity at the extremity.

Finally, Sec. 5.1.2 emphasizes the performance of the ABH method versus classical damping treatments as a damping method without added mass.

5.2.2 Ideas for further directions

The measurement technique for the reflection coefficient presented in Chap. 2 is interesting for its own sake and is able to successfully provide measurements on the ABH termination. In practice, it is however limited by the number and the duration of measurements made with a laser vibrometer. The full field digital optic holography [74] is a promising contactless measurement technique, competing with laser vibrometry. As the name suggests, it allows to acquire signals of displacement of a structure in one single shot embedding a large number of measurement points (1024×1024). The measurement technique of R could then apply with a higher number of measurements and without the hassle of doing them all. Moreover, high speed digital holography [113] would allow the observation of a wave packet entering the ABH region in the time domain. This is an objective of the PhD work of J. Poittevin at LAUM (2012-2015, PhD work supported by the VIBROLEG project, IRT Jules Verne).

As it is suggested in Chap. 3, damping due to air could play a minor role in the total damping seen in the experiment and may be embedded in an equivalent structural loss factor in the model. An experiment in vacuum is in preparation allowing the measurements of transfer functions of the beams and estimation of the reflection coefficient of the ABH termination.

Controlled irregularities of the ABH termination is suggested by Chap. 4 as a way to enhance the damping effect by smartly coupling local modes. As this phenomena seems to be linked with the number of propagating modes in the tapered region, an increase of this number can also be considered by enlarging the extremity in the case of a beam; of course, this is not necessary in the case of a circular ABH on a plate.

Appendix A

Annexes

A.1 Characteristics of damping solutions

The material and geometrical characteristics of the damping solutions mentioned in Chap. 1 for the resonant beam are presented in Tab. A.1.

Characteristics of material	Geometrical characteristics
Steel beam	
E_1=210 GPa ρ_1=7800 kg.m^{-3} η_1=0.05 %	
Aluminium beam	
E_1=70 GPa ρ_1=2700 kg.m^{-3} η_1=0.2 %	
Polymer VeroWhitePlus FullCure 835 beam	
E_1=2.7 GPa ρ_1=1180 kg.m^{-3} η_1=3.5 %	
Sonoston beam	
E_1=76 GPa ρ_1=7700 kg.m^{-3} η_1=2 %	
Carbon composite beam	
E_1=85 GPa ρ_1=1600 kg.m^{-3} η_1=0.6 %	
Free layer: Aluminium beam covered with Eriks Viton B	
E_2=103 MPa ρ_2=1900 kg.m^{-3} η_2=120 %	H_1=0.02 m H_2=1–100 mm
Free layer: Aluminium beam covered with Paracril BJ 50 PHRC	
E_2=55 MPa ρ_2=920 kg.m^{-3} η_2=65%	H_1=0.02 m H_2=1–100 mm
Constrained layer: Aluminium beam covered with Soundcoat DYAD	
G_2=55 MPa ρ_2=920 kg.m^{-3} η_2=65%	H_1=0.02 m H_2=1–100 mm
E_1=70 GPa ρ_1=2700 kg.m^{-3} η_1=0.2 %	H_3=1 mm
Constrained layer: Aluminium beam covered with 3M ISD 110	
G_2=41 MPa ρ_2=950 kg.m^{-3} η_2=50%	H_1=0.02 m H_2=1–100 mm
E_1=70 GPa ρ_1=2700 kg.m^{-3} η_1=0.2 %	H_3=1 mm
Constrained layer: Aluminium beam covered with 3M ISD 112	
G_2=69 MPa ρ_2=950 kg.m^{-3} η_2=80%	H_1=0.02 m H_2=1–100 mm
E_1=70 GPa ρ_1=2700 kg.m^{-3} η_1=0.2 %	H_3=1 mm

Table A.1: Geometrical and material parameters used in Fig. 5.2 (surface damping material data at 20°C from [100], carbon composite data from [16] and polymer data from CTTM, Le Mans).

A.2 RKU model for shear damping

In this appendix, formulas for equivalent properties of three layers structure are reminded according to the Ross-Ungar-Kerwin model of Ref. [116]. For a layered structure, E_i, I_i, H_i, η_i are the Young's modulus, inertia of the cross-section, thickness and loss factor of the i-th layer, respectively, with i=1, 2 or 3. Layer 1 is the holding structure, layer 2 is the damping layer, often made of viscoelastic material and layer 3 is a constraining layer, often made of the same material than layer 1. The geometry of the layered structure is illustrated on Fig. A.1.

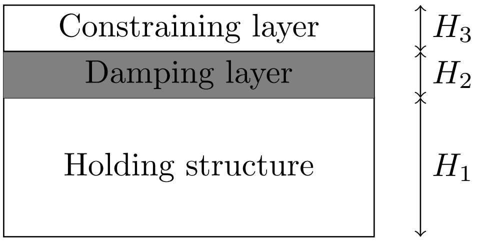

Figure A.1: Scheme of a three layers structure showing the thicknesses of the layers.

The following notations are used:

$$H_{31} = \frac{H_1 + H_3}{2} + H_2, \tag{A.1}$$

$$H_{21} = \frac{H_1 + H_2}{2}, \tag{A.2}$$

$$g = \frac{G_2}{E_3 H_3 H_2 p^2}, \tag{A.3}$$

where p is the wavenumber in substructure 1,

$$D = \frac{(E_2 H_2 (H_{21} - H_{31}/2) + g(E_2 H_2 H_{21} + E_3 H_3 H_{31}))}{(E_1 H_1 + E_2 H_2/2 + g(E_1 H_1 + E_2 H_2 + E_3 H_3))}. \tag{A.4}$$

Finally the complex stiffness of the compound structure is

$$\begin{aligned} EI = {} & \frac{E_1 H_1^3}{12} + \frac{E_2 H_2^3}{12} + \frac{E_3 H_3^3}{12} - \frac{E_2 H_2^2}{12} \frac{(H_{31} - D)}{1+g} + E_1 H_1 D^2 + E_2 H_2 (H_{21} - D)^2 \\ & + E_3 H_3 (H_{31} - D)^2 - \frac{(E_2 H_2/2(H_{21} - D) + E_3 H_3 (H_{31} - D))(H_{31} - D)}{(1+g)}. \end{aligned} \tag{A.5}$$

A.3 Finite difference model

A.3.1 Discrete form of the equation of motion

The discrete equation of motion (3.17):

$$\begin{aligned}\frac{h_n^{-1/2}}{\tilde{x}_{\text{av}}^2}\delta_{\tilde{x}+}\Big[(\mu_{\tilde{x}-}h_n^{-1/2})\delta_{\tilde{x}-}\Big[D_n\Big(\frac{h_n^{-1/2}}{\tilde{x}_{\text{av}}^2}\delta_{\tilde{x}+}((\mu_{\tilde{x}-}h_n^{-1/2})\delta_{\tilde{x}-}w_{n,q}) + \delta_{yy}w_{n,q}\Big)\Big]\Big]\\ + D_n\delta_{yy}\Big[\frac{h_n^{-1/2}}{\tilde{x}_{\text{av}}^2}\delta_{\tilde{x}+}((\mu_{\tilde{x}-}h_n^{-1/2})\delta_{\tilde{x}-}w_{n,q}) + \delta_{yy}w_{n,q}\Big]\\ - (1-\nu)\Big(\frac{h_n^{-1/2}}{\tilde{x}_{\text{av}}^2}\delta_{\tilde{x}+}((\mu_{\tilde{x}-}h_n^{-1/2})\delta_{\tilde{x}-}D_n)\delta_{yy}w_{n,q}\Big) - \rho h_n\omega^2 w_{n,q} = 0.\end{aligned} \tag{A.6}$$

can be put in explicit form by using points neighbouring $w_{l,m}$:

$$\sum_i\sum_j(\beta_{i,j}w_{i,j}) - \rho h_0\phi_n\omega^2 w_{n,q} = 0, \tag{A.7}$$

where the coefficients $\beta_{i,j}$ are:

$$\begin{aligned}\beta_{n,q} = \frac{(1-\nu)\phi_n^{-1/2}}{\tilde{x}_{av}^2\Delta_{\tilde{x}}^2\Delta_y^2}\Big((\phi_{n+1}^{-1/2}+\phi_n^{-1/2})(D_{n+1}-D_n) - (\phi_l^{-1/2}+\phi_{n-1}^{-1/2})(D_n-D_{n-1})\Big)\\ \frac{D_n}{\Delta_y^2}\Big(\frac{2}{\Delta_y^2} + 2(\frac{\phi_n^{-1/2}}{2\tilde{x}_{av}^2\Delta_{\tilde{x}}^2}(\phi_{n+1}^2 + 2\phi_n^{-1/2} + \phi_{n-1}^{-1/2}) + \frac{2}{\Delta_y^2})\Big) + \frac{\phi_n^{-1/2}}{2\tilde{x}_{av}\Delta_{\tilde{x}}^2}\\ \Big(\Big[(\phi_{n+1}^{-1/2}+\phi_n^{-1/2})\big[D_{n+1}\frac{\phi_{n+1}^{-1/2}}{2\tilde{x}_{av}^2\Delta_{\tilde{x}}^2}(\phi_{n+1}^{-1/2}+\phi_l^{-1/2}) + D_l\frac{\phi_n^{-1/2}}{2\Delta_{\tilde{x}}^2\tilde{x}_{av}^2}(\phi_{n+1}^{-1/2}+2\phi_n^{-1/2}+\phi_{n-1}^{-1/2})\\ + \frac{2D_n}{\Delta_y^2}\big]\Big]\Big[(\phi_n^{-1/2}+\phi_{n-1}^{-1/2})\big[D_n\frac{\phi_n^{-1/2}}{2\Delta_{\tilde{x}}^2\tilde{x}_{av}}(\phi_{n+1}^{-1/2}+2\phi_n^{-1/2}+\phi_{n-1}^{-1/2}) + \frac{2D_n}{\Delta_y^2}\\ + D_{n-1}\frac{\phi_{n-1}^{-1/2}}{2\tilde{x}_{av}^2\Delta_{\tilde{x}}^2}(\phi_n^{-1/2}+\phi_{n-1}^{-1/2})\big]\Big]\Big),\end{aligned} \tag{A.8}$$

$$\beta_{n,q+2} = \beta_{n,q-2} = \frac{D_n}{\Delta_y^4}, \tag{A.9}$$

$$\beta_{n+2,q} = \frac{\phi_n^{-1/2}\phi_{n+1}^{-1/2}D_{n+1}}{4\tilde{x}_{av}^4\Delta_{\tilde{x}}^4}(\phi_{n+1}^{-1/2}+\phi_n^{-1/2})(\phi_{n+2}^{-1/2}+\phi_{n+1}^{-1/2}), \tag{A.10}$$

$$\beta_{n+2,q} = \frac{\phi_n^{-1/2}\phi_{n-1}^{-1/2}D_{n-1}}{4\tilde{x}_{av}^4\Delta_{\tilde{x}}^4}(\phi_{n-1}^{-1/2}+\phi_n^{-1/2})(\phi_{n-2}^{-1/2}+\phi_{n-1}^{-1/2}), \tag{A.11}$$

$$
\begin{aligned}
\beta_{n+1,q} = {} & \frac{-D_n\phi_l^{-1/2}}{\tilde{x}_{av}^2\Delta_{\tilde{x}}^2\Delta_y^2}(\phi_{n+1}^{-1/2}+\phi_l^{-1/2}) - \frac{\phi_n^{-1/2}}{2\tilde{x}_{av}^2\Delta_{\tilde{x}}^2}\Big((\phi_{n+1}^{-1/2}+\phi_n^{-1/2}) \\
& \big(\frac{D_{n+1}\phi_{n+1}^{-1/2}}{2\tilde{x}_{av}^2\Delta_{\tilde{x}}^2}(\phi_{n+2}^{-1/2}+2\phi_{n+1}^{-1/2}+\phi_n^{-1/2}) + \frac{2D_{n+1}}{\Delta_y^2} + \frac{D_n\phi_n^{-1/2}}{2\tilde{x}_{av}^2\Delta_{\tilde{x}}^2}(\phi_{n+1}^{-1/2}+\phi_n^{-1/2})\big) \\
& + (\phi_n^{-1/2}+\phi_{n-1}^{-1/2})\frac{D_n\phi_n^{-1/2}}{2\tilde{x}_{av}^2\Delta_{\tilde{x}}^2}(\phi_{n+1}^{-1/2}+\phi_n^{-1/2})\Big),
\end{aligned}
\tag{A.12}
$$

$$
\begin{aligned}
\beta_{n-1,q} = {} & \frac{-D_n\phi_n^{-1/2}}{\tilde{x}_{av}^2\Delta_{\tilde{x}}^2\Delta_y^2}(\phi_n^{-1/2}+\phi_{n-1}^{-1/2}) - \frac{\phi_n^{-1/2}}{2\tilde{x}_{av}^2\Delta_{\tilde{x}}^2}\Big((\phi_{n+1}^{-1/2}+\phi_n^{-1/2}) \\
& \frac{D_n\phi_n^{-1/2}}{2\tilde{x}_{av}^2\Delta_{\tilde{x}}^2}(\phi_n^{-1/2}+\phi_{n-1}^{-1/2}) + (\phi_n^{-1/2}+\phi_{n-1}^{-1/2})\big(\frac{D_n\phi_n^{-1/2}}{2\tilde{x}_{av}^2\Delta_{\tilde{x}}^2}(\phi_n^{-1/2}+\phi_{n-1}^{-1/2}) \\
& + \frac{D_{n-1}\phi_{n-1}^{-1/2}}{2\tilde{x}_{av}^2\Delta_{\tilde{x}}^2}(\phi_n^{-1/2}+2\phi_{n-1}^{-1/2}+\phi_{n-1}^{-1/2}) + \frac{2D_{n-1}}{\Delta_y^2}\big)\Big),
\end{aligned}
\tag{A.13}
$$

$$
\begin{aligned}
\beta_{n,q+1} = {} & \frac{(\nu-1)\phi_n^{-1/2}}{2\tilde{x}_{av}^2\Delta_{\tilde{x}}^2\Delta_y^2}\Big((\phi_{n+1}^{-1/2}+\phi_n^{-1/2})(D_{n+1}-D_n) - (\phi_n^{-1/2}+\phi_{n-1}^{-1/2})(D_n-D_{n-1})\Big) \\
& - \frac{D_n}{\Delta_y^2}\big(\frac{\phi_n^{-1/2}}{\tilde{x}_{av}^2\Delta_{\tilde{x}}^2}(\phi_{n+1}^{-1/2}+2\phi_n^{-1/2}+\phi_{n-1}^{-1/2}) + \frac{4}{\Delta_y^2}\big),
\end{aligned}
\tag{A.14}
$$

$$
\begin{aligned}
\beta_{n,q-1} = {} & \frac{(\nu-1)\phi_n^{-1/2}}{2\tilde{x}_{av}^2\Delta_{\tilde{x}}^2\Delta_y^2}\Big((\phi_{n+1}^{-1/2}+\phi_n^{-1/2})(D_{n+1}-D_n) - (\phi_n^{-1/2}+\phi_{n-1}^{-1/2})(D_n-D_{n-1})\Big) \\
& - \frac{D_n}{\Delta_y^2}\big(\frac{\phi_n^{-1/2}}{\tilde{x}_{av}^2\Delta_{\tilde{x}}^2}(\phi_{n+1}^{-1/2}+2\phi_n^{-1/2}+\phi_{n-1}^{-1/2}) + \frac{4}{\Delta_y^2}\big),
\end{aligned}
\tag{A.15}
$$

$$
\beta_{n+1,q+1} = \frac{\phi_n^{-1/2}(\phi_{n+1}^{-1/2}+\phi_n^{-1/2})}{2\tilde{x}_{av}^2\Delta_{\tilde{x}}^2\Delta_y^2}(D_{n+1}+D_n), \tag{A.16}
$$

$$
\beta_{n+1,q-1} = \frac{\phi_n^{-1/2}(\phi_{n+1}^{-1/2}+\phi_n^{-1/2})}{2\tilde{x}_{av}^2\Delta_{\tilde{x}}^2\Delta_y^2}(D_{n+1}+D_n), \tag{A.17}
$$

$$
\beta_{n-1,q+1} = \frac{\phi_n^{-1/2}(\phi_{n-1}^{-1/2}+\phi_n^{-1/2})}{2\tilde{x}_{av}^2\Delta_{\tilde{x}}^2\Delta_y^2}(D_{n-1}+D_n), \tag{A.18}
$$

$$
\beta_{n-1,q-1} = \frac{\phi_n^{-1/2}(\phi_{n-1}^{-1/2}+\phi_n^{-1/2})}{2\tilde{x}_{av}^2\Delta_{\tilde{x}}^2\Delta_y^2}(D_{n-1}+D_n), \tag{A.19}
$$

A.3.2 Numerical boundary conditions

In the general case, the discrete spatial operator uses 13 points. At the edges, depending on the boundary condition, N points *outside* the grid should be used. The discrete spatial operator then uses "fictive" points [14]. By respecting the discrete boundary conditions, the displacements of the fictive points can be expressed as functions of real points on the edges. Practically, it means modifying the expression of the coefficients of the spatial operator at the edges.

The boundary conditions can be discretized as follows, reminding that the choice of the forward or backward finite difference operators depends on the orientation of the edge or corner. The resulting equations are tedious to write and solve. It is proposed to solve them numerically. The example of the free corner condition at n=0, q=0 is given:

$$\frac{\phi_n^{-1/2}}{\tilde{x}_{av}^2}\delta_{\tilde{x}+}\Big(\mu_{\tilde{x}-}\phi_n^{-1/2}.\delta_{\tilde{x}-}w_{n,q}\Big) + \nu\delta_{yy}w_{n,q} = 0, \tag{A.20}$$

$$\delta_{yy}w_{n,q} + \frac{\nu\phi_n^{-1/2}}{\tilde{x}_{av}^2}\delta_{\tilde{x}+}\Big(\mu_{\tilde{x}-}\phi_n^{-1/2}.\delta_{\tilde{x}-}w_{n,q}\Big) = 0, \tag{A.21}$$

$$\delta_{\tilde{x}-}\delta_{y}w_{n,q} = 0, \tag{A.22}$$

$$\begin{multline}\frac{\phi_n^{-1/2}}{\tilde{x}_{av}}\delta_{\tilde{x}-}(D_n(\frac{\phi_n^{-1/2}}{\tilde{x}_{av}^2}\delta_{\tilde{x}+}(\mu_{\tilde{x}-}\phi_n^{-1/2}.\delta_{\tilde{x}-}w_{n,q}) + \nu\delta_{yy}w_{n,q}))\\ + 2D_n(1-\nu)\frac{\phi_n^{-1/2}}{\tilde{x}_{av}}\delta_{\tilde{x}-}\delta_{yy}w_{n,q} = 0, \tag{A.23}\end{multline}$$

$$\begin{multline}D_n\delta_{y-}(\nu\frac{\phi_n^{-1/2}}{\tilde{x}_{av}^2}\delta_{\tilde{x}+}(\mu_{\tilde{x}-}\phi_n^{-1/2}.\delta_{\tilde{x}-}w_{n,q} + \delta_{yy}w_{n,q})\\ + 2\frac{\phi_n^{-1/2}}{\tilde{x}_{av}^2}(1-\nu)\delta_{\tilde{x}+}(\mu_{\tilde{x}-}(D_n\phi_n^{-1/2})\delta_{\tilde{x}-}\delta_{y-}w_{n,q}) = 0. \tag{A.24}\end{multline}$$

This formulation of the boundary conditions can be made explicit in order to obtain a set of equations relating the displacements of real points and fictive points neighbouring $\tilde{x}_{n,q}$. Let us define the vector $\mathbf{W}^{\text{fict}}$ containing the N fictive displacements (size $N\times1$) and the vector $\mathbf{W}^{\text{real}}$ containing the $13-N$ real displacement. At a given point the N equations of the boundary conditions (for example Eqs. (A.20)-(A.24)) can be written in a matrix formulation:

$$\begin{bmatrix} \mathbf{A} & \mathbf{B} \end{bmatrix} . \begin{bmatrix} \mathbf{W}^{\text{fict}} \\ \mathbf{W}^{\text{real}} \end{bmatrix} = \mathbb{O}_{N\times1}, \tag{A.25}$$

where $\mathbf{A}$ and $\mathbf{B}$ are $N\times N$ and $N\times(13-N)$ matrices, respectively. The displacements of the fictive points can be deduced by

$$\mathbf{W}^{\text{fict}} = (-\mathbf{A})^{-1}.\mathbf{B}.\mathbf{W}^{\text{real}}, \tag{A.26}$$

or

$$W_j^{\text{fict}} = \gamma_{ji}W_i^{\text{real}}. \tag{A.27}$$

where γ_{ji} are coefficients of matrix $(-\mathbf{A})^{-1}.\mathbf{B}$. Then, the discrete spatial operator can be expressed using only real displacement W_i:

$$\sum_i(\beta_i + \gamma_{ji}\beta_j)W_i. \tag{A.28}$$

A.3.3 Validation of the numerical method

The finite difference method is validated against a FEM model (COMSOL, grid set on ’finer’) for a uniform plate and an ABH plate without damping layer (see Fig. 2.1(a) and Tab. 2.1 for the geometry). The relative error ε

$$\varepsilon = \frac{f_{\mathrm{FDM}} - f_{\mathrm{FEM}}}{f_{\mathrm{FEM}}}. \tag{A.29}$$

on eigenfrequencies f_{FDM} given by the finite difference scheme is plotted on Fig. A.2 for the reference beam and the ABH beam with parameters of Tab. 3.1 using a 640×240 grid ($\Delta_{\tilde{x}} = 1.6 \times 10^{-3}$, $\Delta_y = 4.2 \times 10^{-4}$ m). Interestingly, the results are globally more accurate for the variable thickness case. In the worst case, the maximum error is less than 2 %. The sudden drop at 2000 Hz in the ABH result concern a local mode.

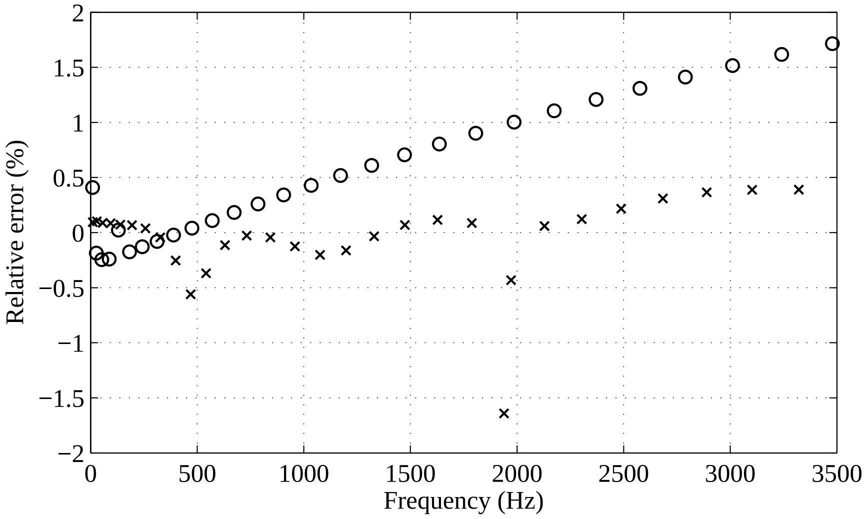

Figure A.2: Error on eigenfrequencies estimation of FDM method compared FEM on Reference (○) and ABH (×) plates.

A.4 Multimodal waveguide model

A.4.1 Details on the plate equations

The governing equations for the flexural motion of plate with inhomogeneities along the longitudinal x-direction (plate parameters remains invariant along transverse y-direction), and in harmonic regime (with the $e^{-\mathrm{j}\omega t}$ time convention) are [84]:

$$w = w(x,y) \tag{A.30}$$

$$\theta_x(x,y) = \frac{\partial w}{\partial x}, \tag{A.31}$$

$$M_x(x,y) = -D\left(\frac{\partial^2 w}{\partial x^2} + \nu\frac{\partial^2 w}{\partial y^2}\right), \tag{A.32}$$

$$M_y(x,y) = -D\left(\frac{\partial^2 w}{\partial y^2} + \nu\frac{\partial^2 w}{\partial x^2}\right), \tag{A.33}$$

$$M_{xy}(x,y) = -D(1-\nu)\frac{\partial^2 w}{\partial x \partial y}, \tag{A.34}$$

$$Q_x(x,y) = \frac{\partial M_x}{\partial x} + \frac{\partial M_{xy}}{\partial y}, \tag{A.35}$$

$$Q_y(x,y) = \frac{\partial M_{xy}}{\partial x} + \frac{\partial M_y}{\partial y}, \tag{A.36}$$

$$\frac{\partial Q_x}{\partial x} + \frac{\partial Q_y}{\partial y} = -\rho h \omega^2 w, \tag{A.37}$$

where $w(x,y)$ is the displacement, $\theta_x(x,y)$ and $\theta_y(x,y)$ are the slopes along x and y-direction, $M_x(x,y)$ and $M_y(x,y)$ are the bending moments around x and y, $M_{xy}(x,y)$ is the twisting moment, $Q_x(x,y)$ and $Q_y(x,y)$ are the shear forces, $D(x)$ is the bending stiffness, ν is the Poisson's ratio, $\rho(x)$ is the mass density, $h(x)$ is the thickness and ω is the angular frequency. Moreover, the total shear forces V_x and V_y including the effects of the twisting moments are defined:

$$V_x(x,y) = Q_x + \frac{\partial M_{xy}}{\partial y} = \frac{\partial M_x}{\partial x} + 2\frac{\partial M_{xy}}{\partial y}, \tag{A.38}$$

$$V_y(x,y) = Q_y + \frac{\partial M_{xy}}{\partial x} = \frac{\partial M_y}{\partial y} + 2\frac{\partial M_{xy}}{\partial x}. \tag{A.39}$$

The aim is to establish the relations between variables w, θ_x, M_x and V_x and their first-order partial derivatives with respect to x. First, Eq. (A.31) gives

$$\frac{\partial w}{\partial x} = \theta_x. \tag{A.40}$$

Using Eq. (A.32) and the derivative with respect to x of Eq. (A.31) yields

$$\frac{\partial \theta_x}{\partial x} = -\frac{1}{D} M_x - \nu \frac{\partial^2 w}{\partial y^2}. \tag{A.41}$$

From Eq. (A.34), the twisting moment is

$$M_{xy} = -D(1-\nu)\frac{\partial \theta_x}{\partial y}, \tag{A.42}$$

then Eq. (A.42) is inserted in Eq. (A.38) to obtain

$$\frac{\partial M_x}{\partial x} = V_x - 2(1-\nu) D \frac{\partial^2 \theta_x}{\partial y^2}. \tag{A.43}$$

The derivation of Eq. (A.38) with respect to x yields

$$\frac{\partial V_x}{\partial x} = \frac{\partial Q_x}{\partial x} + \frac{\partial^2 M_{xy}}{\partial x \partial y}. \tag{A.44}$$

Moreover, Eq. (A.37) directly gives

$$\frac{\partial Q_x}{\partial x} = -\rho h \omega^2 w - \frac{\partial Q_y}{\partial y}, \tag{A.45}$$

where appears the derivation of Eq. (4.7) with respect to y:

$$\frac{\partial Q_y}{\partial y} = \frac{\partial^2 M_{xy}}{\partial x \partial y} + \frac{\partial^2 M_y}{\partial y^2}, \tag{A.46}$$

which writes, using Eq. (A.33):

$$\frac{\partial Q_y}{\partial y} = \frac{\partial^2 M_{xy}}{\partial x \partial y} - D\frac{\partial^4 w}{\partial y^4} - \nu D \frac{\partial^2}{\partial y^2}\frac{\partial^2 w}{\partial x^2}. \tag{A.47}$$

Combining Eqs. (A.47),(A.45) and (A.44) gives

$$\frac{\partial V_x}{\partial x} = -\rho h \omega^2 w + D\frac{\partial^4 w}{\partial y^4} + \nu D \frac{\partial^2}{\partial y^2}\frac{\partial^2 w}{\partial x^2}. \tag{A.48}$$

Finally, the moment M_x appears using Eq. (A.32):

$$D\frac{\partial^2 w}{\partial x^2} = -M_x - \nu D \frac{\partial^2 w}{\partial y^2}, \tag{A.49}$$

and Eq. (A.48) becomes:

$$\frac{\partial V_x}{\partial x} = -\rho h \omega^2 w + D(1-\nu^2)\frac{\partial^4 w}{\partial y^4} - \nu \frac{\partial^2 w}{\partial y^2}. \tag{A.50}$$

Eqs. (A.40), (A.41), (A.43) and (A.50) are the researched relations.

A.4.2 Assembly rule for scattering matrices

In order to compute the scattering matrix of a whole inhomogeneous guide thanks to scattering matrices of elementary regions, it is useful to define an operator that combine the scattering matrices of two consecutive regions A and B. If $\mathbf{S}_{AB}$ is the scattering matrix of the concatenation of the two regions, it can be shown that $\mathbf{S}_{AB}$ can be computed from $\mathbf{S}_A$ and $\mathbf{S}_B$ by using a $\star$ operator [107]:

$$\mathbf{S}_{AB} = \mathbf{S}_A \star \mathbf{S}_B. \tag{A.51}$$

with

$$\mathbf{S}_{AB} = \begin{bmatrix} \mathbf{T}^{+-}_{AB} & \mathbf{R}^{-}_{AB} \\ \mathbf{R}^{+}_{AB} & \mathbf{T}^{-+}_{AB} \end{bmatrix}, \quad \mathbf{S}_{A} = \begin{bmatrix} \mathbf{T}^{+-}_{A} & \mathbf{R}^{-}_{A} \\ \mathbf{R}^{+}_{A} & \mathbf{T}^{-+}_{A} \end{bmatrix}, \quad \mathbf{S}_{B} = \begin{bmatrix} \mathbf{T}^{+-}_{B} & \mathbf{R}^{-}_{B} \\ \mathbf{R}^{+}_{B} & \mathbf{T}^{-+}_{B} \end{bmatrix}. \tag{A.52}$$

Eq. (A.51) is also called assembly rule for scattering matrices. The four submatrices $\mathbf{T}^{+-}_{AB}$, $\mathbf{R}^{-}_{AB}$, $\mathbf{R}^{+}_{AB}$ and $\mathbf{T}^{-+}_{AB}$ of $\mathbf{S}_{AB}$ write

$$\mathbf{T}^{+-}_{AB} = \mathbf{T}^{+-}_{A}(\mathbf{I} - \mathbf{R}^{-}_{B}\mathbf{R}^{+}_{A})^{-1}\mathbf{T}^{+-}_{B}, \tag{A.53}$$

$$\mathbf{R}^{-}_{AB} = \mathbf{R}^{-}_{A} + \mathbf{T}^{+-}_{A}(\mathbf{I} - \mathbf{R}^{-}_{B}\mathbf{R}^{+}_{A})^{-1}\mathbf{R}^{-}_{B}\mathbf{T}^{-+}_{A}, \tag{A.54}$$

$$\mathbf{R}^{+}_{AB} = \mathbf{R}^{+}_{B} + \mathbf{T}^{-+}_{B}(\mathbf{I} - \mathbf{R}^{+}_{A}\mathbf{R}^{-}_{B})^{-1}\mathbf{R}^{+}_{A}\mathbf{T}^{+-}_{B}, \tag{A.55}$$

$$\mathbf{T}^{-+}_{AB} = \mathbf{T}^{-+}_{B}(\mathbf{I} - \mathbf{R}^{+}_{A}\mathbf{R}^{-}_{B})^{-1}\mathbf{T}^{-+}_{A}. \tag{A.56}$$

A.4.3 Convergence and errors

A.4.3.1 Convergence: effect of the spatial step

In the case of the imperfect ABH plate described in Sec. 4.4.1, the mean error ε on the $[f_{min}\ f_{max}]$ range

$$\varepsilon = \frac{1}{f_{max} - f_{min}} \int_{f_{min}}^{f_{max}} \frac{|R_\Delta(f) - R_{\mathrm{Ref}}(f)|^2}{|R_{\mathrm{Ref}}(f)|^2}\,\mathrm{d}f, \tag{A.57}$$

is considered, where $R_K = (R^{+}_{pp})_{11}$ evaluated at $x = l_{\mathrm{ABH}}$ with spatial step Δ and $R_{\mathrm{Ref}} = (R^{+}_{pp})_{11}$ evaluated at $x = l_{\mathrm{ABH}}$ with a small spatial step $\Delta = 5 \times 10^{-5}$ m for which the numerical solution has converged. Computations are done with 30 modes on the 400-2000 Hz frequency range. It is clear that for $\Delta = 10^{-4}$ m, the error is less than 0.01 %. This discretization approximately corresponds to six points per wavelength.

A.4.3.2 Comparison to FEM solution

The numerical resolution presented in Sec. 4.3.3 is compared with a FEM solution (COMSOL) for uniform and ABH cases (for geometry and parameters, see Fig. 4.4 and Tab. 4.1). The computation of $\mathbf{Z}(x)$ and $w(x, y)$ is done with K=30 modes and $\Delta = 10^{-4}$

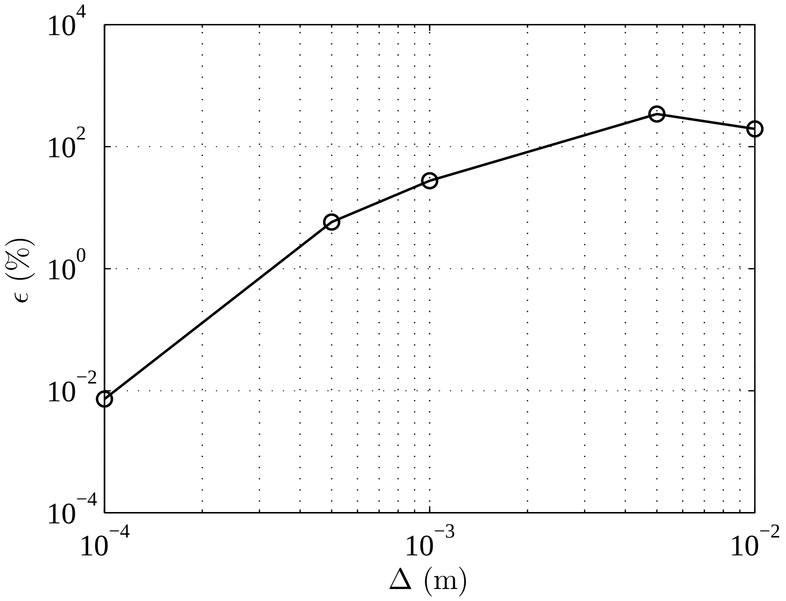

Figure A.3: Error ε on the mean $(R^+_{pp})_{11}$ estimation for different spatial steps Δ.

m with respect to frequency. Mobility transfer functions are plotted on Fig. A.4 with excitation and observation points located at (0.15,0.05). The results for the uniform plate fit perfectly while only minor differences are seen between the two compared solutions for the ABH plate.

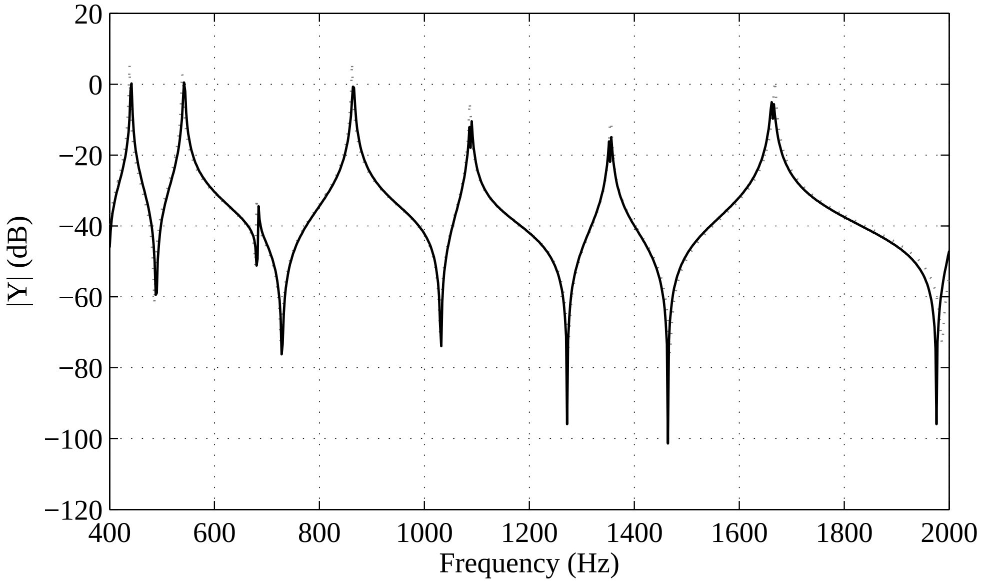

(a)

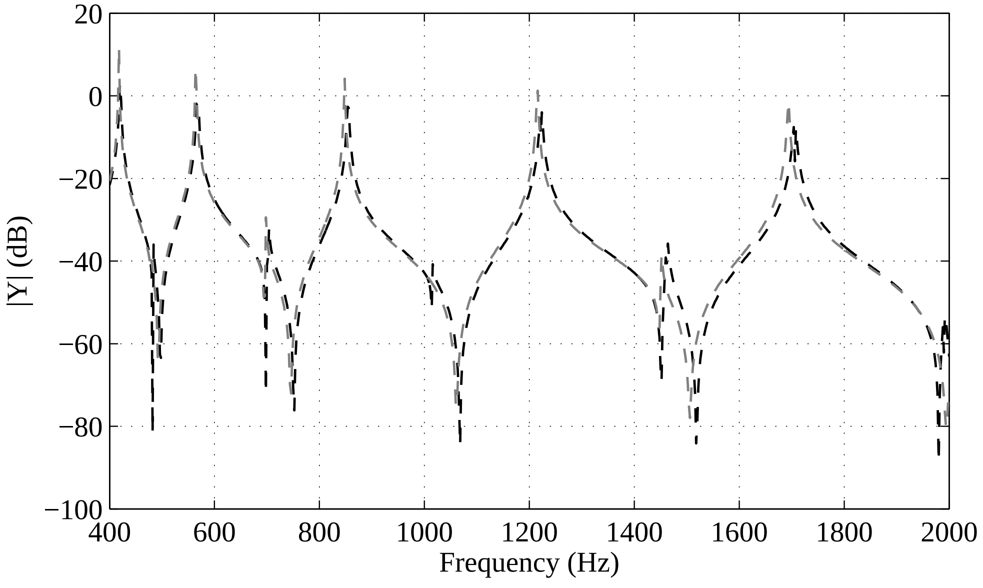

(b)

Figure A.4: Mobility transfer functions for multimodal model (grey) and FEM (black) for (a) Uniform plate and (b) ABH plate.

REFERENCES

[1] ADEME. Charte d'engagements volontaires de réduction des émissions de CO2 du transport routier de voyageurs. Fiches Actions, Decembre 2012.

[2] K.M. Ahmida and J.R.F. Arruda. On the relation between complex modes and wave propagation phenomena. *Journal of Sound and Vibration*, 255(4):663–684, August 2002.

[3] H. Akaike. Information theory and an extension of the maximum likelihood principle. In *Proc. of the 2nd International Symposium on Information Theory*, 1973. ex AIC.

[4] O. Aklouche, A. Pelat, S. Maugeais, and F. Gautier. Scattering of flexural waves from an acoustic black hole in an infinite thin plate. In *Medyna 2013, Marrakech 23–25 april 2013*, 2013.

[5] O. Aklouche, A. Pelat, S. Maugeais, and F. Gautier. Modèle de la diffusion des ondes de flexion par un trou noir acoustique bi-dimensionnel. In *Congrès Français d'Acoustique, Poitiers, 22–25 april 2014*, 2014.

[6] M. Amabili. Theory and experiments for large-amplitude vibrations of rectangular plates with geometric imperfections. *Journal of Sound and Vibration*, 291:539–565, 2006.

[7] K. Arcas, A. Chaigne, and S. Bilbao. Sound synthesis of circular plates by finite differences. *The Journal of the Acoustical Society of America*, 123(5):3522, 2008.

[8] M.F. Ashby. *Materials selection in mechanical design.* Butterworth Heinemann, Oxford, 2004.

[9] R. Badeau, B. David, and G. Richard. A new perturbation analysis for signal enumeration in rotational invariance techniques. *IEEE Transactions on Signal Processing*, 54(2):450–458, 2006.

[10] L. Barguet. Caractérisation de l'effet trou noir acoustique. Master's thesis, Université du Maine, 2011.

[11] C.F. Beards. *Structural Vibration: Analysis and Damping.* Arnold, 1996.

[12] J. Berthaut, M. N. Ichchou, and L. Jézéquel. Piano soundboard: Structural behavior and numerical and experimental study in the modal range. *Applied Acoustics*, 64:1113–1136, 2003.

[13] G. Bienvenu and L. Kopp. Optimality of high-resolution array processing using the eigensystem method. *IEEE Trans. Acoust. Speech Sig. Process.*, 31(5):1235–1245, 1983.

[14] S. Bilbao. *Numerical sound synthesis : finite difference schemes and simulation in musical acoustics.* John Wiley & Sons, Hoboken, 2009.

[15] X. Boutillon and K. Ege. Vibroacoustics of the piano soundboard: Reduced models, mobility synthesis, and acoustical radiation regime. *Journal of Sound and Vibration*, 332:4261–4279, 2013.

[16] E.P. Bowyer. *Experimental investigations of damping structural vibrations using the acoustic black hole effect.* PhD thesis, Loughborough University, 2012.

[17] E.P. Bowyer and V. V. Krylov. Damping of flexural vibration in turbofan blades using the acoustic black hole effect. *Applied Acoustics*, 76:359–365, 2014.

[18] E.P. Bowyer, D.J. O'Boy, V.V. Krylov, and F. Gautier. Experimental inverstigations of damping flexural vibrations in plates containing tapered indentations of power-law profile. *Applied Acoustics*, 74:553–560, 2013.

[19] E.P. Bowyer, D.J. O'Boy, V.V. Krylov, and J.L. Horner. Effect of geometrical and material imperfections on damping flexural vibrations in plates with attached wedges of power law profile. *Applied Acoustics*, 73(5):514–523, May 2012.

[20] C. Camier, C. Touzé, and O. Thomas. Non-linear vibrations of imperfect free-edge circular plates and shells. *European Journal of Mechanics A/Solids*, 28:500–515, 2009.

[21] R. N. Capps. Dynamic young's moduli of some commercially available polyurethanes. *Journal of the Acoustical Society of America*, 73(6):2000–2005, 1983.

[22] X. Carniel and J.-C. Pascal. Vibrational power flow measurement: structure characterization and wave reflection coefficient measurement. In *Proceedings INTER-NOISE 85, Munich, 18-20 September 1985*, pages 613–616, 1985.

[23] Y.-H. Chen and Y.-H. Huang. Timoshenko beam with tuned mass dampers and its design curves. *Journal of Sound and Vibration*, 278:873–888, 2004.

[24] M. G. Christensen, A. Jakobsson, and S. H. Jensen. Sinusoidal order estimation using angles between subspaces. *EURASIP J. Adv. Signal Process*, 2009:62:7–62:7, 2009. ex. ESPORT.

[25] D. Chronopoulos, O. Bareille, B. Troclet, and M. N. Ichchou. Modeling the response of composite panels by a dynamic stiffness approach. *Composite Structures*, 96:111–120, 2013.

[26] D. Chronopoulos, M. N. Ichchou, B. Troclet, and O. Bareille. Efficient prediction of the response of layered shells by a dynamic stiffness approach. *Composite Structures*, 97:401–404, 2013.

[27] G.C. Cohen. *Higher-order numerical methods for transient wave equations.* Springer, 2002.

[28] L. Cremer and M. Heckl. *Structure-Borne Sound: structural vibrations and sound radiation at audio frequencies, second edition.* Springer, 1988.

[29] J. Cuenca. *Wave models for the flexural vibrations of thin plates.* PhD thesis, Université du Maine, Le Mans, October 2009.

[30] J. Cuenca, A. Pelat, and F. Gautier. Vibration damping in polygonal plates using the acoustic black hole effect: model based on the image source method. In *20ieme Congrès Français de Mécanique, Besançon, 29 aout-2 Septembre 2011.*, 2011.

[31] J. Cuenca, A. Pelat, and F. Gautier. Improving the acoustic black hole effect for vibration damping in one dimensional structures. In *Acoustics 2012, Nantes, 23–27 april 2012*, 2012.

[32] P.R. Dahl. Solid friction damping of mechanical vibration. *AIAA Journal*, 14(12):1675–1682, 1976.

[33] J.P. Den Hartog. *Mechanical Vibrations (4th edition).* Dover, 1984.

[34] V. Denis, F. Gautier, and A. Pelat. Scattering of an imperfect acoustic black hole termination. In preparation.

[35] V. Denis, F. Gautier, and A. Pelat. Increasing the modal overlap factor of a beam using the acoustic black hole effect. In *Medyna 2013, Marrakech, 23–25 april 2013*, 2013.

[36] V. Denis, F. Gautier, and A. Pelat. Increasing the modal overlap factor of a beam using the acoustic black hole effect. In *11th International Conference of Vibration Problems, Lisbon, 9–12 septelber 2013*, 2013.

[37] V. Denis, F. Gautier, A. Pelat, and J. Poittevin. Measurement and modelling of the reflection coefficient of an acoustic black hole termination. *Journal of Sound and Vibration*, Submitted:0, 2014.

[38] V. Denis, A. Pelat, F. Gautier, and B. Elie. Modal overlap factor of a beam with an acoustic black hole termination. *Journal of Sound and Vibration*, 333:2475–2488, 2014.

[39] S.W. Doebling, C.R. Farrar, and M.B. Prime. A summary review of vibration-based damage identification methods. *The Shock and Vibration Digest*, 30(2):91–105, 1998.

[40] N. E. Dowling. *Mechanical Behavior of Materials, third edition.* Pearson, 2007.

[41] C. Dufort. Caractérisation de l'effet trou noir acoustique. Master's thesis, Université du Maine, 2012.

[42] K. Ege, X. Boutillon, and B. David. High-resolution modal analysis. *Journal of Sound and Vibration*, 325(4-5):852–869, September 2009.

[43] B. Elie, F. Gautier, and B. David. Macro parameters descibing the mechanical behavior of classical guitars. *The Journal of the Acoustical Society of America*, 132(6):4013–4024, 2012.

[44] D. J. Ewins. *Modal Testing.* Research Studies Press, 1984.

[45] C. Faure. Investigations expérimentales du trou noir acoustique. Master's thesis, Université du Maine, 2013.

[46] S. Felix and V. Pagneux. Multimodal analysis of acoustic propagation in three-dimensional bends. *Wave Motion*, 36(2):157–168, 2002.

[47] J.D. Ferry. *Viscoelastic properties of Polymers.* New York: John Wiley, 1980.

[48] J.D. Ferry, L. Grandine Jr., and E. Fitzgerald. The relaxation distribution functions of polyisobutylene inn the transition from rubeer-liike to glass-like behavior. *Journal of Applied Physics*, 24:911–916, 1953.

[49] P.A. Feurtado, S.C. Conlon, and F. Semperlotti. A normalized wave number variation parameter for acoustic black hole design. *The Journal of the Acoustical Society of America*, 136(2):EL148, 2014. JASA Express Letters.

[50] J.P. Fielding. *Introduction to Aircraft Design.* Cambridge, 1999.

[51] S. Foucaud, G. Michon, Y. Gourinat, A. Pelat, and F. Gautier. Immersed acoustic black hole as a travelling wave absorber: understanding artificial cochlear mechanics. In *Acoustics 2012, Nantes, 23–27 april 2012*, 2012.

[52] S. Foucaud, G. Michon, Y. Gourinat, A. Pelat, and F. Gautier. Artificial cochlea and acoustic black hole travelling waves observation: model and experimental results. *Journal of Sound and Vibration*, 333:3428–3439, 2014.

[53] F. Gautier, J. Cuenca, V.V. Krylov, and L. Simon. Experimental investigation of the acoustic black hole effect for vibration damping in elliptical plates. In *Acoustic'08, Paris*, 2008.

[54] F. Gautier, M.-H. Moulet, and J.-C. Pascal. Reflection, transmission and coupling of longitudinal and flexural waves at beam junctions. part i: Measurement methods. *Acta Acustica United with Acustica*, 92:982–997, 2006.

[55] V.B. Georgiev, J. Cuenca, , M. Gautier, F. Moleron, and L. Simon. Numerical and experimental investigation of the acoutic black hole effect for vibration damping in beams and elliptical plates. In *Euronoise 2009, Edinburgh*, 2009.

[56] V.B. Georgiev, J. Cuenca, F. Gautier, and L. Simon. Vibration reduction of beams and plates using acoustic black hole effect. In *Internoise 2010, 13-16 june 2010, Lisbon*, 2010.

[57] V.B. Georgiev, J. Cuenca, F. Gautier, L. Simon, and V.V. Krylov. Damping of structural vibrations in beams and elliptical plates using the acoustic black hole effect. *Journal of Sound and Vibration*, 330(11):2497–2508, May 2011.

[58] V.B. Georgiev, J. Cuenca, M. Moleron, F. Gautier, and L. Simon. Recent progress in vibration reduction using acoustic black hole effect. In *10eme Congrès Françaisd'Acoustique, Lyon, 12-16 Avril 2010*, 2010.

[59] M. Géradin and D. Rixen. *Mechanical Vibrations: Theory and Applications to Structural Dynamics*. John Wiley & Sons, 1997.

[60] D.J. Gorman. A general solution for the free vibration of rectangular plates resting on uniform elastic edge supports. *Journal of Sound and Vibration*, 139:325–335, 1990.

[61] J.-L. Guyader. *Vibrations des milieux continus*. Hermes Science Publications, October 2002.

[62] J.-L. Guyader and C. Lesueur. Acoustic transmission through orthotropic multilayered plates. part i: plate vibration modes. *Journal of Sound and Vibration*, 58(1):51–68, 1978.

[63] S.W. Hawking. Particle creation by black holes. *Communications in Mathematical Physics*, 43(3):199–220, 1975.

[64] S.W. Hawking. Information loss in black holes. *Physical Review D: Particles and Fields*, 72:084013, 2005.

[65] Y. Hua and T. K. Sarkar. Matrix pencil method for estimating parameters of exponentially damped/undamped sinusoids in noise. *IEEE Trans. Acoust. Speech Sig. Process.*, 38(5):814–824, 1990. ex. MatrixPen.

[66] A. Iserles, A. Martinsen, and S.P. Norset. On the implementation of the method of magnus series for linear differential equations. *BIT*, 39(2):281–304, 1999.

[67] D. I. G. Jones. Response and damping of a simple beam with tuned dampers. *Journal of the Acoustical Society of America*, 42:50–53, 1967.

[68] D. I. G. Jones. Reflections on damping technology at the end of the twentieth century. *Journal of Sound and Vibration*, 190(3):449–462, 1996.

[69] D. I. G. Jones, A. D. Nashif, and R.L. Adkins. The effect of tuned dampers on vibrations of simpple structures. *American Institute of Aeronautics and Astronautics Journal*, 5(2):310–315, 1967.

[70] D.I.G. Jones and W.J. Trapp. Influence of additive damping on resonance fatigue of structures. *Journal of Sound and Vibration*, 17(2):157–185, 1971.

[71] A. Joshi and B.S. Madhusudhan. A unified approach to free vibration of damaged beams having various homogeneous boundary conditions. *Journal of Sound and Vibration*, 147(3):475–488, 1991.

[72] L.E. Kinsler, A.R. Frey, A.B. Coppens, and J.V. Sanders. *Fundamentals of acoustics, fourth edition.* John Wiley & Sons, 2000.

[73] V. Kralovic and V. V. Krylov. Some new methods of damping impact-induced vibrations in badminton racquets. In *Proceedings of Institute of Acoustics*, Reading, United Kingdom, 2008.

[74] T. Kreis. *Holographic Interferometry: principles and methods.* Wiley, 1996.

[75] V. V. Krylov. New type of vibration dampers utilising the effect of acoustic 'black holes'. *Acta Acustica United with Acustica*, 90:830–837, 2004.

[76] V.V. Krylov. Propagation of localized vibration modes along edges of immersed wedge-like structures : geometrical-acoustics approach. *Journal of Computational Acoustics*, 7(1):57–70, 1999.

[77] V.V. Krylov and F.J.B.S. Tilman. Acoustic 'black holes' for flexural waves as effective vibration dampers. *Journal of Sound and Vibration*, 274(3-5):605–619, July 2004.

[78] V.V. Krylov and R Winward. Experimental investigation of the acoustic black hole effect for flexural waves in tapered plates. *Journal of Sound and Vibration*, 300(1-2):43–49, February 2007.

[79] A. Kumar and C.M. Krousgrill. Mode-splitting and quasi-degeneracies in circular plate vibration problems: the example of free vibrations of the stator of a traveling wave ultrasonic motor. *Journal of Sound and Vibration*, 331:5788–5803, 2012.

[80] C. Lambourg. *Modèle temporel pour la simulation numérique de plaques vibrantes: Application à la synthèse sonore.* PhD thesis, Université du Maine, Le Mans, 1997.

[81] J. Laroche. The use of matrix pencil method for the spectrum analysis of musical signal. *The Journal of the Acoustical Society of America*, 94(4):1958–1965, 1993.

[82] B. Laulagnet and J.-L. Guyader. Sound radiation from finite cylindrical shells by means of asymptotic expansion of three-dimensional equations for coating. *The Journal of the Acoustical Society of America*, 96(1):277–286, 1994.

[83] S.Y. Lee and S.M. Lin. Levy-type solution for the analysis of nonuniform plates. *Computers and Structures*, 49(6):931–939, 1993.

[84] A. Leissa. *Vibration of plates.* Acoustical society of America, London, 1993.

[85] Y.K. Lin and B.K. Donaldson. A brief survey of transfer matrix techniques with special reference to the analysis of aircraft panels. *Journal of Sound and Vibration*, 10(1):103–143, 1969.

[86] J. Linjama and T. Lahti. Estimation of bending wave intensity in beams using the frequency response technique. *Journal of Sound and Vibration*, 153(1):21–26, 1992.

[87] J. Linjama and T. Lahti. Measurement of bending wave reflection and impedance in a beam by the structural intensity technique. *Journal of Sound and Vibration*, 161(2):317–331, 1993.

[88] Y. Y. Lu. A fourth-order magnus scheme for helmholtz equation. *Journal of Computational and Applied Mathematics*, 173:247–258, 2005.

[89] R. H. Lyon and R. G. Dejong. *Theory and Application of Statistical Energy Analysis.* Butterworth Heinemann, 1995.

[90] B.R. Mace. Wave reflection and transmission in beams. *Journal of Sound and Vibration*, 97:237–246, 1984.

[91] K.P. Menard. *Dynamic mechanical analysis: a practical introduction.* CRC Press, 1999.

[92] G. Michon, A. Almajid, and G. Aridon. Soft hollow particle damping identification in honeycomb structures. *Journal of Sound and Vibration*, 332:536–544, 2013.

[93] M.A. Mironov. Propagation of a flexural wave in a plate whose thickness decreases smoothly to zero in a finite interval. *Soviet Physics: Acoustics*, 34(3):318–319, 1988.

[94] M.A. Mironov and V. V. Pislyakov. One-dimensional acoustic "black hole". In *Congrès Français d'Acoustique 2002*, 2002.

[95] M.A. Mironov and V. V. Pislyakov. One-dimensional acoustic waves in retarding structures with propagation velocity tending to zero. *Acoustical Physics*, 48(3):400–405, 2002.

[96] M. Moleron. Absorption passive de vibrations de poutres et de plaques par effet trou noir acoustique. Master's thesis, Université du Maine, 2009.

[97] M.-H. Moulet. *Les jonctions en mécanique vibratoire : représentation par matrice de diffusion et caractérisation expérimentale pour des poutres assemblées.* PhD thesis, Université du Maine, 2003.

[98] M.-H. Moulet and F. Gautier. Reflection, transmission and coupling of longitudinal and flexural waves at beam junctions. part ii: Experimental and theoretical results. *Acta Acustica United with Acustica*, 93:37–47, 2007.

[99] NASA/CXC/M.Weiss. For students: What is a black hole ? `http://www.nasa.gov/audience/forstudents/5-8/features/what-is-a-black-hole-58.html`, 2014.

[100] A. D. Nashif, D. I. G. Jones, and J. P. Henderson. *Vibration Damping.* A. Wiley-Interscience Publication, 1985.

[101] A.N. Norris. Reflection and transmission of structural waves at an interface between doubly curved shells. *Acta Acustica United with Acustica*, 84:1066–1076, 1998.

[102] H. Oberst and K. Frankenfeld. Uber die dampfung biegeswchwingungen dunner blech durch fest haftende belage. *Acustica*, 4:181–194, 1952.

[103] D.J. O'Boy and V.V. Krylov. Damping of flexural vibrations in circular plates with tapered central holes. *Journal of Sound and Vibration*, 330(10):2220–2236, May 2011.

[104] D.J. O'Boy, V.V. Krylov, and V. Kralovic. Damping of flexural vibrations in rectangular plates using the acoustic black hole effect. *Journal of Sound and Vibration*, 329(22):4672–4688, October 2010.

[105] V. Pagneux. Multimodal admittance method in waveguides and singularity behavior at high frequencies. *Journal of Computational and Applied Mathematics*, 234:1834–1841, 2010.

[106] J. M. Papy, L. De Lathauwer, and S. Van Huffel. A shift invariance-based order-selection technique for exponential data modelling. *Sig. Proc. Letter, IEEE*, 14(7):473–476, 2007. ex. SAMOS.

[107] A. Pelat. *Approche modale de la propagation acoustique dans les guides d'ondes ouverts. Application à l'acoustique urbaine.* PhD thesis, Université du Maine, 2009.

[108] R. Penrose. A generalized inverse for matrices. *Proceedings of the Cambridge Philosophical Society*, 51:406–413, 1955.

[109] J.-B. Piaud and J. Nicolas. La mesure de l'impédance mécanique. In *Proceedings 12th ICA, Toronto, 24-31 July 1986, Paper M2-7*, 1986.

[110] T. Pinkaew, P. Lukkunaprasit, and P. Chatupote. Seismic effectiveness of tuned mass dampers for damage reduction of structures. *Engineering Structures*, 25:39–46, 2003.

[111] V. V. Pislyakov, M.A. Mironov, and A. Svadkovsky. Vibration of specially tapered beams and plates. In *InterNoise*, 2000.

[112] J. Poittevin. Mesure du coefficient de réflexion deu trou noir acoustique mono-dimensionnel. Master's thesis, Université du Maine, 2012.

[113] J. Poittevin, P. Picart, F. Gautier, and C. Pézerat. Méthode de mesure de champs vibratoires par holographie optique numérique ultra-rapide. In *Congrès Français d'Acoustique, Poitiers, 22–25 april 2014*, 2014.

[114] R. Rana and T.T. Soong. Parametric study and simplified design of tuned mass dampers. *Engineering Structures*, 20(3):193–204, 1998.

[115] M. D. Rao. Recent applications of viscoelastic damping for noise control in automobiles and commercial airplanes. *Journal of Sound and Vibration*, 262:457–474, 2003.

[116] D. Ross, E.L. Ungar, and E.M. Kerwin. Damping of plate flexural vibrations by means of viscoelastic laminae. In *Structural damping*, pages 49—57. J.E. Ruzicka, Oxford, Pergamon Press edition, 1960.

[117] R. Roy and T. Kailath. ESPRIT – Estimation of Signal Parameters via Rotational Invariance Techniques. *IEEE Transactions on Acoustics Speech and Signal Processing*, 37(7):984–995, 1989. ex. ESPRIT.

[118] J. Schiff and S. Shnider. A natural approach to the numerical intergration of ricatti differential equations. *SIAM (Soc. Ind. Appl. Math.) J. Numer. Anal.*, 36:1392–1413, 1999.

[119] R. O. Schmidt. Multiple emitter location and signal parameter estimation. *IEEE Transactions on Antennas and Propagation*, 34:273–280, 1986. ex MUSIC.

[120] G. Schwarz. Estimating the dimensions of a model. *The Annals of Statistics*, 6:461–464, 1978.

[121] K. Schwarzschild. Über das gravitationsfeld eines massenpunktes nach der einsteinschen theorie. *Sitzungsberichte der Königlich Preussischen Akademie der Wissenschaften*, 1:189–196, 1916.

[122] J.C. Snowdon. Vibration of cantilever beams to which dynamic absorbers are attached. *Journal of the Acoustical Society of America*, 39(5):878–886, 1966.

[123] J.C. Snowdon. *Vibration and Shock in damped mechanical systems.* New York: John Wiley, 1970.

[124] P.A. Taillard, F. Laloë, M. Gross, J.P. Dalmont, and J Kergomard. Measurements of resonance frequencies of clarinet reeds and simulations, 2012.

[125] C. Touzé, O. Thomas, and M. Amabili. Transition to chaotic vibrations for harmonically forced perfect and imperfect circular plates. *International Journal of Non-Linear Mechanics*, 46:234–246, 2011.

[126] E.E. Ungar. Loss factors of viscoelastically damped beam structures. *Journal of the Acoustical Society of America*, 34(8):1082–1089, 1962.

[127] W.G. Unruh. Experimental black-hole evaporation. *Physical Review Letters*, 46(21):1351–1353, 1981.

[128] W.G. Unruh. Dumb holes and the effects of high frequencies on black hole evaporation, 1995.

[129] W.G. Unruh and R. Schutzhold. On slow light as a black hole analogue. *Physical Review D*, 68:024008, 2003.

[130] C. Vemula, A.N. Norris, and G.D. Cody. Attenuation of waves in plates and bars using a graded impedance interface at edges. *Journal of Sound and Vibration*, 196(1):107–127, September 1996.

[131] M. Visser. Acoustic black holes: horizons, ergospheres and hawking radiation. *Classical and Quantum Gravity*, 15:1767–1791, 1998.

[132] J.F. Wang, C.C. Lin, and B.L. Chen. Vibration suppression for high-speed railway bridges using tuned mass dampers. *International Journal of Solids and Structures*, 40:465–491, 2003.

[133] Z. Wang and A.N. Norris. Waves in cylindrical shells with circumferential submembers : a matrix approach. *Journal of Sound and Vibration*, 181(3):457–484, 1995.

[134] M. Wax and T. Kailath. Detection of signals by information theoretic criteria. *IEEE Transactions on Acoustics Speech and Signal Processing*, 33:387–392, 1985. ex ITC.

[135] J. Wheeler. Goddard Institute of Space Studies, New York, 1967.

[136] Y. Xiang, Y.B. Zhao, and G.W. Wei. Levy solutions for vibration of multi-span rectangular plates. *International Journal of Mechanical Sciences*, 44:1195–1218, 2002.

[137] G. Xie, D.J. Thompson, and C.J.C. Jones. Mode count and modal density of structural systems: relationships with boundary conditions. *Journal of Sound and Vibration*, 274(3-5):621–651, July 2004.

[138] Z. Zhao, S.C. Conlon, and F. Semperlotti. Broadband energy harvesting using acoustic black hole structural tailoring. *Smart Materials and Structrures*, 23:065021, 2014.